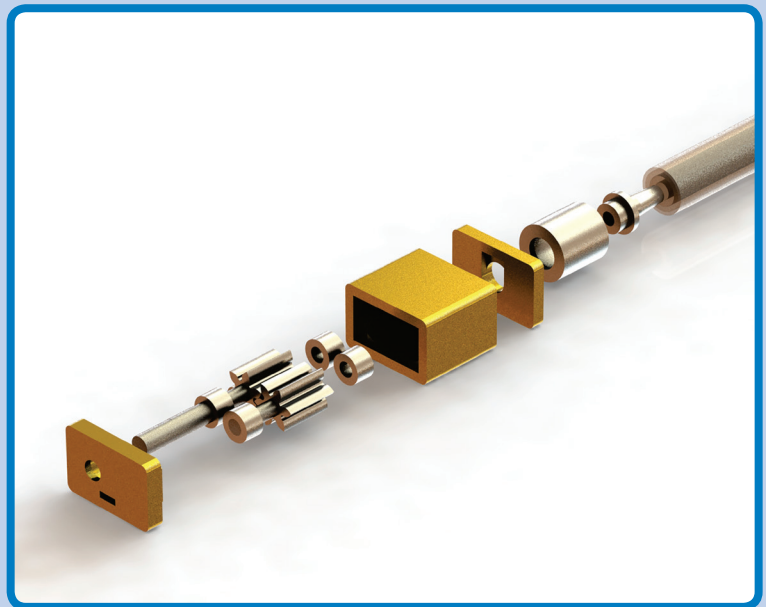




# Strojniški vestnik

## Journal of Mechanical Engineering



no. **7-8**

year **2018**

volume **64**

# Strojniški vestnik – Journal of Mechanical Engineering (SV-JME)

## Aim and Scope

The international journal publishes original and (mini)review articles covering the concepts of materials science, mechanics, kinematics, thermodynamics, energy and environment, mechatronics and robotics, fluid mechanics, tribology, cybernetics, industrial engineering and structural analysis.

The journal follows new trends and progress proven practice in the mechanical engineering and also in the closely related sciences as are electrical, civil and process engineering, medicine, microbiology, ecology, agriculture, transport systems, aviation, and others, thus creating a unique forum for interdisciplinary or multidisciplinary dialogue.

The international conferences selected papers are welcome for publishing as a special issue of SV-JME with invited co-editor(s).

## Editor in Chief

Vincenc Butala

University of Ljubljana, Faculty of Mechanical Engineering, Slovenia

## Technical Editor

Pika Škraba

University of Ljubljana, Faculty of Mechanical Engineering, Slovenia

## Founding Editor

Bojan Kraut

University of Ljubljana, Faculty of Mechanical Engineering, Slovenia

## Editorial Office

University of Ljubljana, Faculty of Mechanical Engineering

SV-JME, Aškerčeva 6, SI-1000 Ljubljana, Slovenia

Phone: 386 (0)1 4771 137

Fax: 386 (0)1 2518 567

info@sv-jme.eu, <http://www.sv-jme.eu>

**Print:** Abografika, printed in 300 copies

## Founders and Publishers

University of Ljubljana, Faculty of Mechanical Engineering, Slovenia

University of Maribor, Faculty of Mechanical Engineering, Slovenia

Association of Mechanical Engineers of Slovenia

Chamber of Commerce and Industry of Slovenia,

Metal Processing Industry Association

## President of Publishing Council

Mitjan Kalin

University of Ljubljana, Faculty of Mechanical Engineering, Slovenia

## Vice-President of Publishing Council

Jože Balič

University of Maribor, Faculty of Mechanical Engineering, Slovenia

## International Editorial Board

Kamil Arslan, Karabuk University, Turkey

Hafiz Muhammad Ali, University of Engineering and Technology, Pakistan

Josep M. Bergada, Politechnical University of Catalonia, Spain

Anton Bergant, Litoštroj Power, Slovenia

Miha Boltežar, UL, Faculty of Mechanical Engineering, Slovenia

Franci Čuš, UM, Faculty of Mechanical Engineering, Slovenia

Janez Diaci, UL, Faculty of Mechanical Engineering, Slovenia

Anselmo Eduardo Diniz, State University of Campinas, Brazil

Igor Emri, UL, Faculty of Mechanical Engineering, Slovenia

Imre Felde, Obuda University, Faculty of Informatics, Hungary

Janez Grum, UL, Faculty of Mechanical Engineering, Slovenia

Imre Horvath, Delft University of Technology, The Netherlands

Aleš Hribernik, UM, Faculty of Mechanical Engineering, Slovenia

Soichi Ibaraki, Kyoto University, Department of Micro Eng., Japan

Julius Kaplunov, Brunel University, West London, UK

Iyas Khader, Fraunhofer Institute for Mechanics of Materials, Germany

Jernej Klemenc, UL, Faculty of Mechanical Engineering, Slovenia

Milan Kljajin, J.J. Strossmayer University of Osijek, Croatia

Peter Krajnik, Chalmers University of Technology, Sweden

Janez Kušar, UL, Faculty of Mechanical Engineering, Slovenia

Gorazd Lojen, UM, Faculty of Mechanical Engineering, Slovenia

Thomas Lübben, University of Bremen, Germany

George K. Nikas, KADMOS Engineering, UK

José L. Ocaña, Technical University of Madrid, Spain

Vladimir Popović, University of Belgrade, Faculty of Mech. Eng., Serbia

Franci Pušavec, UL, Faculty of Mechanical Engineering, Slovenia

Bernd Sauer, University of Kaiserslautern, Germany

Rudolph J. Scavuzzo, University of Akron, USA

Branko Vasić, University of Belgrade, Faculty of Mechanical Eng., Serbia

Arkady Voloshin, Lehigh University, Bethlehem, USA

## General information

Strojniški vestnik – Journal of Mechanical Engineering is published in 11 issues per year (July and August is a double issue).

Institutional prices include print & online access: institutional subscription price and foreign subscription €100,00 (the price of a single issue is €10,00); general public subscription and student subscription €50,00 (the price of a single issue is €5,00). Prices are exclusive of tax. Delivery is included in the price. The recipient is responsible for paying any import duties or taxes. Legal title passes to the customer on dispatch by our distributor.

Single issues from current and recent volumes are available at the current single-issue price. To order the journal, please complete the form on our website. For submissions, subscriptions and all other information please visit: <http://www.sv-jme.eu>.

You can advertise on the inner and outer side of the back cover of the journal. The authors of the published papers are invited to send photos or pictures with short explanation for cover content.

We would like to thank the reviewers who have taken part in the peer-review process.

The journal is subsidized by Slovenian Research Agency.

Strojniški vestnik - Journal of Mechanical Engineering is available on <http://www.sv-jme.eu>, where you access also to papers' supplements, such as simulations, etc.



**Cover:** Exploded view and partly assembled prototype of a new hydropowered surgical drill. The prototype is on scale and based on an external gear motor, where one gear is extended with a drill bit. Experiments were performed at the Laboratory of Material Sciences, Faculty of Mechanical Maritime and Materials Engineering, Delft University of Technology, The Netherlands and the Laboratory of Austrian Center for Medical Innovation and Technology, Wiener Neustadt, Austria.

### Image Courtesy:

Wouter Gregoor, MSc student, Department of Biomechanical Engineering, Faculty of Mechanical Maritime and Materials Engineering, Delft University of Technology, The Netherlands

**ISSN 0039-2480, ISSN 2536-2948 (online)**

© 2018 Strojniški vestnik - Journal of Mechanical Engineering. All rights reserved. SV-JME is indexed / abstracted in: SCI-Expanded, Compendex, Inspec, ProQuest-CSA, SCOPUS, TEMA. The list of the remaining bases, in which SV-JME is indexed, is available on the website.

## Contents

**Strojniški vestnik - Journal of Mechanical Engineering**  
**volume 64, (2018), number 7-8**  
**Ljubljana, July-August 2018**  
**ISSN 0039-2480**

**Published monthly**

### **Papers**

Wouter Gregoor, Jenny Dankelman, Christoph Kment, Gabriëlle J.M. Tuijthof: Hydraulic Actuator Selection for a Compliant Surgical Bone Drill: A Theoretical Approach	425
Igor Ivanovski, Darko Goričanec, Julijan Jan Salamunić, Tina Žagar: The Comparison between Two High-Temperature Heat-Pumps for the Production of Sanitary Water	437
Honghu Pan, Xingxi He, Sai Tang, Fanming Meng: An Improved Bearing Fault Diagnosis Method using One-Dimensional CNN and LSTM	443
Albin Matavz, József Mursics, Ivan Anzel, Tina Zagar: The Influence of External Conditions on the Mechanical Properties of Resin-bonded Grinding Wheels	453
Jelena Vidaković, Vladimir Kvrđić, Mihailo Lazarević: Control System Design for a Centrifuge Motion Simulator Based on a Dynamic Model	465
Jun Wan, Jiafeng Yao, Liang'an Zhang, Hongtao Wu: A Weighted Gradient Projection Method for Inverse Kinematics of Redundant Manipulators Considering Multiple Performance Criteria	475
Mutiu F. Erinosh, Esther T. Akinlabi: Influence of Laser Power on Improving the Wear Properties of Laser-Deposited Ti-6Al-4V+B4C Composite	488



# Hydraulic Actuator Selection for a Compliant Surgical Bone Drill: A Theoretical Approach

Wouter Gregoor<sup>1</sup> – Jenny Dankelman<sup>1</sup> – Christoph Kment<sup>2</sup> – Gabriëlle J.M. Tuijthof<sup>3,4,\*</sup>

<sup>1</sup> Delft University of Technology, The Netherlands

<sup>2</sup> Austrian Center for Medical Innovation and Technology, Austria

<sup>3</sup> Zuyd University of Applied Sciences, The Netherlands

<sup>4</sup> ACES, Academic Medical Centre, The Netherlands

*A compliant bone drill provides advantages over conventional straight drills, because it allows surgical access via a minimally invasive approach. Hydropower allows the transfer of pressurized water with a compliant hose. The goal is to select the hydraulic actuator for this compliant bone drill by reviewing existing actuator principles. The selection was performed with a theoretical analysis. Design requirements were derived from a challenging minimally invasive bone drill procedure, and were set: a speed of 750 rpm, a torque of 0.015 Nm and a maximum dimensional volume of 5 mm × 5 mm × 10 mm to drill Ø 1.5 mm holes in human bone. A literature search was performed. For each actuator, the fluid flow and the required pressure difference were described as a function of the actuator dimensions and the rotational speed. Selection of the actuator was performed by it meeting the set output power, the torque, realistic input dimensions, and requiring the lowest pressure and number of parts. Existing literature provided six hydraulic actuators: external gear motor, gear ring motor, axial turbine, radial turbine, Pelton wheel, and Ossberger turbine. The latter four are hydrodynamic turbines, which could not meet the rotational speed. The external gear motor was selected for its lowest required pressure difference ( $11.5 \times 10^5$  Pa) and design simplicity. This theoretical design approach can be used for other applications.*

**Keywords:** orthopaedic procedures, surgical tools, actuator, bone drill, hydraulic

## Highlights

- Quantitative design requirements for a compliant minimally invasive surgical bone drill were derived.
- Six hydraulic actuators were reviewed: external gear motor, gear ring motor, axial turbine, radial turbine, Pelton wheel, and Ossberger turbine.
- Theoretical calculation using the quantitative requirements resulted in the selection of the external gear motor as the most feasible actuator.
- The theoretic equations can be applied to select hydraulic actuators for other applications.

## 0 INTRODUCTION

Arthroscopy is minimally invasive surgery performed in human joints. It has tremendous benefits for patients in terms of low morbidity and quick rehabilitation. In this paper, we focus on the arthroscopic microfracture technique, which is the first-line treatment for cartilage lesions in knees, ankles and other joints [1] and [2]. With microfracture, small holes (microfractures) are drilled perpendicular to the cartilage lesion, which eventually forms regenerated fibrocartilage [1] and [2]. The microfracture technique is a typical medical case that reveals technical drawbacks of using straight instruments and predefined access portals in joints: not every surgical site can be reached, and perpendicular drilling is possible in only a few locations in joints [3] and [4]. In the worst case, these drawbacks prevent adequate treatment. From a mechanical viewpoint, two contradictory requirements have to be met: instruments need to be compliant and steerable to reach lesions (flexibility), and they need to be stiff

to resist machining forces (rigidity) [1] and [2]. Some solutions were proposed to achieve the above functionality using electromotors and mechanical transmission, but without success [5] to [7]. We explore the feasibility of a different technical principle: the design of a compliant bone drill that is to be powered by a hydraulic actuator. This allows energy transfer to the joint via a compliant hose that carries pressurized water. This design provides the additional advantages that during arthroscopy saline fluid is already used to rinse the joint, and water contributes to the cooling of the drill bit to prevent necrosis [4]. The goal of this study is to select the most suitable miniature hydraulic actuator that transfers hydraulic power to the drill bit and fits within a minimally invasive instrument.

## 1 METHODS

First, the general theory on hydraulic actuators describes the two fundamental working principles (hydrostatic motors and hydrodynamic turbines)

\*Corr. Author's Address: Research Centre Smart Devices, Zuyd University of Applied Sciences, Nieuw Eychholt 300, 6419 DJ Heerlen, The Netherlands, gabrielle.tuijthof@zuyd.nl

with mathematical formulas. Second, a review of the literature gives an inventory of actuators. Third, the actuators are evaluated using a theoretical design engineering approach. Calculations are performed with quantitative values derived for the medical case of micro-fracturing, i.e., required output power  $P$ , the rotational speed  $n$ , the required torque  $T$  and realistic input dimensions. This gives the fluid flow  $Q$  and the required pressure difference  $\Delta p = p_{in} - p_{out}$  per actuator upon which the most suitable is selected.

## 2.1 Fundamental Hydraulic Working Principles

In this study, the presence of losses is neglected and a steady flow of an ideal fluid is assumed [8]. Consequently, the output power equals the input power:

$$P = T \cdot 2\pi \cdot \frac{n}{60} = \Delta p \cdot Q. \quad (1)$$

### 2.1.1 Hydrostatic Motors

In hydrostatic motors, a displacement volume  $V$  is trapped and transported periodically by moving parts (e.g., gears or vanes) (Fig. 1). The loads on the moving parts transfer in  $\Delta p$  to give hydraulic power [8] and [9].  $Q$  follows from [9] (Fig. 1):

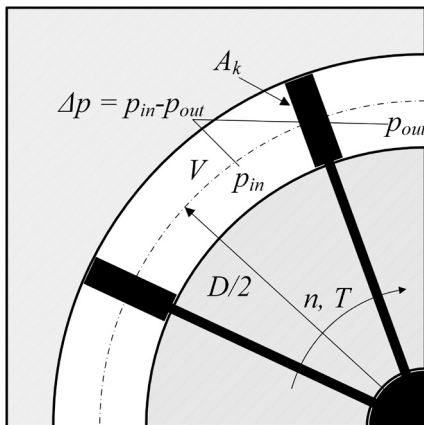


Fig. 1. Schematic drawing of a simplified hydrostatic motor; adapted from [9]

$$Q = V \cdot \frac{n}{60} = \left(\frac{1}{8} \cdot \pi D \cdot A_k\right) \cdot \frac{n}{60}, \quad (2)$$

where  $D$  is the diameter and  $A_k$  is the effective area. Similarly,  $\Delta p$  follows from Eqs. (1) and (2) and [9] (Fig. 1):

$$\Delta p = \frac{P}{Q} = \frac{1}{15} \cdot \frac{T}{D \cdot A_k}. \quad (3)$$

A typical characteristic of hydrostatic motors is that  $\Delta p$  is independent of  $n$ . This implies that  $T$  can be set by choosing  $\Delta p$  and  $Q$  [9].

### 2.1.2 Hydrodynamic Turbines

Hydrodynamic turbines are open structures through which the flow passes. Energy is transferred from the fluid to the turbine by dynamic action [10]. The relative movement exists between the continuous moving fluid and the turbine blades. This creates a momentum exchange [10]. In contrary to the hydrostatic motors, the torque is a function of the rotational speed  $T(n)$ . Calculation of  $Q$  requires the formulation of absolute ( $C_{in}$  and  $C_{out}$ ) and relative ( $c_{in}$  and  $c_{out}$ ) inlet and outlet velocities and their radial and tangential components ( $C_R$  and  $C_T$ ) (Fig. 2). The direction of the common absolute inlet and outlet velocity  $C_{in}$  and  $C_{out}$  on one blade is indicated by solid thick arrows. The turbine velocities at the inner and outer part of the blades are  $U_{in}$  and  $U_{out}$  (at half of the diameter  $D_{out}$  vs.  $D_{in}$ ). The absolute velocities are decomposed into a tangential  $C_{Tin}$  and  $C_{Tout}$  and radial components  $C_{Rin}$  and  $C_{Rout}$  indicated by dotted arrows. The fluid inlet and outlet angles  $\alpha_{in}$  and  $\alpha_{out}$  and blade angles  $\beta_{in}$  and  $\beta_{out}$  are needed for this decomposition. Finally, the fluid velocities relative to the turbine  $c_{in}$  and  $c_{out}$  are derived and indicated by striped arrows. Fluid enters the hydrodynamic turbine with an absolute velocity  $C_{in}$  at a fluid inlet angle  $\alpha_{in}$ . This yields a relative velocity  $c_{in} = C_{in} - U_{in}$  with  $U_{in}$  is the inner turbine velocity (Fig. 2). The fluid exits with a relative velocity  $c_{out}$  at an angle  $\beta_{out}$ . This gives an absolute outlet velocity  $C_{out} = c_{out} + U_{out}$  with  $U_{out}$  is the outer turbine velocity at fluid outlet angle  $\alpha_{out}$  (Fig. 2).  $Q$  is given by [10]:

$$Q(n) = \frac{1}{k_v} \cdot C_{Rout}(n) \cdot A_{turbine}. \quad (4)$$

With  $A_{turbine}$  is the effective area where the fluid flows through, and  $k_v$  is a correction factor for the volume that is occupied by the vanes. For the working principle of hydrodynamic turbines,  $T(n)$  is derived from Newton's second law of motion in which the mass flow changes over time, and with steady-state tangential absolute fluid velocities ( $C_{Tin}$  and  $C_{Tout}$ ) [10] and [11] (Fig. 2):

$$T = m \cdot \frac{d}{dt} \cdot C_T(t) \cdot \frac{D}{2} = Q(n) \cdot \rho \cdot \left( \frac{D_{out}}{2} \cdot C_{Tin}(n) + \frac{D_{in}}{2} \cdot C_{Tout}(n) \right). \quad (5)$$

Filling out Eq. (4) in Eq. (5) gives [10]:

$$T(n) = \frac{1}{k_v} \cdot C_{Rout}(n) \cdot A_{turbine} \cdot \rho \left( \frac{D_{out}}{2} \cdot C_{Tin}(n) + \frac{D_{in}}{2} \cdot C_{Tout}(n) \right). \quad (6)$$

Notice that  $C_T$  and  $C_R$  are a function of  $n$  and the turbine's dimensions. Subsequently,  $\Delta p$  is derived from Bernoulli's equation [10]:

$$P = \left( \Delta p + \frac{1}{2} \cdot \rho (C_{in}^2(n) - C_{out}^2(n)) \right) \cdot Q(n). \quad (7)$$

First Eq. (1) is substituted for  $P$ , followed by Eq. (6) for  $T$ . Next Eq. (7) is rewritten to give  $\Delta p$  [10]:

$$\Delta p = \rho \left( \frac{D_{out}}{2} \cdot C_{Tin}(n) + \frac{D_{in}}{2} \cdot C_{Tout}(n) \right) - \frac{1}{2} \cdot \rho (C_{in}^2(n) - C_{out}^2(n)). \quad (8)$$

Thus,  $\Delta p$  depends on  $n$  for hydrodynamic turbines.

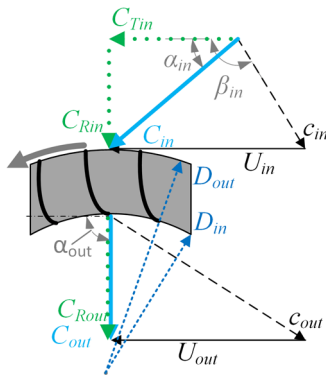


Fig. 2. Schematic drawing of a cross-section of three blades of a radial turbine (grey) to highlight the velocity profile; adapted from [10]

## 2.2 Literature Review

First, surgical instruments were reviewed that use hydrostatic motors and/or hydrodynamic turbines as proposed by the concept. Second, the review was concentrated on general working principles of hydraulic actuators by searching the Scopus database and the library of Delft University of Technology (www.library.tudelft.nl). In Scopus, the following keywords were used without date and language restrictions using OR:

- Hydraulic motor, hydrostatic motor, positive displacement for hydrostatic motors,

- turbomachinery, hydrodynamic, hydraulic turbine, water turbine, impeller for hydrodynamic turbines.

In the TU Delft library collection, the following categories were reviewed:

- EH / Fluid mechanics EHA / Fluid mechanics: general,
- NG / Energy conversion systems NGM / Turbomachinery: general NGN / Hydraulic converters: general NGP / Pump technology: general NGR / Pumps NGS / Hydraulic motors and turbines,
- MG / Design of control systems MGC / Servomechanisms, fluid systems.

## 2.3 Requirements Set by Arthroscopic Microfracture Technique

To perform a quantitative evaluation of the found actuators, requirements were set using the arthroscopic microfracture technique [1] and [2].

### 2.3.1 Dimensions

The suggested dimensions of the standard technique were adopted: a hole diameter of 1.5 mm and a hole depth of 4 mm [1]. Thus, the drill bit diameter  $D_{drill}$  was determined to be 1.5 mm and used to calculate the drilling torque. Additionally, the limited space in human joints sets a maximum height and width of 5 mm to the embodiment of a hydraulic actuator [12] and [13]. The length of a hydraulic actuator was set at a maximum of 10 mm to allow manoeuvrability in human joints [13]. These relatively small dimensions pose restrictions because small parts reach their material limits sooner upon loading by relatively high values of  $\Delta p$  and  $T$ . This was taken into account when evaluating the hydraulic actuators.

### 2.3.2 Torque

Literature presents formulas that describe the torque  $T$  for drilling in bone [14]:

$$T = j \cdot f^y \cdot \frac{\pi}{4} (D_{drill})^2 \cdot 1000, \quad (9)$$

where  $f$  is the drilling feed in mm/rev and  $j$ ,  $y$ ,  $x$  and  $B$  are constants related to the drill type. Eq. (9) was verified by comparing its calculated outcome to experimental results from other studies [15] and [16]. The results gave the same order of magnitude for  $T$  (Table 1). The drilling feed for the microfracture technique was determined according to Sezek [17]

who indicated that a safe drilling feed of 70 mm/min at  $n=370$  rpm (equals 0.19 mm/rev) avoids necrosis. Filling out  $f$ , the set  $D_{drill}$  and the drill constants of a standard surgical twist drill bit [14] (i.e.  $j=1.6 \times 10^{-2}$ ,  $y=0.39$ ,  $x=2.2$  and  $B=3.8 \times 10^{-4}$ ) in Eq. (9) gives a  $T$  of 0.0015 Nm.

**Table 1.** Bone drilling data; a) gives the calculated drilling torque  $T$  using Eq. (9),  $D_{drill}$  and feed  $f$  suggested by Wiggins [14]; b) presents the experimentally measured drilling torques; note that the drill diameters are different from the set  $D_{drill}$

Parameter	Wiggins [14] <sup>a)</sup>	Jacob [15] <sup>b)</sup>	Tuijthof [16] <sup>b)</sup>
$D_{drill}$ [mm]	2.77	3.2	3 to 3.2
$f$ [mm/rev]	0.25	0.20	0.3
$T$ [Nm]	0.06	0.07	0.02 to 0.12

### 2.3.2 Speed, Power and Pressure

Eq. (9) indicates that the torque is independent of speed. Jacob et al. [15] show that this only holds for rotational speeds above 750 rpm. Therefore, the hydraulic actuators were evaluated at  $n = 750$  rpm. Filling out  $n$  and  $T$  in Eq. (1) sets the required power  $P$  to be 1.16 W. Finally, we set  $\Delta p$  as low as possible to remain below the material limits of conventional materials.

## 3 RESULTS

The literature search yielded no small-sized hydraulic actuators suitable for the use case. Most hydrodynamic turbines are applied on a much larger scale in, for example, hydro-electric power plants. The hydraulic actuators and corresponding mathematical descriptions were derived from four out of ten books [8] to [11]. The discarded books describe overlapping content.

### 3.1 Hydrostatic Motors

Hydrostatic motors can be divided into piston, gear, and vane motors (Fig. 3) [9]. As the names suggest, piston motors work by moving pistons, gear motors work by interlocking gears that trap the fluid volume in the space where the gears do not interlock, and vane motors work by moving vanes that enclose the fluid volume [9].

Given the dimensional requirements, the relative high complexity and large number of small parts of piston and vane motors, only the gear motors were analysed. Furthermore, the gear ring motor does not require a shekel-shaped separation element and can be

build smaller in comparison to the internal gear motor (Fig. 3). Therefore, only the external gear motor and the gear ring motor were analyzed.

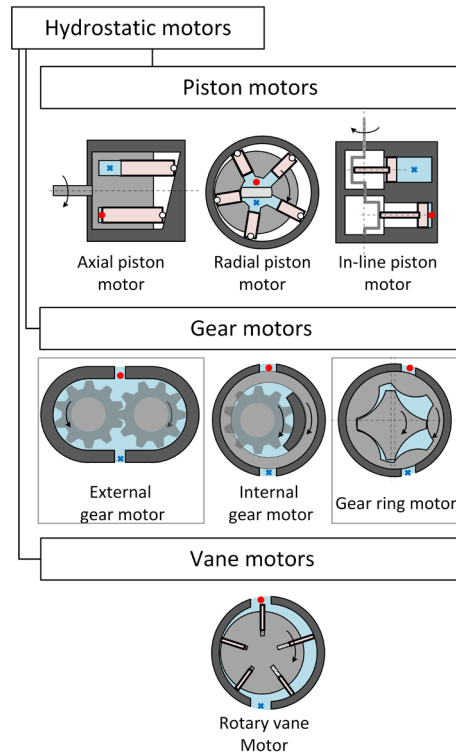


**Fig. 3.** Overview of hydrostatic motors; for each, a section view is presented indicating the fluid (light blue), the stationary parts (dark grey), the translating parts (pink/thick lines), the rotating parts (light grey) the fluid inlet (red dot) and the fluid outlet (blue cross); adapted from [9]

#### 3.1.1 External Gear Motor

The external gear motor works with pressurized fluid entering the motor that causes a distributed force  $F_p$  acting on the two gears (Fig. 4). Formulating  $Q(n, dimensions)$  starts by determining the mean displacement volume  $V_m$  (Fig. 4). It is assumed that both gears are equally sized, only one teeth pair contributes to the displacement and that the pressure drop occurs over one teeth pair. First, the instantaneous displacement volume  $dV$  is derived from the instantaneous work  $dW$  [9]:

$$dW = T_1 \cdot d\phi_1 + T_2 \cdot d\phi_2 = dV \cdot \Delta p. \quad (10)$$

With  $T_1$  and  $T_2$  are the torques on both gears and  $d\phi_1$  and  $d\phi_2$  their change of angular displacement. They are expressed in the gear diameter  $D_{out}$ , the gear width  $b$ , the number of teeth  $z$  and distances  $u$  and  $x_a$

(Fig. 4). The change of angular displacement is written as  $d\varphi = \omega dt = 2\pi \frac{n}{60} dt$ . The gear torques are generated by  $F_p$  multiplied by moment arm  $l$  and can be expressed as (Fig. 4) [9]:

$$T_{1,2} = F_p \cdot l = \Delta p \cdot b \cdot h \cdot \frac{k}{2} = p \cdot \frac{b}{2} \cdot \left[ \left( \frac{D_{out}}{2} \right)^2 - \left( \frac{D_{out}}{2} \cdot \frac{2}{z+2} \right)^2 \pm \frac{D_{out} \cdot 2x_a}{z+2} - u^2 \right], \quad (11)$$

$k$  is the length of the projected area of the gear which is not pressurized due to meshing of the teeth and  $h$  is the length of the pressurized area (Fig. 4).  $k$  and  $h$  are expressed in  $D_{out}$ ,  $z$ ,  $u$  and  $x_a$  (Appendix A1). Subsequently, Eq. (10) is rewritten and filled out with Eq. (11) and  $d\varphi$  to yield  $dV$  [9]:

$$dV = b \cdot \pi \frac{n}{30} \left[ \left( \frac{1}{2} D_{out} \right)^2 - \left( D_{out} \frac{z}{2(z+2)} \right)^2 - u^2 \right] \cdot dt. \quad (12)$$

Second,  $dV$  changes over the interlocking trajectory of two teeth. For the period of continuous interlocking of these teeth, the tooth pair has to interlock from  $u = -w/2$  till  $u = w/2$  with  $w$  being the transverse base pitch [18] (Fig. 4). The  $V_m$  of the teeth pair over the interlocking trajectory is calculated by integrating Eq. (12) over time [9]:

$$V_m = \int_{-w/2}^{w/2} dV = b \cdot 2\pi \cdot \left( \frac{D_{out}}{z+2} \right)^2 \cdot \frac{z + \sin^2 \gamma}{z}. \quad (13)$$

Solving the integral requires  $u$  and  $w$  to be expressed in gear dimensions (Appendix A2). Finally,  $Q$  is obtained as follows [16]:

$$Q = z \cdot \frac{n}{60} \cdot V_m = \frac{n \cdot b \cdot \pi}{30} \cdot \left( \frac{D_{out}}{z+2} \right)^2 \cdot (z + \sin^2 \gamma). \quad (14)$$

Filling out the set and chosen values of the geometric parameters as presented in Table 2 in Eq. (14), a fluid flow  $Q$  of 0.001 L/s is obtained. With  $Q$  and  $P$  known,  $\Delta p$  is calculated with Eq. (1) to be  $11.5 \times 10^5$  Pa.

### 3.1.2 Gear Ring Motor

The gear ring motor works by an eccentric inner gear ring (called “pinion”) that interlocks with the outer gear ring on one side (Fig. 3). The pinion has one tooth less than the gear ring and rotates as well as the gear ring (gerotor principle). This principle makes use of trochoid toothing which guarantees a seal between the inner and outer teeth and creates a moving displacement volume ( $V_s = A_s \cdot b$ ) opposite the

interlocking teeth (Fig. 5) [9]. Next, we define  $z$  as the number of teeth of the gear ring. Notice that the pinion always has one tooth less than the gear ring, hence  $z_p = z - 1$  [9].

The general formula of  $Q$  is given by the first part of Eq. (14) with the difference that  $V_s$  is approximated by displacement volume  $V_p = A_p \cdot b$  as follows (Fig. 5) [9]:

$$Q = z_p \cdot \frac{n}{60} \cdot V_p = z_p \cdot \frac{n}{60} \cdot 2e \cdot \frac{\pi \cdot D}{z_p} \cdot k_a \cdot b, \quad (15)$$

where  $e$  is the eccentricity and  $k_a$  is a correction factor that takes into account the small error that is introduced by the approximation.  $k_a$  can be expressed in  $z$  and  $x_c$  ( $\approx 0.125$ ) [9]:

$$k_a = \frac{A_p}{A_s} = \left( \frac{z_p}{z} \right)^{x_c}. \quad (16)$$

The values for  $k_a$  and the set design parameters from Table 2 were filled out in Eq. (15) to obtain a fluid flow of  $5.4 \times 10^{-4}$  L/s. With  $Q$  and  $P$  known,  $\Delta p$  is calculated with Eq. (1) to be  $21.7 \times 10^5$  Pa.

### 3.2 Hydrodynamic Turbines

Hydrodynamic turbines can be divided into reaction and impulse turbines (Fig. 6) [10]. Reaction turbines exist in axial and radial configurations and are fully submerged [10]. The water is accelerated or

**Table 2.** Parameters that were used to calculate  $n$ ,  $Q$  and  $\Delta p$  for the actuators. The actuators' diameters ( $D_{out}$  and  $D_{in}$ ) and width  $b$  were derived from the set requirements; the number of teeth ( $z$  and  $z_p$ ), the various blade angles and  $k_v$  were chosen to reach the highest efficiency

Actuator	$D_{out}$ [m]	$D_{in}$ [m]	$b$ [m]	$z$	$z_p$	$\gamma$ [°]
External gear	0.005	-	0.005	5	-	20 [18]
Gear ring	0.004	-	0.005	6	5	20 [18]
					$\beta_{in}$ [°]	$\beta_{out}$ [°]
Axial turbine	0.005	0.002	-	90	78	1.2
Radial turbine	0.005	0.002	0.005	90	70	1.2
				$D_j$ [m]		
Pelton wheel	0.005	0.003	-	0	-	-
Ossb. turbine	0.005	0.003	-	-	16 [20]	-

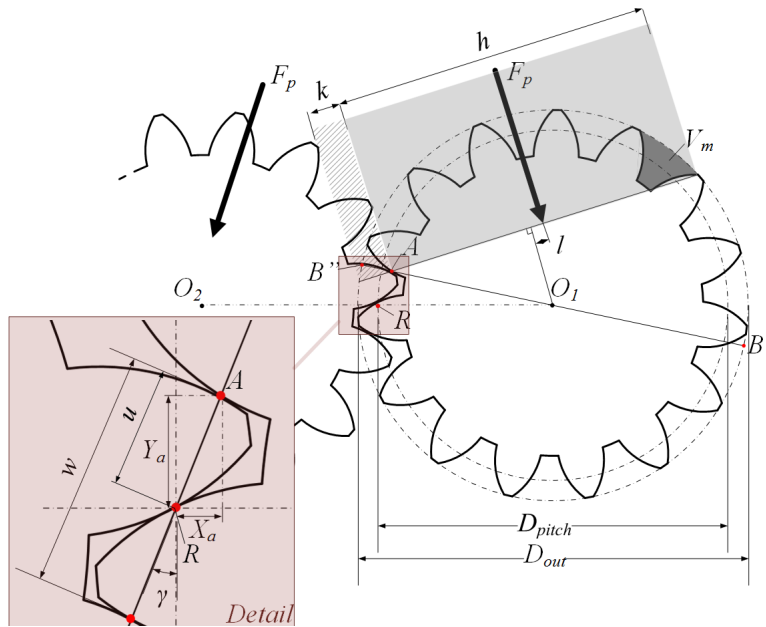


**Fig. 4.** Definition of the important geometric parameters of the external gear motor; the hydrostatic pressure area is indicated by light grey, the area of no pressure due to meshing of the teeth is hatched. Indicated are the distributed force  $f_p$ , the moment arm  $l$ , the roll point  $R$ , the contact point  $A$ , the gear centres ( $O_1$  and  $O_2$ ), the mean displacement area  $V_m$ , distances  $h$  and  $k$ : part of the interlocking teeth are enlarged in a detail drawing showing points  $R$  and  $A$ , pressure angle  $\gamma$  and distances  $u$  and  $w$ ; adapted from [9]

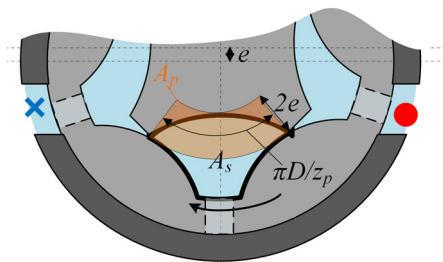


**Fig. 5.** Cross section of a part of the gear ring motor; both gear rings (light grey) rotate in clockwise direction in the housing (dark grey); pressurized fluid enters the motor on the right (red dot) and enters the displacement volume via internal channels distributed along the gear ring; the fluid leaves the motor at the left side (blue cross); part of the pinion is shown that entraps the displacement area  $A_s$  (thick lines) together with the outer gear ring; the approximate displacement area  $A_p$  is coloured orange (thin lines); adapted from [9]

blades. This results in a force on the bucket blade that together with the wheel's diameter creates a torque on the turbine wheel (Figs. 6 and 7). The impulse turbines

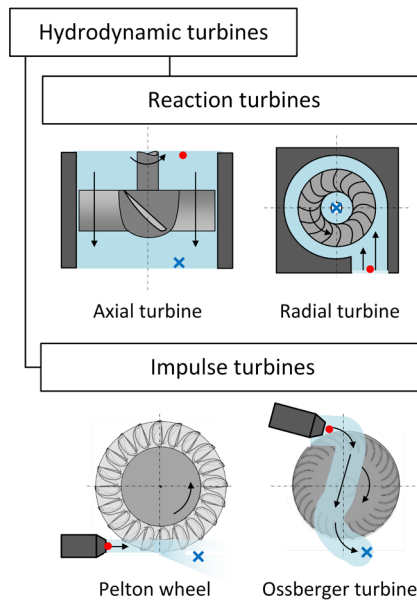


**Fig. 6.** Overview of hydrodynamic turbines; for each, a section view is presented indicating the fluid (light blue), the stationary parts (dark grey), the rotating parts (light grey), the fluid inlet (red dot) and the fluid outlet (blue cross); adapted from [10]

decelerated over the blades. The force that causes the acceleration and deceleration is generated by the fluid pressure. The result is that the fluid velocity is changed from inlet to outlet. The impulse turbines operate at atmospheric pressure. Two types are present: the Pelton wheel and Ossberger turbine (Fig. 6). The working principle is that the water's pressure (potential energy) is converted to water's kinetic energy by a nozzle that causes a water jet to hit the

do not require a housing, whereas reaction turbines require a housing since they are fully submerged.

As the total pressure drop takes place in the nozzle, impulse turbines do not require a housing. Despite their different nature of energy transfer, the mathematical descriptions of reaction and impulse turbines are described in analogy to yield the  $n$  and  $Q$ . Since  $T$  is dependent on  $n$ , the set torque is used to calculate the rotational speed.

### 3.2.1 Radial Turbine

Following the general approach, first  $Q$  is calculated with Eq. (4) [10]. This requires  $C_{Rout}$  to be expressed as a function of  $n$  (see Appendix B1: Eq. (36)). The direction of the absolute inlet and outlet fluid velocity  $C_{in}$  and  $C_{out}$  on one blade is indicated by solid thick arrows (Fig. 7). The turbine velocities at the inner and outer part of the blades are  $U_{in}$  and  $U_{out}$  (at half of the diameter  $D_{in}$  vs.  $D_{out}$ ). The absolute velocities are decomposed into a tangential  $C_{Tin}$  and  $C_{Tout}$ , and in the case of an axial turbine axial components  $C_{Ain}$  and  $C_{Aout}$  or in case of a radial turbine in radial components  $C_{Rin}$  and  $C_{Rout}$  indicated by dotted green arrows. The fluid inlet and outlet angles  $\alpha_{in}$  and  $\alpha_{out}$  and blade angles  $\beta_{in}$  and  $\beta_{out}$  are needed for this decomposition. Finally, the fluid velocities relative to the turbine  $c_{in}$  and  $c_{out}$  are derived and indicated by striped arrows.  $C_{Rout}(n)$  is substituted in Eq. (4):

$$Q(n) = \frac{1}{k_v} \cdot \frac{D_{in} \cdot \pi \cdot n}{60} \cdot \tan(180^\circ - \beta_{out}) \cdot D_{in} \cdot \pi \cdot b. \quad (17)$$

Second, to express  $T(n)$ , all fluid velocities  $C_{Rout}$ ,  $C_{Tout}$ ,  $C_{Rin}$ , and  $C_{Tin}$  are described as function of  $n$  (see Appendix B1). Substituting Eq. (17) and (39) and  $C_{Tout}=0$  in Eq. (6) yields:

$$T(n) = \frac{\pi \cdot b \cdot k_\beta \cdot D_{in}^2 \cdot D_{out}^2}{2k_v} \tan(180^\circ - \beta_{in}) \cdot \rho \cdot \left(\frac{\pi \cdot n}{60}\right)^2, \quad (18)$$

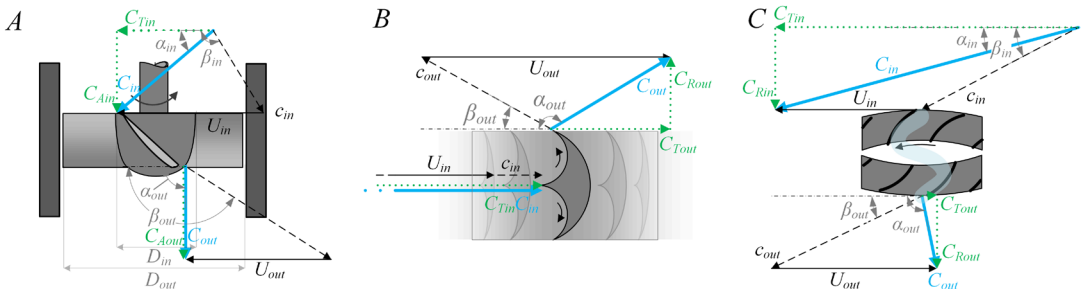


Fig. 7. Velocity profiles of a) an axial turbine, b) a Pelton wheel and c) an Ossberger turbine; adapted from [10]

$k_\beta$  is the constant factor calculated from the in- and outlet blade angles. Finally,  $\Delta p$  was determined by substituting Eqs. (36), (38) and (40) in Eq. (8):

$$\Delta p = \frac{D_{out}^2 \cdot k_{\beta 2} \left(1 - \frac{1}{2} \cdot k_{\beta 2}\right)}{4} \cdot \rho \cdot \left(\frac{2\pi \cdot n}{60}\right)^2 - \frac{\tan(180^\circ - \beta_{out})^2}{8} \left(\left(\frac{1}{k_v} \cdot \frac{D_{in}^2}{D_{out}}\right)^2 - D_{in}^2\right) \cdot \rho \cdot \left(\frac{2\pi \cdot n}{60}\right)^2. \quad (19)$$

The set torque and the values of the input parameters (Table 2) were filled out in Eq. (18) to give an  $n$  of 55160 rpm. The value of  $n$  was used to calculate  $Q$  with Eq. (17): 0.42 L/s. Finally, filling out all values in Eq. (19) yields a  $\Delta p$  of  $2.1 \times 10^5$  Pa.

### 3.2.2 Axial Turbine

Following the general approach, first  $Q$  is calculated with Eq. (4) [10]. This requires  $C_{Aout}$  to be expressed as a function of  $n$  (see Appendix B2: Eq. (43)) and substituted in Eq. (4):

$$Q(n) = \frac{1}{k_v} \cdot \frac{D_{out} + D_{in}}{2} \cdot \frac{\pi \cdot n}{60} \cdot \tan(180^\circ - \beta_{out}) \cdot \frac{\pi}{4} (D_{out}^2 - D_{in}^2). \quad (20)$$

Second, to express  $T(n)$ , all fluid velocities  $C_{Aout}$ ,  $C_{Tout}$ ,  $C_{Ain}$ , and  $C_{Tin}$  are described as function of  $n$  (see details Appendix B2). Substituting Eqs. (20) and (44) and  $C_{Tout}=0$  in Eq. (6) yields:

$$T(n) = \frac{\pi \cdot D_{out} \cdot k_\beta \cdot \tan(180^\circ - \beta_{out})}{8k_v} \cdot \frac{D_{out} + D_{in}}{4} \cdot (D_{out}^2 - D_{in}^2) \cdot \rho \cdot \left(\frac{2\pi \cdot n}{60}\right)^2. \quad (21)$$

Finally,  $\Delta p$  was determined. First, the absolute fluid velocities were calculated using the Pythagorean theorem (Fig. 7a). Second, Eqs. (43) and (44) and the absolute fluid velocities were filled out in Eq. (8):

$$\Delta p = k_\beta \cdot \left(1 - \frac{\rho}{2} \cdot k_\beta\right) \cdot \left(\frac{D_{out} + D_{in}}{4}\right)^2 \cdot \left(2\pi \cdot \frac{n}{60}\right)^2. \quad (22)$$

The set torque and the values of the input parameters (Table 2) were filled out in Eq. (21) to give an  $n$  of 62825 rpm. The value of  $n$  was used to calculate  $Q$  with Eq. (20): 0.74 L/s. Finally, filling out all values in Eq. (22) gives a  $\Delta p$  of  $15.3 \times 10^5$  Pa.

### 3.2.3 Pelton Wheel

$Q$  is fully defined by the absolute inlet fluid velocity  $C_{in}$  and the nozzle diameter  $D_j$  [19]:

$$Q = C_{in} \cdot \pi \left(\frac{D_j}{2}\right)^2. \quad (23)$$

Using Fig. 7b, the tangential inlet and outlet velocities are determined [19]:

$$C_{Tin} = C_{in}, \quad (24)$$

$$C_{Tout} = c_{out} \cdot \cos(\beta_{out}) - U_{out}. \quad (25)$$

With the bucket velocity  $U_{out}$  is defined as  $\frac{D}{2} \cdot 2\pi \cdot \frac{n}{60}$ , and  $c_{out}$  is the outlet water jet velocity relative to the bucket velocity.  $C_{in}$  is set to  $2U_{out}$ , since this ratio gives the maximum output power [19]. Since  $C_{in}$  is twice  $U_{out}$ ,  $C_{out}$  of the emerging water jet in the plane of the wheel is zero (provided that  $\beta_{out}=0$ ). This means that the complete momentum of the inlet water jet is transferred into work and water will effectively fall off the trailing edge of the buckets. With this assumption,  $T(n)$  can be fully expressed:

$$T(n) = C_{in} \cdot \pi \left(\frac{D_j}{2}\right)^2 \cdot \rho \cdot \frac{D}{2} \cdot (C_{in} + (c_{in} \cdot \cos(\beta_{out}) - U_{out})) = \pi \left(\frac{D_j}{2}\right)^2 \cdot \frac{D^3}{4} \cdot (1 + \cos(\beta_{out})) \cdot \rho \cdot \left(2\pi \cdot \frac{n}{60}\right)^2. \quad (26)$$

The set torque and the values of the input parameters (Table 2) were filled out in Eq. (26) to give an  $n$  of 22716 rpm. The value of  $n$  was used to calculate  $Q$  with Eq. (23): 0.08 L/s. Finally,  $\Delta p$  over the blades is zero, since a velocity difference is absent between inlet and outlet water jet.

### 3.2.4 Ossberger Turbine

The Ossberger turbine (often referred as cross-flow or Banki turbine) consists of a nozzle and a turbine runner (Fig. 6). It has a high efficiency at low flow

rates. Typically, the water jet enters the runner at an angle of 16 degrees to the tangent of the periphery of the wheel [20].  $Q(n)$  and  $T(n)$  determined with the same approach as used for the Pelton wheel. In fact,  $Q(n)$  is described by Eq. (23).

Using Fig. 7c, the tangential velocities of the in- and outlet waterjet are described [20]:

$$C_{Tin} = C_{in} \cdot \cos(\alpha_{in}), \quad (27)$$

$$C_{Tout} = c_{out} \cdot \cos(\beta_{out}) - U_{out}. \quad (28)$$

With the bucket velocity  $U_{out}$  is defined as  $n \cdot D/2$ , and  $\alpha_{in}$  is the inlet angle of the waterjet.  $C_{in}$  is set to  $2U_{out}/\cos\alpha_1$ , since this ratio gives the maximum output power [20]. With these equations,  $T(n)$  is described as:

$$T(n) = \frac{D \cdot n}{\cos\alpha_1} \cdot \pi \left(\frac{D_j}{2}\right)^2 \cdot \rho \cdot (C_{in} \cdot \cos(\alpha_{in}) + c_{out} \cdot \cos(\beta_{out}) - U_{out}) \cdot \frac{D}{2} = \pi \left(\frac{D_j}{2}\right)^2 \cdot \frac{D^3}{2\cos\alpha_1} \cdot \rho \cdot \left(2\pi \cdot \frac{n}{60}\right)^2. \quad (29)$$

The set torque and the values of the input parameters (Table 2) were filled out in Eq. (29) to give an  $n$  of 22272 rpm. The value of  $n$  was used to calculate  $Q$  with Eq. (23): 0.09 L/s. Finally,  $\Delta p$  over the blades is zero.

## 3.3 Results Summary

An overview of the calculated rotational speed, flow and pressure difference for each of the hydraulic actuators is given in Table 3. Due to their different working principles, a difference between hydrostatic motors and hydrodynamic turbines is that the required drilling torque requires a relative high pressure or a high rotational speed and flow, respectively. An exception is the axial turbine which requires both a high  $n$  and  $\Delta p$ .

**Table 3.** Overview of calculated rotational speed  $n$ , fluid flow  $Q$  and pressure difference  $\Delta p$  for the set torque, dimensions and power

		$n$ [rpm]	$Q$ [L/s]	$\Delta p$ [Pa]
Hydrostatic motors	External gear	750	0.001	$11.5 \times 10^5$
	Gear ring	750	0.0006	$21.7 \times 10^5$
Hydrodynamic turbines	Axial turbine	62825	0.74	$15.3 \times 10^5$
	Radial turbine	55160	0.42	$2.1 \times 10^5$
	Pelton wheel	22716	0.08	0
	Ossberger turbine	22272	0.09	0

## 4 DISCUSSION

Literature on miniature hydraulic actuators for medical or other applications was not found. Therefore, six conventional hydraulic actuators [8] to [11] were analysed for their applicability in the proposed concept for the compliant bone drill. The medical case of microfracture technique posed a worst-case design scenario: bone is the toughest human tissue to drill, posing a high demand for the required drilling torque and power and the human joint space is very tight, posing a high demand for actuator miniaturization. Following the proposed theoretic approach, the rotational speed, fluid flow and pressure difference were calculated (Table 3). Based on these results, all hydrodynamic turbines are discarded, since they do not meet the set maximum rotational speed of 750 rpm. The need for a high rotational speed of the hydrodynamic turbines is explained by Eqs. (6), (18), (21), (26) and (29). The torque is dependent on the rotational speed and the dimensions of the turbine. Since the dimensions need to be small (Table 2), the rotational speed needs to be high [10] and [11]. Eventually, we found one example of a miniature hydraulic turbine applied in a dental drill 'Kern Turbojet' with  $n$  of 61000 rpm (later reduced to 45000 rpm) and  $Q$  of 0.10 L/s [21]. This product was not a success, because of its bulkiness and low torque. This finding confirms our calculations and our suggestion to proceed with hydrostatic motors.

The hydrostatic external gear and gear ring motors can generate the set torque and dimensions with reasonable values of the pressure difference (Eq. (4)). The rotational speed  $n$  can be set without affecting the required torque [9]. Comparing the external gear motor and the gear ring motor, two aspects are in favour of the external gear motor: the twice-as-low-than-required pressure difference that adds to the safety margin of the housing and gear materials (Table 3), and the simplicity of the design that consists of two gears and a housing. Consequently, this theoretical approach suggests that the external gear motor is most suited to implement in a design for a compliant bone drill.

This theoretical approach poses limitations. First, the efficiency of the actuators was not taken into account. We do expect that the small dimensions will induce relatively high losses that significantly influence the actual required flow and pressure difference [8]. However, since all constructive working principles were miniaturized to the same scale and the losses are assumed to be more or less equal, the relative theoretical comparison as presented

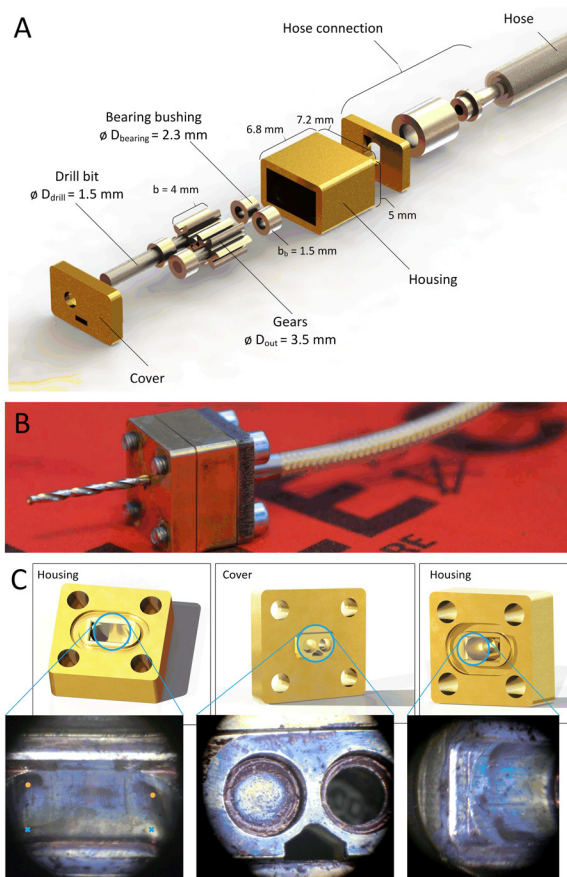


**Fig. 8.** a) Exploded view of external gear motor prototype with main dimensions, b) assembled prototype, and c) results of leakage test with ink residue left on the axial leakage gap on the cover (middle) and the radial leakage gap of the housing (left and right); more ink residue is present on the outlet side (red dot) than on the inlet side of the actuator (blue cross)

is still useful. Second, we did not alter the designs of the six hydraulic actuators to generate outcome values that would closer match the requirements. This is defensible as one would need to fully redesign all six hydraulic actuators, which was not the scope of this study. However, the designs that required quite some small parts beforehand (Fig. 3) were not included for further analysis. Additionally, the blade angles, pressure angle, teeth, and correction factor (Table 2) were chosen such that they would yield the most favourable theoretical outcome. A quick sensitivity analysis of those values indicates that the order of magnitude of the calculated outcome parameters remains the same. However, it is unclear if these values can be achieved in an actual design. Finally, the set value of 750 rpm for the rotational speed was chosen partly because of the lack of available data of the torque for lower speeds [15]. For bone drilling

without the risk of necrosis, even lower speeds would be recommended [22] with the consequence of a nonlinear increase of the required torque. Still, the external gear motor would compare favourably with the difference that the required pressure difference would increase.

Obviously, the presented analysis is the first important step in developing a compliant hydropowered bone drill. The next step would be to build and to test a miniature external gear motor. Fig. 8 presents an on-scale prototype for which we performed leakage, friction and pressure drop tests. The tests confirmed the challenges to cope with losses, critical geometric and surface tolerances. The prototype's tolerances (H6/h6 fit and clearance of 0.0016 mm) and material (brass Ms58 grade and stainless steel 304 grade) were not suitable to achieve a proper working actuator. Further constructive development is required, but this is out of the scope of this paper. The losses in terms of reduced efficiency are acceptable for the intended medical application, but the expected higher required pressure difference could compromise safety. The fact that the energy can be transferred through a compliant hose does provide an advantage above conventional mechanical solutions that are actuated by electromotors.

## 5 CONCLUSIONS

To the best of the authors' knowledge, no systematic analysis of hydraulic actuators has been presented before. The strength of this analysis is that the derived equations can be applied independently from our intended application and complementary requirements to select a hydraulic actuator for other applications. Based on the set requirements for a compliant bone drill, the external gear motor was selected to provide the highest potential.

## 6 NOMENCLATURE

$\gamma$  pressure angle, [°]  
 $\alpha_{in}$  fluid inlet angle, [°]  
 $\alpha_{out}$  fluid outlet angle, [°]  
 $\beta_{in}$  blade inlet angle, [°]  
 $\beta_{out}$  blade outlet angle, [°]  
 $\Delta p$  pressure difference, [Pa]  
 $\Delta C$  velocity difference, [m/s]  
 $OA$  distance contact point - gear centre point, [m]  
 $d\varphi$  change of angular displacement, [rad]  
 $\rho$  density, [kg/m<sup>3</sup>]  
 $A_k$  effective area [m<sup>2</sup>] or water jet area, [m<sup>2</sup>]  
 $A_p$  approximated gear ring displacement area, [m<sup>2</sup>]

$A_s$  gear ring displacement area, [m<sup>2</sup>]  
 $B$  drill type constant, [-]  
 $b$  gear width or turbine width, [m]  
 $c$  fluid velocity relative to turbine, [m/s]  
 $C_{in}$  inlet fluid velocity, [m/s]  
 $C_{out}$  outlet fluid velocity, [m/s]  
 $C_A$  axial component of the fluid velocity, [m/s]  
 $C_R$  radial component of the fluid velocity, [m/s]  
 $C_T$  tangential component of the fluid velocity, [m/s]  
 $D$  diameter, [m]  
 $D_{drill}$  drill diameter, [m]  
 $D_{in}$  inner diameter, [m]  
 $D_j$  nozzle diameter, [m]  
 $D_{pitch}$  pitch diameter, [m]  
 $D_{out}$  outer diameter, [m]  
 $dW$  instantaneous work, [J]  
 $dV$  instantaneous displacement volume, [m<sup>3</sup>]  
 $e$  eccentricity, [m]  
 $f$  drilling feed, [mm/rev]  
 $F$  force, [N]  
 $F_p$  force exerted by fluid pressure, [N]  
 $F_{thrust}$  thrust force, [N]  
 $h$  length of the pressure area ( $A_k$ ), [m]  
 $j$  drill type constant, [-]  
 $k$  length of the projected area of the gear which is not pressurized due to meshing of the teeth, [m]  
 $k_\beta$  constant factor of the in- and outlet blade angles, (Appendix B1)  
 $k_a$  area difference correction factor, [-]  
 $k_v$  vane volume correction factor, [-]  
 $l$  moment arm, [m]  
 $m$  mass, [kg]  
 $n$  rotational speed, [rpm]  
 $P$  power, [W]  
 $R$  roll point, [-]  
 $p_{in}$  inlet pressure, [Pa]  
 $p_{out}$  outlet pressure, [Pa]  
 $Q$  flow, [m<sup>3</sup>/s]  
 $T$  torque, [Nm]  
 $w$  transverse base pitch, [m]  
 $u$  distance roll point – contact point, [m]  
 $U_{in}$  inlet turbine velocity, [m/s]  
 $U_{out}$  outlet turbine velocity, [m/s]  
 $V$  displacement volume, [m<sup>3</sup>]  
 $V_m$  mean displacement volume, [m<sup>3</sup>]  
 $w$  transverse base pitch, [m]  
 $x$  drill type constant, [-]  
 $x_A$  horizontal contact point distance, [m]  
 $x_c$  area correction factor coefficient, [-]  
 $y_A$  vertical contact point to distance, [m]  
 $y$  drill type constant, [-]  
 $z$  number of gear teeth, [-]  
 $z_p$  number of pinion teeth, [-]

7 REFERENCES

[1] Steadman, J.R., Rodkey, W G., Briggs, K.K. (2010). Microfracture: Its history and experience of the developing surgeon. *Cartilage*, vol. 1, no. 2, p. 78-86, DOI:10.1177/1947603510365533.

[2] Van Bergen, C.J.A., De Leeuw, P.A.J., Van Dijk, C.N. (2009). Potential pitfall in the microfracturing technique during the arthroscopic treatment of an osteochondral lesion. *Knee Surgery, Sports Traumatology. Arthroscopy*, vol. 17, no. 2, p. 184-187, DOI:10.1007/s00167-008-0594-y.

[3] Yan Nai, T., Herder, J.L., Tuijthof, G.J. M. (2011). Steerable mechanical joint for high load transmission in minimally invasive instruments. *Journal of Medical Devices, Transactions of the ASME*, vol. 5, no. 3, p. 034503-034503-6, DOI:10.1115/1.4004649.

[4] den Dunnen, S., Mulder, L., Kerkhoffs, G.M.M.J., Dankelman, J., Tuijthof, G.J.M. (2013). Waterjet drilling in porcine bone: The effect of the nozzle diameter and bone architecture on the hole dimensions. *Journal of the Mechanical Behavior of Biomedical Materials*, vol. 27, p. 84-93, DOI:10.1016/j.jmbm.2013.06.012.

[5] Hacker, R.L., Van Wyk, R.A., Heisler, G.R., (2011). *Rotary SHAVER with Improved Connection between Flexible and Rigid Rotatable Tubes*. U.S. Patent 7993360., USPTO, Washington.

[6] Fucci, J., Dinger, F.B., Trott, A.F., Adams, K.M., Mazurek, W.F. (1995). *Bendable Variable Angle Rotating Shaver*. U.S. Patent 5411514, USPTO, Washington.

[7] Daniel, S.C., Juknelis, A.J., Kauker, B.J., (1995). *Arthroscopic cutter Having Curved Rotatable Drive*. U.S. Patent 5437630A, USPTO, Washington.

[8] White, F.M. (2008). *Fluid Mechanics*. McGraw-Hill, New-York.

[9] Ivantysyn, J., Ivantysynova, M. (1993). *Hydrostatische Pumpen und Motoren: Konstruktion und Berechnung*. Vogel Business Media, Würzburg.

[10] Bohl, W. (1994). *Strömungsmaschinen 1-Aufbau und Wirkungsweise*. Vogel Business Media, Würzburg.

[11] Dixon, S.L. (2005). *Fluid Mechanics and Thermodynamics of Turbomachinery*. Butterworth-Heinemann, Oxford.

[12] Dowdy, P.A., Watson, B.V., Amendola, A., Brown, J.D. (1996). Noninvasive ankle distraction: Relationship between force, magnitude of distraction, and nerve conduction abnormalities. *Arthroscopy: The Journal of Arthroscopic and Related Surgery*, vol. 12, no. 1, p. 64-69, DOI:10.1016/S0749-8063(96)90221-2.

[13] Tuijthof, G.J.M., Herder, J.L., Van Dijk, C. N., Pistecky, P.V. (2004). A compliant instrument for arthroscopic joint fusion. *Proceedings of the ASME Design Engineering Technical Conference*, p. 397-405, DOI:10.1115/DETC2004-57148.

[14] Wiggins, K.L., Malkin, S. (1976). Drilling of bone. *Journal of Biomechanics*, vol. 9, no. 9, p. 553-559, DOI:10.1016/0021-9290(76)90095-6.

[15] Jacob, C.H., Berry, J.T., Pope, M.H., Hoaglund, F.T. (1976). A study of the bone machining process-Drilling. *Journal of Biomechanics*, vol. 9, no. 5, p. 343-349, DOI:10.1016/0021-9290(76)90056-7.

[16] Tuijthof, G.J.M., Frühwirth, C., Kment, C. (2013). Influence of tool geometry on drilling performance of cortical and

trabecular bone. *Medical Engineering and Physics*, vol. 35, no. 8, p. 1165-1172, DOI:10.1016/j.medengphy.2012.12.004.

[17] Sezek, S., Aksakal, B., Karaca, F. (2012). Influence of drill parameters on bone temperature and necrosis: A FEM modelling and in vitro experiments. *Computational Materials Science*, vol. 60, p. 13-18, DOI:10.1016/j.commatsci.2012.03.012.

[18] Maitra, G.M. (1994). *Handbook of Gear Design*. Tata McGraw-Hill Education, Nodia.

[19] Amberger, R. (2014). Pelton wheel water turbine. from: <http://people.rit.edu/rfaite/courses/tflab/Cussons/pelton/pelton.htm>, accessed on 13-06-2014.

[20] Mockmore, C.A., Merryfield, F. (1949). *The Banki Water Turbine. Bulletin Series*, no. 25, Engineering Experiment Station, Oregon State System of Higher Education, Oregon.

[21] Stephens R.R. (1987). Dental handpiece history. *Australian Dental Journal*, vol. 32, no. 1, p. 58-62, DOI:10.1111/j.1834-7819.1987.tb01279.x.

[22] Soriano, J., Garay, A., Aristimu-o, P., Iriarte, L.M., Eguren, J.A., Arrazola, P.J. (2013). Effects of rotational speed, feed rate and tool type on temperatures and cutting forces when drilling bovine cortical bone. *Machining Science and Technology*, vol. 17, no. 4, p. 611-636, DOI:10.1080/10910344.2013.837353.

8 APPENDIX A1 EXTERNAL GEAR MOTOR

Distances  $k$  and  $h$  were rewritten in two steps. First, using the intersection cord theorem, the multiplication of  $h$  and  $k$  (Eq. (11)) is expressed as [9]:

$$h \cdot k = \overline{AB'} \cdot \overline{AB''} = \left(\frac{1}{2} D_{out} + \overline{O_1A}\right) \cdot \left(\frac{1}{2} D_{out} - \overline{O_1A}\right) = \left(\frac{1}{2} D_{out}\right)^2 - \overline{O_1A}^2. \quad (30)$$

Second, a local coordinate system is placed in roll point  $R$  (Fig. 4) defining  $u$  as the distance of point  $A$  to point  $R$ .  $\overline{O_1A}$  is expressed following the Pythagorean theorem and by substituting  $D_{pitch}$  with  $D_{out} \cdot z / (z+2)$  (Fig. 4):

$$\overline{O_1A}^2 = \left(\frac{1}{2} D_{pitch} - x_A\right)^2 + y_A^2 = \left(D_{out} \cdot \frac{z}{2(z+2)}\right)^2 - D_{out} \cdot \frac{z}{z+2} \cdot x_A + u^2. \quad (31)$$

Analogously,  $\overline{O_2A}$  is derived for the second gear:

$$\overline{O_2A}^2 = \left(\frac{1}{2} D_{pitch} + x_A\right)^2 + y_A^2 = \left(D_{out} \cdot \frac{z}{2(z+2)}\right)^2 + D_{out} \cdot \frac{z}{z+2} \cdot x_A + u^2. \quad (32)$$

Finally, Eqs. (31) and (32) are filled out in Eq. (30), which in turn is filled out in Eq. (11).

9 APPENDIX A2 GEAR RING MOTOR

To solve the integration of Eq. (13) some parameters need to be expressed in the gear dimensions. For involute gear, point *A* moves with a constant speed over the line of action that equals the direction of *u* (Fig. 4) [9]:

$$\frac{du}{dt} = D_{out} \frac{z}{2(z+2)} \leq \cos \gamma \cdot 2\pi \cdot \frac{n}{60}. \quad (33)$$

With  $\gamma$  is the pressure angle (Fig. 4). Eq. (33) is rewritten to express *dt* in *du*. Furthermore, for involute gear with equal teeth and no profile shift, *w* can be expressed as (Fig. 4) [9]:

$$w = \frac{\pi \cdot D_{out}}{z} \cdot \cos \gamma. \quad (34)$$

Substituting the expressions for *dt* and *w* in Eq. (13) allows solving the integral .

10 APPENDIX B1 RADIAL TURBINE

- Using Fig. 2,  $C_{Rout}$  is expressed as [10]:

$$C_{Rout} = U_{out} \cdot \tan(180^\circ - \beta_{out}). \quad (35)$$

Subsequently,  $C_{Rout}$  can be written as function of *n* by substituting  $U_{out}$  as follows [10]:

$$C_{Rout}(n) = \frac{D_{in}}{2} \cdot \frac{2\pi \cdot n}{60} \cdot \tan(180^\circ - \beta_{out}). \quad (36)$$

- Using Fig. 2, the radial inlet fluid velocity ( $C_{Rin}$ ) can be expressed as [10]:

$$C_{Rin} = \frac{Q(n)}{D_{out} \cdot \pi \cdot b}. \quad (37)$$

Substituting Eq. (17) as expression of  $Q(n)$  yields:

$$C_{Rin}(n) = \frac{1}{k_v} \cdot \frac{D_{in}^2}{D_{out}} \cdot \tan(180^\circ - \beta_{out}) \cdot \frac{\pi \cdot n}{60}. \quad (38)$$

- Using Fig. 2, the tangential inlet fluid velocity ( $C_{Tin}$ ) can be expressed as:

$$C_{Tin} = U_{in} - \left( \frac{C_{Rin}(n)}{\tan(180^\circ - \beta_{in})} \right). \quad (39)$$

Subsequently,  $C_{Tin}$  can be written as function of *n* by substituting  $U_{in}$  as and Eq. (38) [10]:

$$C_{Tin} = \frac{D_{out} \cdot \pi \cdot n}{60} \left( 1 - \frac{1}{k_v} \cdot \frac{D_{in}^2}{D_{out}^2} \cdot \frac{\tan(180^\circ - \beta_{out})}{\tan(180^\circ - \beta_{in})} \right) = \frac{D_{out} \cdot \pi \cdot n}{60} \cdot k_\beta. \quad (40)$$

With  $k_\beta$  is de constant term that results from the blade angle configuration.

- Finally, Fig. 2 indicates that  $C_{Tout}$  is zero.

11 APPENDIX B2 AXIAL TURBINE

- Using Fig. 7a, the axial components of the in- and outlet fluid velocities  $C_{Ain}$  and  $C_{Aout}$  are given:

$$C_{Aout}(n) = C_{Ain}(n) = U_{in} \cdot \tan(180^\circ - \beta_{out}). \quad (41)$$

Next, the turbine velocity *U* is described (Fig. 7a) [10]:

$$U_{in} = U_{out} = \frac{1}{2} \cdot \frac{D_{out} + D_{in}}{2} \cdot \frac{2\pi \cdot n}{60}. \quad (42)$$

Substituting Eq. (42) in Eq. (41) yields:

$$C_{Tin} = \frac{D_{out} + D_{in}}{2} \cdot \frac{\pi \cdot n}{60} \left( 1 - \frac{\tan(180^\circ - \beta_{out})}{\tan(180^\circ - \beta_{in})} \right). \quad (43)$$

- Using Eq. (39) and substituting Eq. (42),  $C_{Tin}$  is [10]:

$$C_{Tin} = \frac{D_{out} + D_{in}}{2} \cdot \frac{\pi \cdot n}{60} \left( 1 - \frac{\tan(180^\circ - \beta_{out})}{\tan(180^\circ - \beta_{in})} \right). \quad (44)$$

- Finally, Fig. 7a indicates that  $C_{Tout}$  is zero, analogous to the radial turbine.

# The Comparison between Two High-Temperature Heat-Pumps for the Production of Sanitary Water

Igor Ivanovski<sup>1</sup> – Darko Goričanec<sup>2</sup> – Julijan Jan Salamunič<sup>3</sup> – Tina Žagar<sup>4,\*</sup>

<sup>1</sup> IVD Maribor, Slovenia

<sup>2</sup> University of Maribor, Faculty of Chemistry and Chemical Engineering, Slovenia

<sup>3</sup> Inter oil d.o.o., Slovenia

<sup>4</sup> Ministry of Economic Development and Technology, Slovenia

*High-temperature heat-pumps are devices that exploit low-temperature heat sources for the production of hot water at high temperatures. This paper presents a comparison between two high temperature heat-pumps for the production of hot sanitary water of temperatures between 65 °C and 85 °C. A high-temperature heat-pump that uses ammonia as a refrigerant and transcritical heat-pump that uses carbon dioxide as a refrigerant were compared in terms of coefficient of performance. Theoretical calculations were based on the REFPROP property method within Aspen Plus software. The simulations showed that the ammonia high-temperature heat-pump outperforms the transcritical heat-pump in terms of coefficient of performance within the evaporation temperature range between -20 °C and 20 °C.*

**Keywords:** heat-pump, sanitary water, coefficient of performance

## Highlights

- Paper presents modelling two high-temperature heat-pumps using REFPROP property method.
- Two refrigerants were compared, ammonia and CO<sub>2</sub> in terms of COP.
- A double stage ammonia heat-pump has a higher COP than the transcritical heat-pump.
- Heat-pump technology is cheaper than the technology of transcritical heat-pumps.

## 0 INTRODUCTION

The EU has set a target to reduce greenhouse gas emissions by 80 % to 95 % until 2050 [1]. Heat-pumps could play an important role in achieving this goal as they are considered as one of the more important decarbonisation technologies for energy systems throughout the world. Traditional heat-pumps are suitable for low-temperature heating systems such as underfloor heating, low-temperature radiators or fan convection heaters. On the other hand, district heating system usually operates at higher temperature regimes. Therefore, high-temperature heat-pumps (HTHP) are suitable for the aforementioned purpose.

HTHP are devices that exploit low-temperature heat sources such as geothermal water, waste heat of refrigerators, industrial sources, etc. in order to produce hot water to be used for heating of buildings, for the production of sanitary hot water or in district heating systems.

HTHP usually employ ammonia as a refrigerant and can be used in many different applications. Kulcar et al [2] reported on exploiting heat from low-temperature geothermal sources. Goričanec et al [3] reported on exploiting low-temperature heat from the generators' cooling system within a hydro power plant. A study on the exploitation of low-temperature energy sources from cogeneration gas

engines was presented in [4]. A semi-empirical model was developed for high pressure twin compressors for the purpose of exploiting waste heat of refrigeration units [5]. A comparison between the installation of electric boilers or HTHP in distributed cogeneration was undertaken in the study on intermittency friendly energy system [6].

On the other hand, transcritical heat-pumps that use natural refrigerant carbon dioxide are getting an increasing attention [7]. Zha et al. [8] investigated a transcritical heat-pump with Voorhees economizer. Tao et al. performed a thermodynamic analysis of an ejector enhanced CO<sub>2</sub> transcritical heat-pump [7]. An expander was used to replace the expansion valve to recover the expansion work in [9] and the influence of nitrogen was studied. Transcritical heat-pumps are suitable for the production of hot sanitary water, which requires a high-temperature lift, as the supercritical fluid is not condensed during the cycle, but it is cooled in the gas cooler.

Carbon dioxide and ammonia are the most promising amongst natural refrigerants, which could replace the refrigerants with global warming potential (GWP). Carbon dioxide has zero ozone depletion potential (ODP) and negligible GWP [9]. On the other hand, ammonia has zero ODP and GWP.

There are a few disadvantages of using ammonia as a refrigerant, such as toxicity and flammability. On

\*Corr. Author's Address: Ministry of Economic Development and Technology, Kotnikova 5, 1000 Ljubljana, Slovenia, tina.krope@gmail.com

the other hand, ammonia has an extremely high latent heat, thus providing more heat flow per unit of mass flow than any other refrigerant used in the traditional compression refrigeration systems [10]. Also the acoustic velocity of ammonia is much higher than any other refrigerant, which means that higher gas velocities can be used in the design of pipes, valves and fittings without incurring substantial pressure losses [10].

The main disadvantages of CO<sub>2</sub> as a refrigerant are high pressure of evaporation and gas cooling, and low theoretical coefficient of performance (COP). Despite of that, CO<sub>2</sub> has excellent transport properties and high compressor efficiency, enabling to obtain high actual COP [11]. CO<sub>2</sub> is also non-toxic, non-flammable, thermally stable, and compatible with other materials.

The goal of this study was to compare two natural refrigerants, ammonia and carbon dioxide for producing sanitary hot water within a high-temperature heat-pump and trans-critical heat-pump, respectively. The comparison was based on COP values, which were calculated during theoretical simulations using Aspen Plus software.

## 1 METHODS

### 1.1 Single Stage HTHP

Single stage HTHP consists of 4 main parts: a compressor, an evaporator, a condenser, and an expansion valve as shown in Fig. 1.

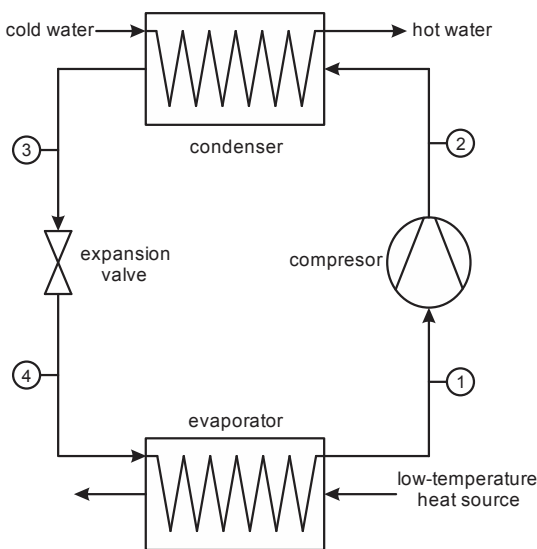


Fig. 1. Process flow diagram of single stage HTHP

The vapour refrigerant is first compressed from an evaporation pressure to a condensation pressure. The vapour is superheated in point 2; further on, it cools to a condensation temperature, then it condenses and further cools down to a discharge temperature in point 3. The heat that is released during vapour cooling, condensation, and liquid sub cooling is transferred to sanitary water. The subcooled liquid refrigerant (point 3) is then reduced in pressure in an expansion valve. After the expansion the refrigerant evaporates in the evaporator. A low-temperature heat source is needed for this process.

### 1.2 Double stage HTHP

Double stage HTHP has an additional compressor and intercooler placed between both compressors as shown in Fig. 2. Cold water is conveyed to the intercooler and then to the condenser of the heat-pump. Double stage HTHP was used for evaporation temperatures below 10 °C. The second compressor is needed because the pressure ratio of a compressor, which is defined as the quotient between the outlet pressure and inlet pressure of a compressor, cannot exceed 5. However, double stage HTHP could also be used for evaporation temperatures above 10 °C, which would lead to higher COP compared to a single stage HTHP because cold vapours require less work to compress.

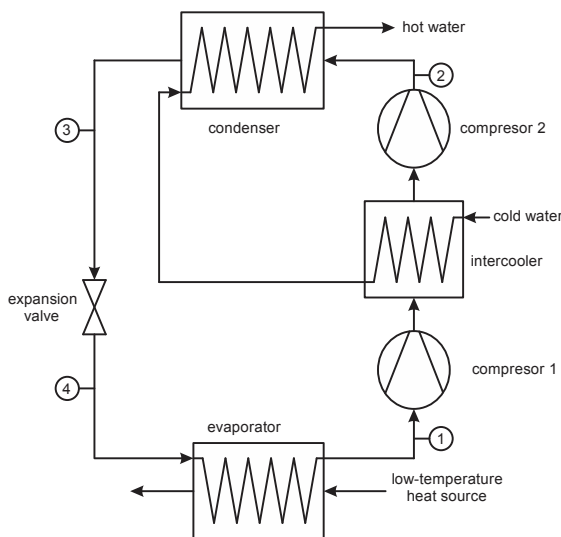


Fig. 2. Process flow diagram of double stage HTHP

### 1.3 Transcritical Heat-Pump

Transcritical heat-pump has nearly the same configuration as single stage HTHP, Fig. 3, except

for an additional internal heat exchanger [8], and it has a gas cooler instead of a condenser. CO<sub>2</sub> is compressed above the critical pressure of 71 bar, and cooled in a gas cooler, where the heat is released over a temperature range.

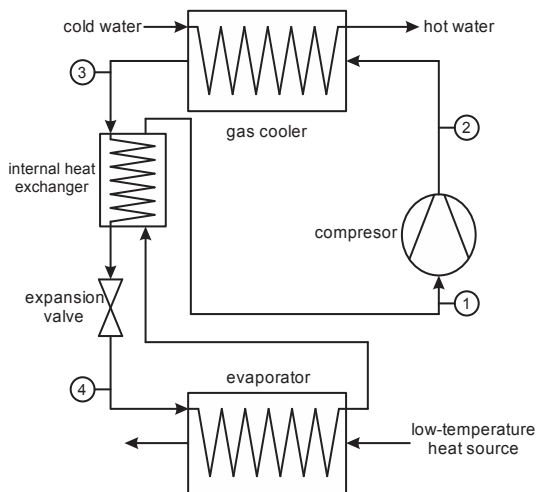


Fig. 3. Process flow diagram of transcritical heat-pump

This is in contrast to the conventional heat-pumps, where the majority of heat is released at a constant temperature. After the gas cooler, the supercritical CO<sub>2</sub> (point 3) is conveyed to an internal heat exchanger, where it is further cooled with the vaporised CO<sub>2</sub> coming from the evaporator. After the reduction in pressure, liquid CO<sub>2</sub> evaporates in the evaporator. The internal heat exchange increases COP of the whole system, because higher temperatures can be obtained at the compressor outlet.

### 1.4 Simulations

In the present study, the following simplifying assumptions were taken into account for the theoretical analysis of both heat-pumps:

- Refrigerant at the evaporator outlet was specified as saturated vapour.
- Zero pressure drop was assumed in all heat exchangers (condensers, gas coolers, evaporators, intercoolers, and internal heat exchanges), and connecting pipes.
- It was assumed that heat losses are negligible.
- An adiabatic, but non-isentropic compression process was assumed with isentropic efficiency of 0.7 [12] and 0.84 [3] and [4] for CO<sub>2</sub> and ammonia compressors, respectively. Mechanical efficiency was set to 0.97 for both compressors.

- The refrigerant temperature at the outlet of the gas cooler was set at 35 °C. It was assumed that ammonia would also be subcooled after condensation in the condenser to the same temperature.
- The temperature of the inlet sanitary water was assumed to be 15 °C.
- Evaporation temperatures were varied between -20 °C and 20 °C. In this temperature range, all types of heat sources could be used such as: geothermal water, heat of refrigeration equipment, and even outside air.
- The amount of produced hot water was fixed at 1.07 kg/s.

Outlet pressure of the high pressure compressor was varied during the simulations of heat-pumps in order to achieve the minimum approach temperatures of 10 °C in the gas cooler/condenser in all simulation cases. The minimum approach temperature in the internal heat exchanger was also set to 10 °C.

REFPROP property method was used for all the simulations within Aspen Plus software program – a versatile modeling tool, which is relatively easy to use when modeling advanced chemical processes and power cycles. It provides a platform for describing different physical/chemical processes. ASPEN Plus can be used for model creation, sensitivity analyses, economics, and optimization. It has a broad physical-chemical property database with many built-in unit models such as compressors, pumps, heaters, heat-exchangers, stream mixers, and stream splitters. In addition, the user can create model blocks based on the Fortran programming language. The REFPROP property method was developed by the National Institute of Standards and Technology (NIST). It is based on highly accurate pure fluid and mixture models. It implements 3 models for the determination of thermodynamic properties of pure fluids: equation of state explicit in Helmholtz energy, the modified Benedict-Webb-Rubin equation of state, and an extended corresponding state model (ESC) [13] and [14].

COP values were calculated according to Eq. (1) for the single-stage HTHP and transcritical heat-pump:

$$COP = \frac{\Phi}{W}, \tag{1}$$

where  $\Phi$  is the rate of heat flow within the gas cooler or condenser [W], and  $W$  is the work required to drive the compressor [W]. Eq. (2) was used for the calculation of the COP of the double-stage high temperature heat-pump:

$$COP = \frac{\Phi_c + \Phi_I}{W_1 + W_2}, \quad (2)$$

where  $\Phi_c$  is the rate of heat flow within the condenser [W],  $\Phi_I$  is the rate of heat flow within the intercooler [W],  $W_1$  is the work required to drive the first compressor [W], and  $W_2$  is the work required to drive the second compressor [W].

The calculations of COP values were done in an MS Excel spreadsheet. Afterwards, graphs were drawn in the same program.

### 3 RESULTS AND DISCUSSION

The condenser of the ammonia HTHP was simulated so that the ammonia was subcooled after condensing. Fig. 4 shows the temperature curves for the condenser of ammonia HTHP at evaporation temperature ( $t_e$ ) of 0 °C and sanitary water temperature ( $t_w$ ) of 75 °C. This enables the full utilisation of the heat of the compressed refrigerant and even a lower compression ratio compared to condensation only. The temperature of the water at the condenser inlet was higher than 15 °C in the case of double stage heat-pump as the water was already partially heated within the intercooler. In order to keep the minimum approach temperatures of 10 °C in the condenser, the outlet pressure of the second compressor needed to be a bit higher than it would be in the case of a single stage heat-pump. Fig. 5 presents the temperature curves for the gas cooler of the transcritical CO<sub>2</sub> heat-pump at evaporation temperature of 0 °C and sanitary water temperature of 75 °C.

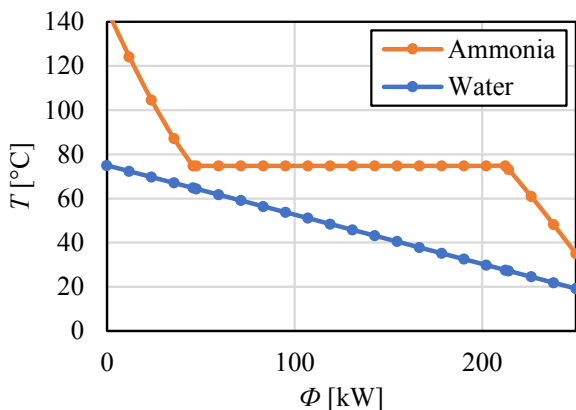


Fig. 4. Temperature curves for the condenser of High temperature heat-pump at  $T_e = 0$  °C;  $T_w = 75$  °C

The refrigerant was cooled to 35 °C in all the cases to allow for a fair comparison between both technologies. In the above mentioned cases water

temperatures and evaporation temperatures are the same. However, the mass flow of the refrigerant that produces the same heat flow rate in the condenser or gas cooler is much bigger in the case of CO<sub>2</sub> by a factor of 7.2 compared to NH<sub>3</sub>.

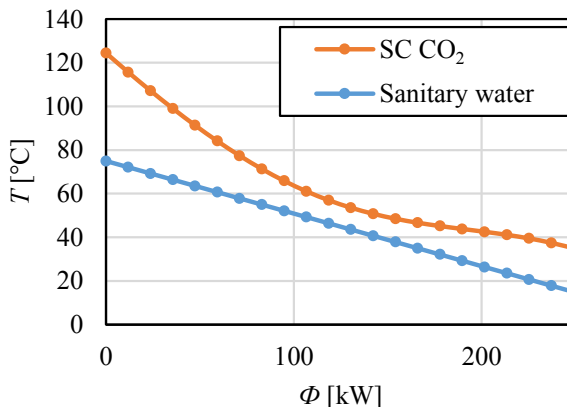


Fig. 5. Temperature curves for the gas cooler of the transcritical CO<sub>2</sub> heat-pump at  $T_e = 0$  °C;  $T_w = 75$  °C

Fig. 6 presents the results of calculations of COP values dependent on the outlet temperatures of hot sanitary water for the transcritical heat-pump using CO<sub>2</sub> as a refrigerant. The simulations were carried out at different refrigerant evaporation temperatures ( $T_e$ ), ranging from -20 °C to 20 °C. It should be noted that all transcritical heat-pump cases were simulated as a single stage heat-pump, meaning that only one compressor was used in the cycle. On the other hand, the ammonia HTHP was simulated as a single stage heat-pump for the evaporation temperatures above 15 °C and as a double stage heat-pump for the evaporation temperatures below 10 °C. Fig. 7 presents the results of calculations of COP values dependent on the outlet temperatures of hot sanitary water for the HTHP that uses ammonia as a refrigerant.

When comparing the results of both simulations, it can be seen that the ammonia HTHP is overall better in terms of COP. For example: in the case of the production of hot sanitary water at 75 °C and at evaporation temperature of 20 °C (meaning that low temperature heat source would be available at temperatures greater than 25 °C) COPs would amount to 5.18 and 4.4 for the ammonia heat-pump and transcritical CO<sub>2</sub> heat-pump, respectively.

The differences between the COP values of both heat-pumps, Table 1, were the highest in the case of high evaporation temperature – in the range between 0.73 and 0.88 On the other hand, this difference was the lowest at low evaporation temperatures, ranging

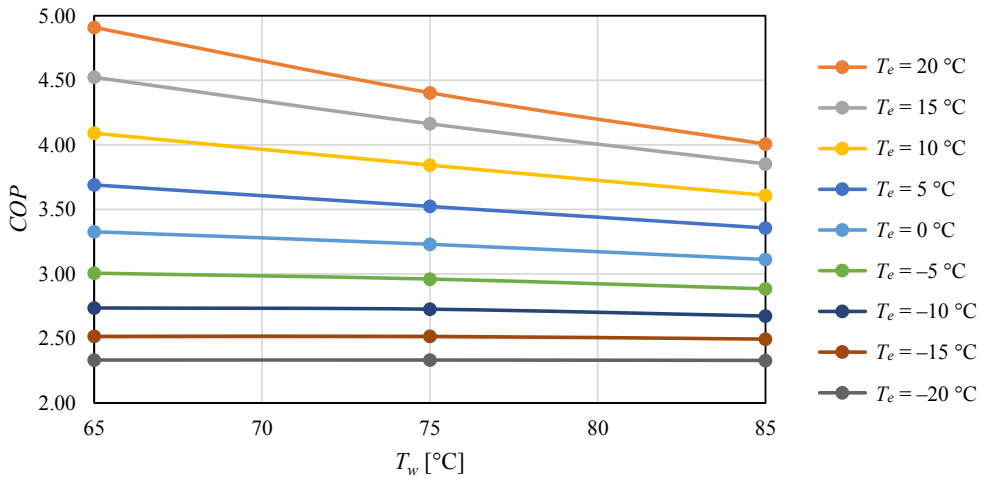


Fig. 6. COP dependent on the sanitary water temperature for the transcritical heat-pump (CO<sub>2</sub>)

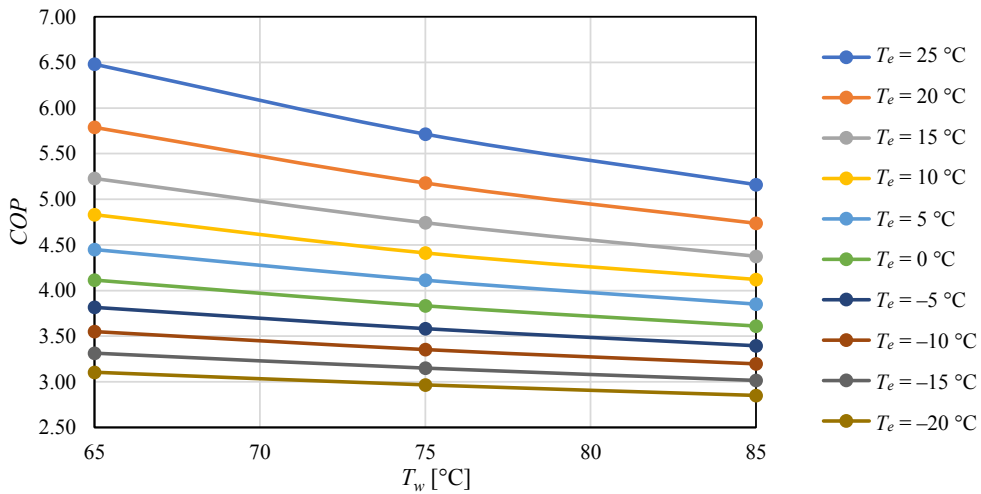


Fig. 7. COP dependent on the sanitary water temperature for the HTHP (NH<sub>3</sub>)

from 0.52 to 0.77. Outlet water temperatures have a similar influence on the difference between the COP values of both heat-pumps. The COP value was the highest in the case of low sanitary water temperatures (65 °C) ranging from 0.70 to 0.88, and the lowest at high sanitary water temperatures (85 °C) ranging from 0.5 to 0.73.

Table 1. Differences between COP values of both heat-pump technologies dependent on evaporation temperature and hot water temperature

		T <sub>e</sub> [°C]								
		20	15	10	5	0	-5	-10	-15	-20
T <sub>w</sub> [°C]	65	0.88	0.70	0.74	0.76	0.79	0.81	0.81	0.80	0.77
	75	0.77	0.58	0.57	0.59	0.60	0.62	0.63	0.63	0.63
	85	0.73	0.52	0.51	0.50	0.50	0.51	0.52	0.52	0.52

#### 4 CONCLUSIONS

Two different heat-pumps were presented and compared during this research work. The simulation models and assumptions were designed in a way to enable a fair comparison between these two technologies. The results of the simulations showed that ammonia outperforms carbon dioxide when used as a refrigerant for the production of hot sanitary water. Two main reasons why the ammonia HTHP outperforms the transcritical CO<sub>2</sub> heat-pump could be the following:

- a better isentropic efficiency of ammonia compressor,
- the fact that ammonia can transfer more heat per unit of mass or volume than CO<sub>2</sub>.

However, when deciding for the most profitable technology there are more factors to consider than just the COP. The investment costs of both technologies are one of the more important factors. It is expected that the cost for the transcritical CO<sub>2</sub> heat-pump would be higher than that of ammonia HTHP, due to higher pressures in the transcritical CO<sub>2</sub> heat-pump and an additional internal heat exchanger. On the other hand, double stage HTHP is needed in the case of low evaporation temperatures, which also increases the capital costs. Those heat-pump technologies can be used in the cases where cooling and heating is required at the same time. Food industry (for example meat and dairy industry) is especially suitable, because hot water and refrigeration are needed at the same time.

Further work should include a detailed designing and simulations of gas cooler, condenser, evaporators and internal heat exchanger including pressure drop analyses and optimisation of the operation of both heat-pumps. The comparison should also be extended to district heating applications, by using two stage transcritical heat-pumps if necessary. In this way, low temperature water sources could be exploited for district heating applications.

## 5 REFERENCES

- [1] Olabi, A. G. (2016). Energy quadrilemma and the future of renewable energy. *Energy*, vol. 108, p. 16, DOI:10.1016/j.energy.2016.07.145.
- [2] Kulcar, B., Goricanec, D., Krope, J. (2008). Economy of exploiting heat from low-temperature geothermal sources using a heat pump. *Energy and Buildings*, vol. 40, no. 3, p. 323-329, DOI:10.1016/j.enbuild.2007.02.033.
- [3] Goričanec, D., Pozeb, V., Tomšič, L., Trop, P. (2014). Exploitation of the waste-heat from hydro power plants. *Energy*, vol. 77, p. 220-225, DOI:10.1016/j.energy.2014.06.106.
- [4] Caf, A., Urbancl, D., Trop, P., Goricanec, D. (2016). Exploitation of low-temperature energy sources from cogeneration gas engines. *Energy*, vol. 108, p. 86-92, DOI:10.1016/j.energy.2015.09.119.
- [5] Zhao, Z., Xing, Z., Hou, F., Tian, Y., Jiang, S. (2016). Theoretical and experimental investigation of a novel high temperature heat pump system for recovering heat from refrigeration system. *Applied Thermal Engineering*, vol. 107, p. 758-767, DOI:10.1016/j.applthermaleng.2016.07.047.
- [6] Blarke, M. B. (2012). Towards an intermittency-friendly energy system: Comparing electric boilers and heat pumps in distributed cogeneration. *Applied Energy*, vol. 91, no. 1, p. 349-365, DOI:10.1016/j.apenergy.2011.09.038.
- [7] Bai, T., Yan, G., Yu, J. (2015). Thermodynamic analyses on an ejector enhanced CO<sub>2</sub> transcritical heat pump cycle with vapor-injection. *International Journal of Refrigeration*, vol. 58, p. 22-34, DOI:10.1016/j.ijrefrig.2015.04.010.
- [8] Zha, S., Hafner, A., Nekså, P. (2008). Investigation of R-744 Voorhees transcritical heat pump system. *International Journal of Refrigeration*, vol. 31, no. 1, p. 16-22, DOI:10.1016/j.ijrefrig.2007.06.017.
- [9] Li, X., Li, M., Ma, Y., Yan, Q. (2013). The influence of nitrogen on an expander in a carbon dioxide transcritical heat pump. *Applied Thermal Engineering*, vol. 59, no. 1-2, p. 182-188, DOI:10.1016/j.applthermaleng.2013.05.037.
- [10] Pearson, A. (2008). Refrigeration with ammonia. *International Journal of Refrigeration*, vol. 31, no. 4, p. 545-551, DOI:10.1016/j.ijrefrig.2007.11.011.
- [11] Sarkar, J., Bhattacharyya, S., Ram Gopal, M. (2007). Natural refrigerant-based subcritical and transcritical cycles for high temperature heating. *International Journal of Refrigeration*, vol. 30, no. 1, p. 3-10, DOI:10.1016/j.ijrefrig.2006.03.008.
- [12] Mayekawa Mycom, CO<sub>2</sub> Supercritical Heat pump from <http://www.mayekawa.com>, accessed on 2015-04-20.
- [13] Fouad, W.A., Vega, L. F. (2018). Transport properties of HFC and HFO based refrigerants using an excess entropy scaling approach. *The Journal of Supercritical Fluids*, vol. 131, pp. 106-116, DOI:10.1016/j.supflu.2017.09.006.
- [14] Aspen Technology, Inc, Aspen Plus V8.6. 2015.

# An Improved Bearing Fault Diagnosis Method using One-Dimensional CNN and LSTM

Honghu Pan – Xingxi He\* – Sai Tang – Fanming Meng

Chongqing University, The State Key Laboratory of Mechanical Transmissions, China

*As one of the most critical components in rotating machinery, bearing fault diagnosis has attracted many researchers' attention. The traditional methods for bearing fault diagnosis normally requires three steps, including data pre-processing, feature extraction and pattern classification, which require much expertise and experience. This paper takes advantage of deep learning algorithms and proposes an improved bearing fault diagnosis method based on a convolutional neural network (CNN) and a long-short-term memory (LSTM) recurrent neural network whose input is the raw sampling signal without any pre-processing or traditional feature extraction. The CNN is frequently used in image classification as it could extract features automatically from high-dimensional data, while LSTM is most applied in speech recognition as it considers time coherence. This paper combined one-dimensional CNN and LSTM into one unified structure by using the CNN's output as input to the LSTM to identify the bearing fault types. First, a part of raw bearing signal data is used as the training dataset in the model, and the simulation ends when the number of iterations reaches a specific value. Second, the rest of the signal data was input in the trained model as the testing dataset to verify the effectiveness of the proposed method. The results show that the average accuracy rate in the testing dataset of this proposed method reaches more than 99 %, which outperforms other algorithms for bearing fault diagnosis.*

**Keywords:** bearing fault diagnosis, CNN, LSTM

## Highlights

- An improved bearing fault diagnosis method based on deep learning algorithms is proposed in this paper.
- To take advantages of CNN and LSTM, this proposed model combined them into one structure by taking CNN's output as LSTM's input.
- This proposed model requires no traditional feature extraction, which is the most difficult step in traditional fault diagnosis methods.
- A comparison experiment with other deep learning-based models and traditional methods proved the effectiveness of this proposed method.

## 0 INTRODUCTION

The bearing is the most important component in rotating machinery; its main function is to support the mechanical rotating body and reduce the friction coefficient during movement. However, continuous abrasion resulting from the relative motion between mating surfaces would cause the components' damage, and several studies have shown that the bearing fault is the major source in rotating machinery faults [1]. An effective fault diagnosis method could obtain the healthy condition of bearings and probe the fault patterns, which are also the most challenging tasks in fault diagnosis.

The traditional methods for bearing fault diagnosis using vibration signals mainly includes three steps: data pre-processing, feature extraction, and pattern classification. The features that are commonly extracted have been generated from the time domain [2], the frequency domain [3], or the time-frequency domain [4]. Next, the extracted features are fed into classifiers such as a support vector machine (SVM) [5] and [6], a decision tree [7], a BP neural network [8], etc.

The difficulty of traditional fault diagnosis methods lies in the selection of features. Any feature has its own limitations [9], e.g., the time domain feature could not detect the faulty component, the frequency domain feature is unable to identify the location of damage, the envelop analysis requires prior knowledge and professional experience and the wavelet tree feature requires pre-selection of the suitable mother wavelet and appropriate level of decomposition.

In recent years, deep learning algorithms have aroused the widespread attention of researchers as it could discover intricate structures in big data [10]. Compared with traditional machine learning algorithms, deep learning has made great progress in image recognition [11] and speech recognition [12]. Furthermore, a large number of academic achievements emerged in the field of bearing fault diagnosis using deep learning algorithms. Sun et al. [13] extracted the wavelet features and selected convolutional neural network (CNN) as the classifier, whose accuracy rate reaches 99.79 %; He et al. [14] proposed an unsupervised fault diagnosis based on a deep belief network (DBN), and it has been proven

\*Corr. Author's Address: Chongqing University, The State Key Laboratory of Mechanical Transmissions, Chongqing 400044, China, xingxi@cqu.edu.cn

to outperform the back propagation neural network (BPNN) and support vector machine (SVM); Yin et al. [15] proposed an effective health assessment model by integrating Isomap into DBN with extracting time-domain, frequency-domain, wavelet packet features.

As illustrated in the literature [16], CNN is good at reducing frequency variations, and a long-short term memory (LSTM) recurrent neural network is appropriate for temporal modeling. This paper takes advantage of both CNN and LSTM and proposed an improved fault diagnosis method by combining a one-dimensional CNN and LSTM into one structure. By using this method, the limitations of traditional feature extraction can be avoided since the input of the model is the raw signal data and no traditional feature extraction is needed.

The rest of this paper is illustrated as follows: Section 1 introduces one-dimensional CNN and LSTM briefly and describes the method to combine them into one structure. Section 2 presents the bearing fault diagnosis and the results by using the proposed model. Section 3 shows the comparison results with other models. Section 4 draws the conclusion.

### 1 METHODS

The structure of the proposed method is shown in Fig. 1, which consists of five layers including the input layer, the convolutional layer, the pooling layer, the LSTM layer and the output layer.

Among above layers, the convolutional layer and pooling layer are applied in the CNN model, which has been proven effective in image recognition [11]. The convolution operation changes the input data into smaller feature maps through convolutional kernels. The convolutional kernels and feature maps are usually two-dimensional as the input of CNN are two-dimensional figures. To meet the one-dimensional -characteristic of mechanical signals, this paper constructs a one-dimensional convolutional neural network, whose convolutional kernels and feature maps are all one-dimensional.

Suppose the input of a one-dimensional convolutional neural network is  $x$ , which belongs to  $R^{n \times 1}$ , where  $n$  is the length of the input data.

Then the output of the convolutional layer can be calculated as follows [17]:

$$y_{i,j,k} = f\left(\sum_{i=1}^s x_{i,k} * w_{j,i} + b_i\right), \quad (1)$$

where the  $y_{i,j,k}$  is the output of the convolutional layer,  $1 \leq i \leq m$ ,  $m$  is the number of samples,  $1 \leq j \leq p$ ,  $p$  is the length of the convolutional kernels,  $1 \leq k \leq n$ ,  $f$  is the activation function, typically a hyperbolic tangent, relu, or sigmoid function;  $x_{i,k}$  is the input data;  $*$  is the convolution operation;  $w_{j,i}$  is the weight and  $b_i$  is the bias.

The pooling layer is the sub-sampling layer to reduce the size of feature maps and prevent the overfitting. The Max pooling method is frequently used in the pooling layer whose output is the

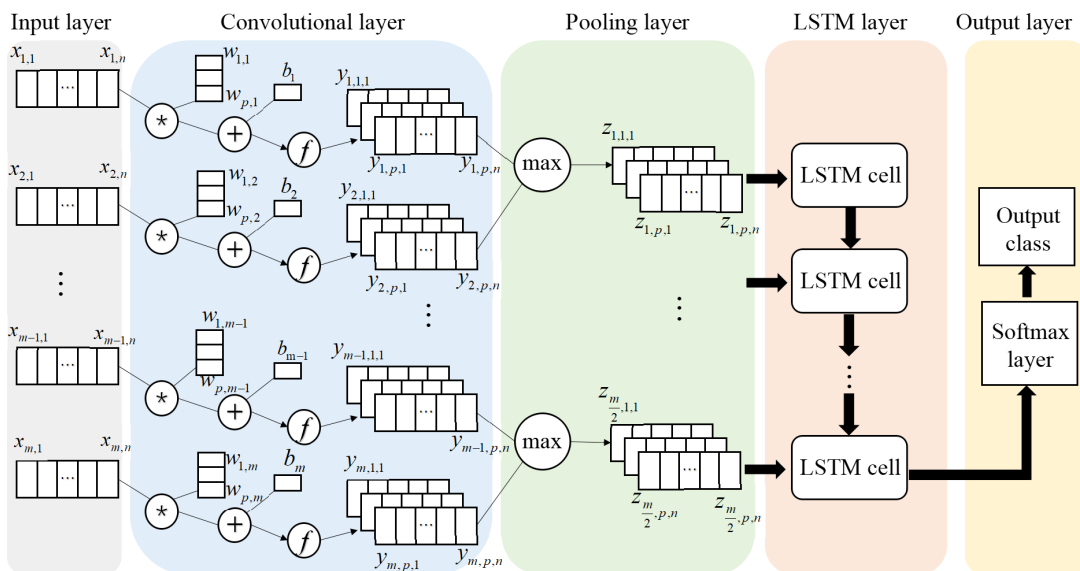


Fig. 1. Combined structure of one-dimensional CNN and LSTM

maximum of the previous feature maps, which can be expressed as follows [17]:

$$z_{l,j,k} = \max(x_{2i-1,j,k}, x_{2i,j,k}), \quad (2)$$

where  $z_{l,j,k}$  is the output of the pooling layer, and  $1 \leq l \leq m/2$ .

The output of the one-dimensional CNN is taken as the input of the LSTM to reduce variance in time series. In order to solve the problem of gradient disappearance and gradient explosion in standard recurrent neural networks (RNN), Hochreiter and Schmidhuber [18] proposed the LSTM. The main difference between the LSTM and standard RNN is that the hidden units' structure of the standard RNN was replaced by LSTM cells. As shown in Fig. 2, an LSTM's cell consists of three gate structures, i.e., the forget gate, input gate and output gate and a cell structure.

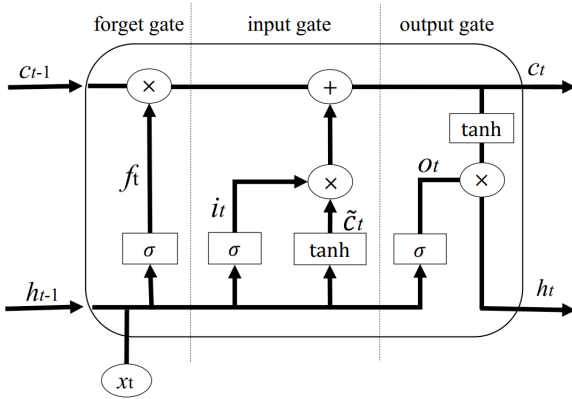


Fig. 2. Structure of a cell of LSTM

The output of the CNN layer is divided into  $m/2$  segments, which means the input of the LSTM layer has  $m/2$  time series.

The forget gate determines how much previous information could pass, whose output could be calculated as follows:

$$f_t = \sigma(w_{fz}z_t + w_{fh}h_{t-1} + b_f), \quad (3)$$

where the  $\sigma$  is a sigmoid function;  $w$  is weight;  $z_t$  is the current input,  $1 \leq t \leq m/2$ ;  $h_{t-1}$  is the output of the previous cell;  $b_f$  is the bias.

The input gate determines the new information that could be saved in the cell, which could be calculated as:

$$i_t = \sigma(w_{iz}z_t + w_{ih}h_{t-1} + b_i), \quad (4)$$

$$\tilde{C}_t = \tanh(w_{xz}z_t + w_{xc}h_{t-1} + b_i). \quad (5)$$

The output gate determines what information to output from the cell state, whose output can be expressed as follows:

$$c_t = c_{t-1}f_t + i_t\tilde{C}_t, \quad (6)$$

$$o_t = \sigma(w_{oz}z_t + w_{oh}h_{t-1} + b_o), \quad (7)$$

$$h_t = o_t \times \tanh(c_t). \quad (8)$$

Behind the LSTM layer is the softmax layer for classification, which could be calculated as follows:

$$\text{softmax}(y_i) = \frac{e^{u_i}}{\sum e^{u_i}}, \quad (9)$$

where  $u_i$  is the  $i^{\text{th}}$  output of the former layer.

The output class label can be obtained after the softmax layer, which was compared with the true label of the experimental data. The backpropagation (BP) algorithm [19] was introduced to train the model, which could adjust the weights and biases by comparing the output class label with the true label and propagating the output layer's error back through the network to minimize the loss function  $L$ , which is calculated as follows:

$$L = -\frac{1}{m} \sum [u \ln u' + (1-u) \ln (1-u')], \quad (10)$$

where  $m$  is the number of samples;  $u$  is the true label, and  $u'$  is the output class.

In the process of back propagation, the value of weight and bias are adjusted continuously until the number of iterations reaches the specific value. The parameters adjustment could be expressed as follows:

$$w_t = w_{t-1} - \varepsilon \frac{\partial L}{\partial w}, \quad (11)$$

$$b_t = b_{t-1} - \varepsilon \frac{\partial L}{\partial b}, \quad (12)$$

where  $\varepsilon$  is the learning rate, which determines the updating speed of parameters;  $w_t$ ,  $b_t$  represent the value of weight and bias in  $t^{\text{th}}$  iteration;  $w_{t-1}$ ,  $b_{t-1}$  represent the value of weight and bias in  $(t-1)^{\text{th}}$  iteration.

The training processing was presented in Fig. 3, the output class was compared with the true label of the sample, and parameters were adjusted based on the above BP algorithm. After several iterations, the value of loss function became tiny, which means the parameters have met the samples' characteristics.

To accelerate the training process and prevent the local optima, the mini-batch gradient descent algorithm [12] is applied, in which the batch size of training samples is selected for iteration.

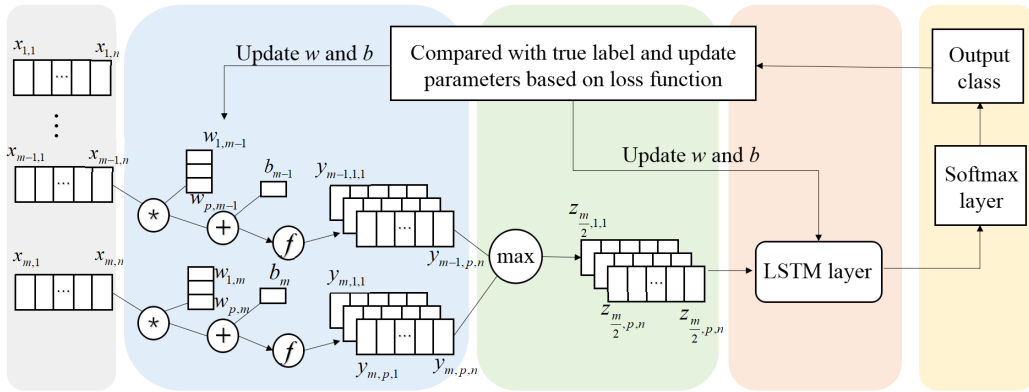


Fig. 3. The training processing

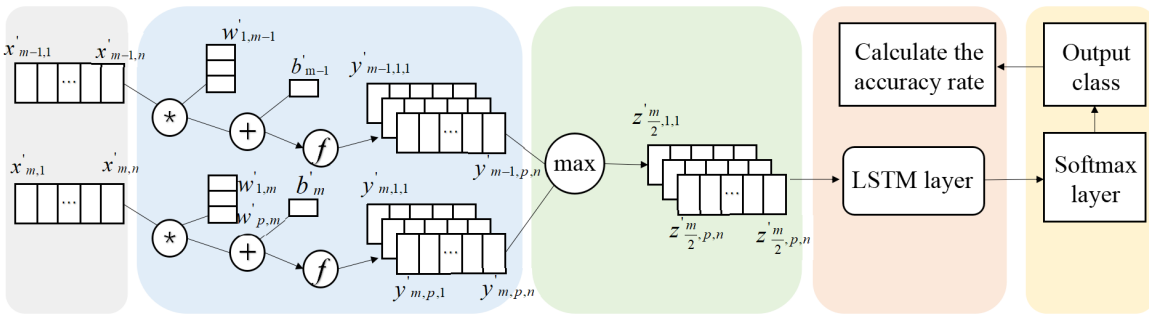


Fig. 4. The testing processing

After training processing finished, testing datasets is about to be input into the trained model, which was presented in Fig. 4. Parameters for testing datasets use what was updated in the last iteration of training processing.

To validate the algorithm's efficiency, the accuracy rate  $A_r$  was introduced, which could be calculated with the following formula:

$$A_r = \frac{N_r}{N_t} \times 100 [\%], \quad (13)$$

where  $N_r$  is the number of correctly predicted samples, and  $N_t$  is the number of total samples.

The flow chart of this whole proposed model is shown in Fig. 5, where  $N$  is the max iteration epoch. Firstly, vibration signal was collected in test stand and then divided into a training dataset and a testing dataset; Secondly, the training dataset was used to train the model, and optimal parameters would be acquired after several iterations; Thirdly, the testing dataset was input to the trained model to obtain its predicted class, so the accuracy rate could be calculated based on Eq. (13).

## 2 BEARING FAULT DIAGNOSIS

### 2.1 Experimental Setup and Data Acquisition

In order to validate the proposed method, the bearing vibration data from the Case Western Reserve University (CWRU) Bearing Data Centre is applied [20]. As shown in Fig. 6, the test stand consists of a motor, a torque transducer, a dynamometer and the control electronics (not shown). The SKF bearings were used in this experiment, whose fault was introduced by electro-discharge machining. The vibration data was collected for four health conditions, i.e., the normal condition, the ball fault, the inner race fault and the outer race fault, and the fault diameters are 0.18 mm, 0.36 mm, and 0.53 mm, respectively.

The data used in this paper were collected from the drive end of the test bench. The motor provides an output power of 2.2 kW, the sampling frequency is 48 kHz and the sampling time for each dataset is approximately 10 s. The rotating speed of the shaft is 1725 r/min, which means about 1670 data points will be collected for one revolution. The first 48,430 points of each dataset are chosen and divided into 290 samples, and therefore each sample includes

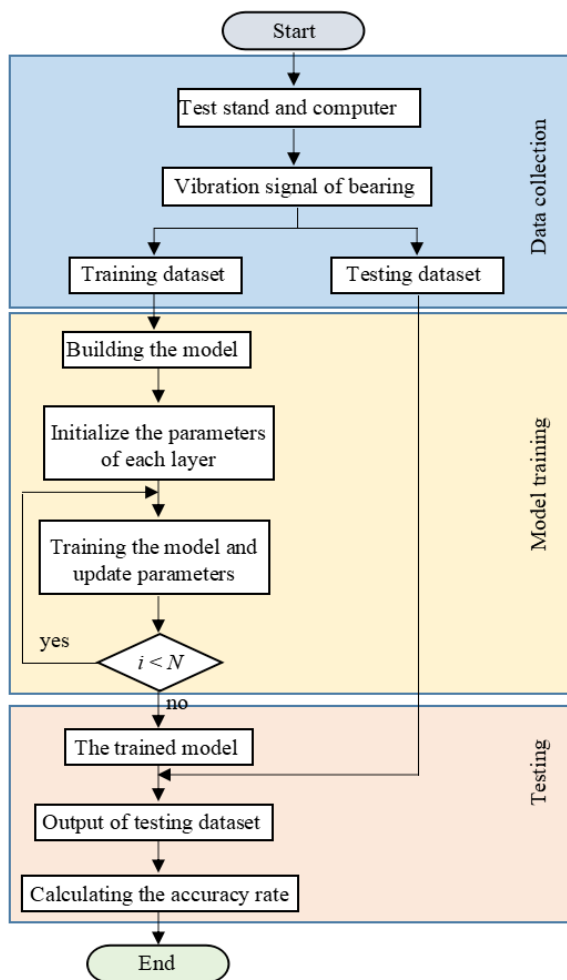


Fig. 5. Flowchart of the proposed model

1670 points collected in one revolution. To reduce the impact of equipment fluctuations and to ensure the points in each sample are collected within the same revolution, the first 35 points and the last 35 points in each sample are discarded; therefore, every sample includes only 1600 points.

Each dataset represents a state of bearing health conditions and contains 290 samples, in which 240 samples are selected randomly as the training dataset, and the rest are used as the test set. As shown in Table 1, the proposed model processed a total of ten datasets, including one normal state and three fault types, i.e. the ball fault, the inner race fault and the outer race fault while each fault type has three variations by size. Fig. 7 shows the vibration signals of ten health conditions as referred in the Table 1, and it is hard to classify them just by intuition.

Table 1. Description of dataset

Health condition	Fault size [mm]	Training dataset	Testing dataset	Class label
a) normal	–	240	50	0
b) ball fault	0.18	240	50	1
c) ball fault	0.36	240	50	2
d) ball fault	0.53	240	50	3
e) inner race fault	0.18	240	50	4
f) inner race fault	0.36	240	50	5
g) inner race fault	0.53	240	50	6
h) outer race fault	0.18	240	50	7
i) outer race fault	0.36	240	50	8
j) outer race fault	0.53	240	50	9

## 2.2 Training Results

The model was illustrated in Section 2 in detail. The input data has three dimensions; the first dimension is the number of samples; the second dimension represents time steps, and the third dimension is a default value. The original training dataset with the dimension of  $2400 \times 1600$  is changed into  $2400 \times 80 \times 20$ , while for the testing dataset the dimension is changed to  $500 \times 80 \times 20$ .

The structure of this proposed model was shown in Fig. 1. A convolutional layer is set behind the input layer, whose kernel length is chosen to be 32 and kernel channel to be 64, then the dimension of this layer’s output is  $2400 \times 80 \times 32$  or  $500 \times 80 \times 32$ . Behind the convolutional layer is the pooling layer, the pooling length and stride are both chosen to be 2, which means the dimension of this layer’s output is  $2400 \times 40 \times 32$  or  $500 \times 40 \times 32$ . Following the pooling layer, a ‘relu’ activation function is introduced to increase the nonlinear properties, and 0.2 dropout is introduced to prevent overfitting. The fourth layer is the LSTM layer with 128 cells, whose output dimension is  $2400 \times 128$  or  $500 \times 128$ . The last layer is the output layer with a softmax classifier, and the data turns into  $2400 \times 10$  or  $500 \times 10$ .

Settings of the model were shown in Table 2., and the Adam optimizer [21] is chosen to minimize the loss function. This proposed model is developed based on Python and implemented in an open resource library (keras). All experiments are performed on a computer with 4 GB GPU whose type is GTX 1050 Ti.

One important task for deep learning models is the adjustment of hyperparameters, and this paper takes the batch size and learning rate as hyperparameters. As mentioned in Section 1, the mini-batch gradient descent algorithm was used to minimize the loss function, and then the batch size defines the number

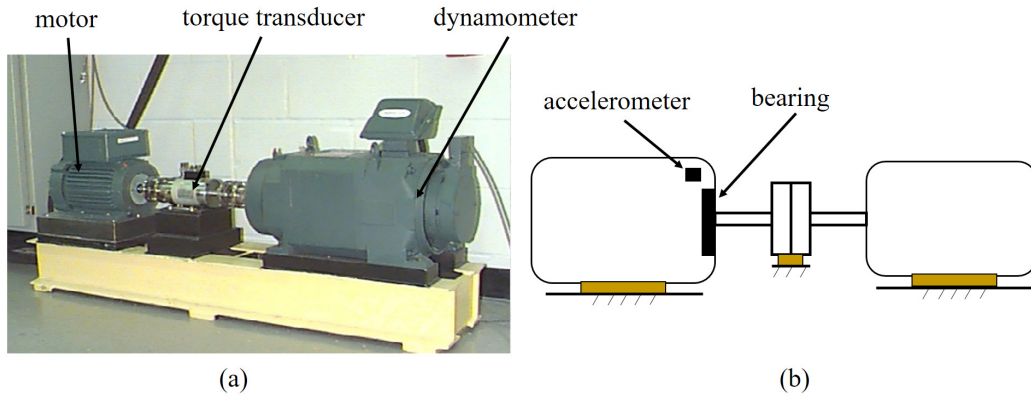


Fig. 6. Test stand; a) a photo, and b) a scheme

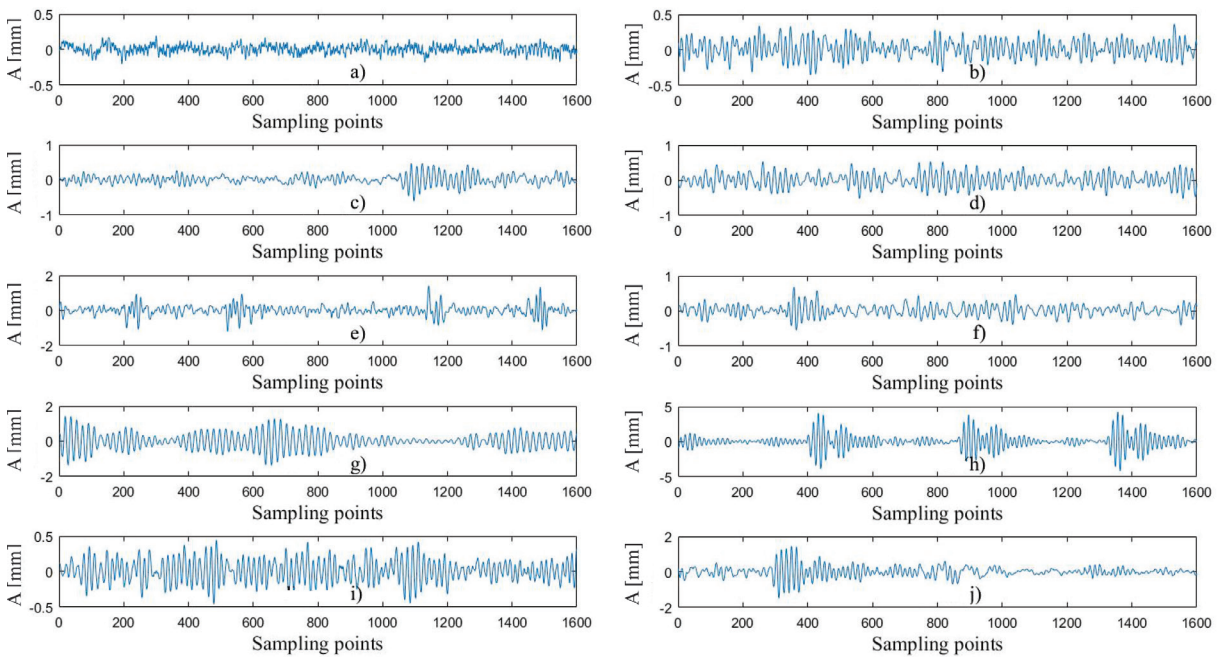


Fig. 7. Vibration signal for different health conditions (as referred in Table 1) the y-axis represents the amplitude of signal and x-axis is the number of sampling points

Table 2. Parameters for the proposed method

Layer	Type	Parameter for layer	Other parameters
1	Input layer	Shape = [2400,80,20]	Epoch = 50
2	Convolutional layer	KC = 32, KL = 64	Dropout = 0.2 Activation = 'relu'
3	Pooling layer	PL = 2, Stride = 2	Classifier = 'softmax'
4	LSTM layer	NU = 128	Optimizer = 'AdamOptimizer'
5	Output layer	OC = 10	

KC = kernal channel; KL = kernal length; PL = pooling length; NU = number of units; OC = output channel

Table 3. Accuracy rate in testing dataset for different configurations

Learning rate	Batch size					
		20	40	60	80	100
		Accuracy rate [%]				
0.0005	99.8	99.6	99.2	99.8	99.6	
0.001	99.4	99.8	99.8	99.4	99	
0.002	99.8	99.8	99.4	99	99.6	
0.004	99.6	99.6	98.6	100	99.6	
0.006	98.8	98.4	97.6	98.8	99.6	

of samples to be processed in one batch. The learning rate defines the updating speed of some parameters such as weight and bias.

The accuracy rate in the testing dataset reflects the effectiveness of the model, which equals the number of correctly predicted samples divided by the total number of testing dataset samples. The results for different configurations are shown in Table 3; as can be seen, the best configuration with the batch size of 80 and the learning rate of 0.004 presents a completely correct prediction. Otherwise, the average accuracy rate is over 99 %, which proves the effectiveness of the proposed model.

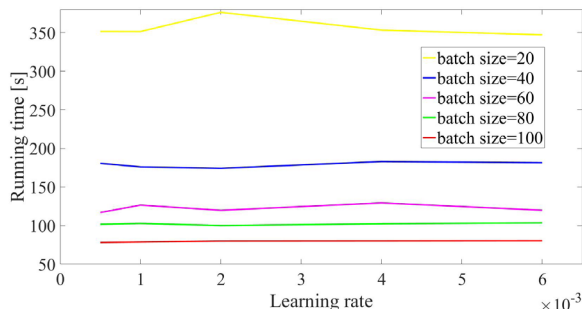


Fig. 8. Running time for different configurations

As shown in Table 3, the value of batch size has little effect on the prediction accuracy, while a large learning rate may lead to a decline in prediction accuracy because the parameters tend to oscillate instead of converge. Considering the similar accuracy rate for different configurations, the computing time is introduced for evaluation. As shown in Fig. 8, the main influencing factor of computing time is the batch size. The computing time for the batch size of 20 is four times more than that for the batch size of 100. Taking accuracy rate and computing time into consideration, the configuration with the batch size of 80 and the learning rate of 0.004 is recommended.

### 3 COMPARISONS

#### 3.1 Comparison with Other Deep Learning Models

The comparisons between the proposed method and a DNN model, a CNN model and a LSTM model are presented in this section. The DNN model includes three layers with 256 neurons, 256 neurons, 10 neurons respectively and 0.2 dropout to prevent overfitting; otherwise, the ‘relu’ activation function is used to introduce non-linear properties. The configuration and parameters for the CNN model and the LSTM in this section use the same values in Table 2.

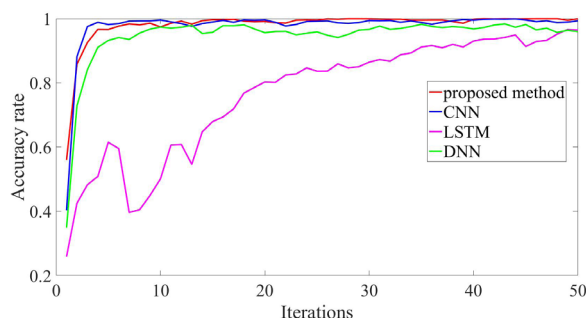


Fig. 9. Accuracy rate in training dataset of models using deep learning algorithms

The accuracy rate in the training dataset is used to evaluate the models; as shown in Fig. 9, the iteration speed of the LSTM model is the slowest, which requires nearly 50 iterations to achieve a 90 % accuracy rate. The CNN model performs as good as the proposed method in training dataset and better than the DNN.

Table 4 presents the accuracy rate in the testing dataset for different models, the three models for comparison achieve the accuracy rate of 98.8 %, 93.8 % and 80.8 %, respectively. Combined with Fig. 8 and Table 4, the accuracy rate of the DNN model in the testing dataset is much lower than that in training dataset due to the overfitting.

Table 4. Accuracy rate in testing dataset of different models

Methods	Proposed method	CNN	LSTM	DNN
Accuracy rate [%]	100	98.8	93.8	80.8

The conclusion can be drawn that the proposed model has a higher accuracy rate in the testing dataset than the CNN model, it iterates faster than LSTM model, and it is more effective in reducing overfitting than DNN model.

#### 3.2 Comparison with Traditional Fault Diagnosis Methods

The traditional fault diagnosis methods require feature extraction before feeding data to the classifier. This paper extracted the time domain features, wavelet packet features and empirical mode decomposition (EMD) features to feed into a commonly used classifier decision tree. Table 5 presents the extracted time domain features, while wavelet packet features and EMD features are given in [22] and [23] respectively. The training and testing datasets use what mentioned in 2.1 (240 datasets for training, 50 datasets for testing).

**Table 5.** Time domain features

Features	Formula
Mean	$\bar{X} = \frac{1}{N} \sum_{i=1}^N x_i$
Root mean square	$X_{rms} = \sqrt{\frac{1}{N} \sum_{i=1}^N x_i^2}$
Variance	$D_x = \frac{1}{N-1} \sum_{i=1}^N (x_i - \bar{X})^2$
Peak value	$x_p = \max(x_i)$
Peak to peak value	$X_{p-p} = \max(x_i) - \min(x_i)$
Kurtosis	$D_x = \frac{\frac{1}{N} \sum_{i=0}^N (x_i - \bar{X})^4}{\left[ \frac{1}{N} \sum_{i=0}^N (x_i - \bar{X})^2 \right]^2}$
Skewness	$S = \frac{1}{N} \sum_{i=1}^N \left( \frac{x_i - \bar{X}}{\sigma_x} \right)^3$
Crest factor	$C_f = \frac{X_p}{X_{rms}}$
Impulse factor	$I_f = \frac{X_p}{\bar{X}}$

The performance of models using different features is given in Table 6; the accuracy rate is in the range between 75 % and 90 % by using traditional methods. It can be concluded that the training results by using different features vary greatly and the accuracy rate of the previous experiment is nearly 10 % higher than the latter one, which proves the choice of the feature is a difficult step in traditional methods. The same feature extracted in different ways may cause different results as well. The wavelet packet feature of db4 mother wavelet outperforms than that of db3 mother wavelet and haar mother wavelet. Therefore, the overall performance of the traditional methods is worse than the deep learning-based models.

Compared with traditional or previously-used techniques of bearing fault diagnosis, the advantages of using the deep learning networks mentioned in the paper lie in the following aspects: 1) Comparably fewer iterations are required, and the computing time is acceptable. Based on Fig. 8, with the batch size of 80, the simulation time takes only 100 seconds.

2) Even though the rate of accuracy is not exactly 100 %, the result is remarkably high and quite close to 100 % (with the batch size of 80, different learning rates result in the accuracy rate all above 99.4 %). 3) No feature extraction based on prior knowledge, diagnostic experiences or professional expertise is required, and the constructed deep learning networks can extract features automatically. Traditional feature extraction methods can be quite complicated, e.g., different features suit for different signals, for instance, Fourier transform suits stationary signals while wavelet transform suits non-stationary signals. Or those methods might be hard to fully reflect the fault characteristics. Automatic feature extraction can avoid these complexities and uncertainties.

#### 4 CONCLUSIONS

In traditional methods for bearing fault diagnosis and detection, it's necessary to extract some features to describe the signal. However, different features suit different conditions, which requires much expertise and a priori knowledge. The application of deep learning algorithms helps solve the problem as the deep learning algorithms such as the DNN, CNN, and LSTM have been proved capable of discovering intricate structures in big data.

**Table 6.** Performance of different methods

Methods	Accuracy rate in testing dataset [%]
Time domain + decision tree	80.6
EMD + decision tree	77
Wavelet packet(mother wavelet: haar) + decision tree	79.8
Wavelet packet(mother wavelet: db3) + decision tree	86.6
Wavelet packet(mother wavelet: db4) + decision tree	87.8

This paper proposed an improved bearing fault diagnosis method by combining one-dimensional CNN and LSTM into one structure. Considering CNN's advantage in reducing frequency variance and LSTM's advantage in the temporal model, the output of CNN was taken as the input of LSTM. The raw signal data collected by sensors is divided into a training dataset and testing dataset. The training dataset was used to determine the inner parameters in the model. After that, the testing dataset was fed into the trained model to verify its effectiveness. The results show that the average accuracy rate in the testing dataset is over 99 %; moreover, the model in

its best configuration presents a completely correct prediction.

Compared with other deep learning-based models, the proposed model has advantages: firstly, it achieves the highest prediction accuracy in the testing dataset; secondly, it iterates faster than the LSTM model; thirdly, the proposed model is more efficient to prevent overfitting than the DNN model. Compared with the traditional fault diagnosis methods, this proposed method has the following advantages: firstly, the traditional feature extraction is not required, which eliminates the interference of inappropriate features; secondly, the prediction accuracy of this proposed method is much higher than that of the traditional methods.

However, this proposed model has its own limitation: its main disadvantage is the large amount of computation required. As the improvement of computer's computation power, this proposed method can be extended to more complicated mechanical systems, such as gearboxes. Future research will focus on the further improvement of the algorithm and its applications in other field.

## 5 ACKNOWLEDGEMENTS

This work was supported by the Fundamental Research Funds for the Central Universities of P.R. China (No. 106112016CDJZR288805).

## 6 REFERENCES

- [1] Vekteris, V., Trumpa, A., Turla, V., Šešok, N., Iljin, I. Moškin, V., Kilikevičius, A., Jakštis, A., Kleiza, J. (2017). An investigation into fault diagnosis in a rotor-bearing system with dampers used in centrifugal milk separators. *Transactions of FAMENA*, vol. 41, no. 2, p. 77-86, DOI:10.21278/TOF.41207.
- [2] Liu, F., Qian, Q., Liu, F., Lu, S., He, Q., Zhao, J. (2017). Wayside bearing fault diagnosis based on envelope analysis paved with time-domain interpolation resampling and weighted-correlation-coefficient-guided stochastic resonance. *Shock and Vibration*, vol. 2017, art ID 3189135, DOI:10.1155/2017/3189135.
- [3] Mckee, K.K., Forbes, G.L., Mazhar, I., Entwistle, R., Hodkiewicz, M., Howard, I. (2015). A vibration cavitation sensitivity parameter based on spectral and statistical methods. *Expert Systems with Applications*, vol. 42, no. 1, p. 67-78, DOI:10.1016/j.eswa.2014.07.029.
- [4] Do, V.T., Nguyen, L. C. (2016). Adaptive empirical mode decomposition for bearing fault detection. *Strojniški vestnik - Journal of Mechanical Engineering*, vol. 62, no. 5, p. 281, 290, DOI:10.5545/sv-jme.2015.3079.
- [5] Fernández-Francos, D., Martínez-Rego, D., Fontenla-Romero, O., Alonso-Betanzos, A. (2013). Automatic bearing fault diagnosis based on one-class v-SVM. *Computers & Industrial Engineering*, vol. 64 no. 1, p. 357-365, DOI:10.1016/j.cie.2012.10.013.
- [6] Zhang, X., Liang, Y., Zhou, J., Zang, Y. (2015). A novel bearing fault diagnosis model integrated permutation entropy, ensemble empirical mode decomposition and optimized SVM. *Measurement*, vol. 69, p. 164-179, DOI:10.1016/j.measurement.2015.03.017.
- [7] Aydin, I., Karakose, M., Akin, E. (2014). An approach for automated fault diagnosis based on a fuzzy decision tree and boundary analysis of a reconstructed phase space. *ISA Transactions*, vol. 53, no. 2, p. 220-229, DOI:10.1016/j.isatra.2013.11.004.
- [8] Zhao, Z., Xu, Q., Jia, M. (2016). Improved shuffled frog leaping algorithm-based BP neural network and its application in bearing early fault diagnosis. *Neural Computing and Applications*, vol. 27, no. 2, p. 375-385, DOI:10.1007/s00521-015-1850-y.
- [9] Boudiaf, A., Moussaoui, A., Dahane, A., Atoui, I. (2016). A comparative study of various methods of bearing faults diagnosis using the case Western Reserve University data. *Journal of Failure Analysis and Prevention*, vol. 16, no. 2, p. 271-284, DOI:10.1007/s11668-016-0080-7.
- [10] Lecun, Y., Bengio, Y., Hinton, G. (2015). Deep learning. *Nature*, vol. 521, no. 7553, p. 436-444, DOI:10.1038/nature14539.
- [11] He, K., Zhang, X., Ren, S., Sun, J. (2016). Deep residual learning for image recognition. *Proceedings of the IEEE Conference on Computer Vision and Pattern Recognition*, DOI:10.1109/cvpr.2016.90.
- [12] Hinton, G., Deng, L., Yu, D., Dahl, G.E., Mohamed, A., Jaitly, N., Senior, A., Vanhoucke, V. (2012). Deep neural networks for acoustic modeling in speech recognition: the shared views of four research groups. *IEEE Signal Processing Magazine*, vol. 29, no. 6, p. 82-97, DOI:10.1109/msp.2012.2205597.
- [13] Sun, W., Yao, B., Zeng, N., Chen, B., He, Y., Cao, X., He, W. (2017). An intelligent gear fault diagnosis methodology using a complex wavelet enhanced convolutional neural network. *Materials*, vol. 10, no. 7, p. 790, DOI:10.3390/ma10070790.
- [14] He, J., Yang, S., Gan, C. (2017). Unsupervised fault diagnosis of a gear transmission chain using a deep belief network. *Sensors*, vol. 17, no. 7, p. 1564, DOI:10.3390/s17071564.
- [15] Yin, A., Lu, J., Dai, Z., Li, J., Ouyang, Q. (2016). Isomap and deep belief network-based machine health combined assessment model. *Strojniški vestnik - Journal of Mechanical Engineering*, vol. 62, no. 12, p. 740-750, DOI:10.5545/sv-jme.2016.3694.
- [16] Sainath, T.N., Vinyals, O., Senior, A., Sak, H. (2015). Convolutional, long short-term memory, fully connected deep neural networks. *IEEE International Conference on Acoustics, Speech and Signal Processing*, p. 4580-4584, DOI:10.1109/icassp.2015.7178838.
- [17] Li, H., Lin, Z., Shen, X., Brandt, J., Hua, G. (2015). A convolutional neural network cascade for face detection. *IEEE Conference on Computer Vision and Pattern Recognition*, DOI:10.1109/cvpr.2015.7299170.
- [18] Hochreiter, S., Schmidhuber, J. (1997). Long short-term memory. *Neural Computation*, vol. 9, no. 8, p. 1735-1780, DOI:10.1162/neco.1997.9.8.1735.
- [19] Horikawa, S., Furuhashi, T., Uchikawa, Y. (1992). On fuzzy modeling using fuzzy neural networks with the back-

- propagation algorithm. *IEEE Transactions on Neural Networks*, vol. 3, no. 5, p. 801-806, DOI:10.1109/72.159069.
- [20] Loparo, K. (1998). Bearings Vibration Data Set, Cast Western Reverse University, from: <https://csegroups.case.edu/bearingdatacenter/home>, accessed on 1998-July-25
- [21] Kingma, D., Ba, J. (2015). Adam: A method for stochastic optimization. *Internal Conference of Learning Representation*, p. 1-15.
- [22] Wang, Z., Zhang, Q., Xiong, J., Xiao, M., Sun, G., He, J. (2017). Fault diagnosis of a rolling bearing using wavelet packet denoising and random forests. *IEEE Sensors Journal*, vol. 17, no. 17, p. 5581-5588, DOI:10.1109/jсен.2017.2726011.
- [23] Ali, J.B., Fnaiech, N., Saidi, L., Chebel-Morello, B., Fnaiech, F. (2015). Application of empirical mode decomposition and artificial neural network for automatic bearing fault diagnosis based on vibration signals. *Applied Acoustics*, vol. 89, p. 16-27, DOI:10.1016/j.apacoust.2014.08.016.

# The Influence of External Conditions on the Mechanical Properties of Resin-bonded Grinding Wheels

Albin Matavz<sup>1</sup> – József Mursics<sup>2</sup> – Ivan Anzel<sup>3,\*</sup> – Tina Zagar<sup>4</sup>

<sup>1</sup>MAMUT TIM, Ltd., Slovenia

<sup>2</sup>FALCO Zrt. Hungary

<sup>3</sup>University of Maribor, Faculty of Mechanical Engineering, Slovenia

<sup>4</sup>Ministry of Economic Development and Technology, Slovenia

*The paper presents the ageing effects on mechanical and functional properties of resin-bonded grinding wheels with Aluminium oxide and Silicon carbide. The measurements provided the basis for the design of a temporary model of changes. Furthermore, the influence of humidity as the most likely cause for a steep downgrade in the mechanical properties of grinding wheels was examined and identified. Within that context, the system of forced, i.e. accelerated ageing of grinding wheels (additional humidification) was used under special atmospheric conditions.*

*The model mechanisms for changing microstructures during ageing are presented and are based on the microstructural characterisation of grinding wheels that were exposed to different thermo-mechanical impacts. These mechanisms confirm the most likely cause for ageing, as established empirically, and therewith related changes of the mechanical properties of grinding wheels. Furthermore, the findings are useful in the process of manufacturing grinding wheels, helping to improve mechanical properties and most of all, considerably slowing down the ageing process, and providing higher added value to such products.*

**Keywords:** resin-bonded grinding wheels, mechanical properties, ageing, microscopic analysis

## Highlights

- Mechanisms for changing microstructures during ageing of grinding wheels are presented.
- The suggested process of manufacturing of grinding wheels, with the aim of helping to improve mechanical properties.
- Influence of humidity downgrades the mechanical properties of grinding wheels.
- Slowing down the ageing process provides a higher added value to such products.

## 0 INTRODUCTION

When we check the quality of grinding or cutting abilities of grinding wheels with corundum or SiC grains, it can be seen that their quality tends to alter over time. This time-dependent ageing processes or changes of mechanical properties occur gradually over the period of two or three months from the date of production, especially because of atmospheric conditions (humidity), affecting the microstructure of grinding wheels and their alterations during grinding.

When we searched for causes of the change of mechanical properties of resin-bonded grinding wheels during a specific period, we have not been able to find any scientific article or source in the database dealing with the issue. Different producers or researchers connected with them have dealt with a similar issue, but due to confidentiality of data and findings (significantly unfavourable technological information for grinding wheels producers with respect to uncontrolled fall of quality of grinding wheels), their findings are not accessible to a wider circle of users, or the technological information are owned by the producers.

It should however be mentioned that many authors have dealt with the issue of the change in mechanical properties of certain other types of grinding wheels (e.g. metal – bonded Cubic Boron Nitride (CBN) and diamond grinding wheels) [1] to [6], and have shed light on processes during grinding, depending on the type of binder, the shape and type of grains, and the changes of their micro and macro structures during the process of their use. Some of the findings from researches may be connected to such recognitions and findings. The wear behaviour of abrasive tools can greatly affect the machined surface quality and integrity, which is the reason why different wear status of the abrasive tools could produce different material removal behaviour during grinding. Generally, the classification of wear behaviour in grinding includes the wear of abrasive tools and the wear of abrasive grains. In recent years, more attention has been paid to the research on wear behaviour of abrasive tools from the macro and micro perspective [1] and [2].

At the same time, a lot of investigations on the influence of the porosity on the mechanical strength of the porous composite matrices of grinding wheels were made [3].

\*Corr. Author's Address: University of Maribor, Faculty of Mechanical Engineering, Smetanova ulica 17, 2000 Maribor, Slovenia, ivan.anzel@um.si

Newest literature also mentioned numerical simulation and experimental studies on the mechanism of grain fracture based on the analysis of brazing-induced residual stress and the resultant stress in grinding; as such, the grain fracture wear could be predicted and controlled effectively [4].

On the basis of scientific and research methods it has been established how the ageing affects the mechanical properties of grinding wheels and how downgrade in the functional properties can be prevented by appropriate production procedures.

With this objective, the following activities have been carried out:

- test samples of resin-bonded grinding wheels were made within the series production of grinding wheels under realistic production and technological conditions and parameters, applied in the industry;
- the influence of humidity on mechanical properties of grinding wheels has been determined;
- the research of what causes the downgrade in the cutting abilities of a grinding wheel (hygroscopic moisture from the atmosphere, pores and cracks in grinding wheels);
- analysis of how moisture content in resin-bonded grinding wheels affects the downgrade in the quality and the related ageing process of grinding wheels;
- the weighting factor determined by tests was eliminated, as it causes ageing of resin-bonded grinding wheels and reduction of cutting abilities;
- cutting ability factor values of grinding wheels were identified over a time-defined ageing process;
- influence of ageing was determined on the rotational speed in disintegration of grinding wheels during ageing;
- the findings were confirmed by the microstructural analysis of samples and the created model of the course of ageing in polymeric matrix of grinding wheel.
- On the basis of the results, the course or intensity of the influence of ageing on the properties of resin-bonded grinding wheels was determined, and the obtained data and findings enabled an improvement in production procedures or defining the method of quality control in the production of resin-bonded grinding wheels.

## 1 THEORETICAL BACKGROUND

### 1.1 Grinding Products

Grinding products may be used for cutting or grinding metals, as well as organic and inorganic materials. There are conventional (classic), flexible grinding wheels (emery cloth and paper) and super abrasive wheels (CBN and Diamond wheels) [5] and [6]. Their properties and efficiency depend on the microstructure and components they are made of, the mechanical properties or the loads they can bear, circumferential speed of the grinding wheel, and the heat generated during use [7].

Conventional grinding wheels are made of grain aggregates, fillers (additives) and binders (phenol-formaldehyde resins), which provide the grinding wheel with strength and uniform design.

In order to create a strong and stable bond between grains and the bearing material, we need a high quality phenol-formaldehyde resin and the correct ratio between liquid (resole) and powdered (novolak) resin. The composition of the polymer matrix of a resin-bonded grinding wheel must be such that the operating temperature ranging between 700°C and 1000°C generated during grinding doesn't significantly alter the mechanical properties.

The key properties of phenol-formaldehyde resins are their ability to crosslink and form infinite polymer chains and their irreversible thermal strengthening in the thermal process phase of grinding wheel production.

Phenol-formaldehyde resins are obtained by reaction of phenol (P) and formaldehyde (F) in the presence of a catalyst, which may be acid, base or metal salt. The result is a liquid or hard dispersed product, which may be thermo-plastic (novolak) or duro-plastic (resole) [8].

Fig. 1 shows the molecular structure of phenol-formaldehyde resins with regard to the F/P molar ratio and pH.

P and F are the most important raw materials for industrial production of phenol resins.

The key factors, which affect what type of resin is obtained, are:

- molar ratio between F and P;
- type of catalyst, which is used in polymerization.

When a catalyst is alkaline, we obtain resoles (liquid resins) with the addition of formaldehyde and phenol and the formation of oligomers, with a molar ratio of F to P  $\geq 1$ , which is the most frequently used binder on water basis for grain wetting in the grinding industry [9].

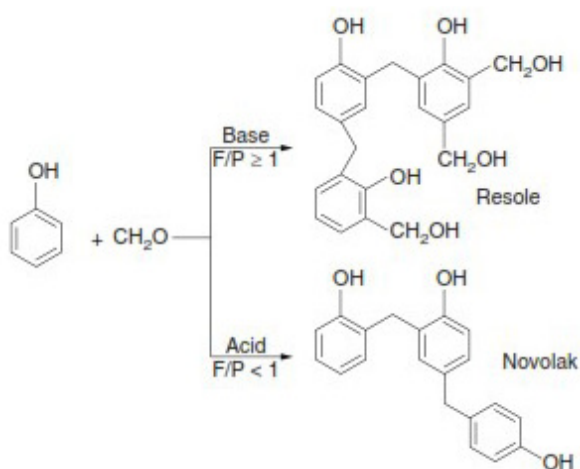


Fig. 1. Molecular structure phenol-formaldehyde resin

However, if an acidic catalyst is used, novolak (powdered resins) is obtained by the addition of formaldehyde and phenol and the formation of oligomers in an acidic environment, with a molar ratio of F to P < 1, which is useful for impregnation of meshes. In addition, together with hexamethylenetetramine (HMTA or Hexa) it is also useful in the grinding industry.

## 1.2 Abrasive Grains

Grains are made of inorganic materials and are distinguished by high strength and appropriate toughness. The basic function of grains is grinding of processed material (workpiece) [10].

Grains are most often composed of Aluminium oxide ( $\text{Al}_2\text{O}_3$ ) and Silicon carbide (SiC), which are produced synthetically.

Grains with high hardness are usually fragile, so such grains are used for fine and end grinding [11]. A type of phenol resin is used as a binder, since it is more flexible, whereas resistance to higher temperatures is not that important. Quite the opposite, grains with lower hardness usually possess a higher degree of toughness, and are less fragile, so they are used for intensive, rough grinding. Because high quantities of heat are released during such grinding, phenol resins must be used as a binder, since they are more resistant to high temperatures and serve as a strong binder of abrasive grain particles [12] and [13].

The choice in the size of grains is also important and depends on the processed material and grinding conditions. The surface roughness of the processed material directly depends from size of abrasive grains [14]. As a rule, larger grains are used for rougher

materials, and smaller grains are used for less rough materials.

## 1.3 Fillers

Fillers have been used in the production of grinding wheels from the very beginning. The use of fillers delivered the findings that various fillers, which are usually inorganic, in powdered or fibre form, may improve and add some properties to the basic composition of polymer or grinding wheel.

The added fillers may influence the density of grinding wheel, optical features, colour and change of surface qualities. They may also retain the shape of product during drying (shrinking), reduce bending, reduce thermal conductivity, change magnetic properties and essentially contribute to improvement and achievement of wanted mechanical properties of grinding wheels. Their ability of chemical reaction is particularly important, which means they can facilitate or inhibit chemical reactions of polymerisation, drying time and heat treatment, and the related degree of crosslinking.

The most frequently chosen fillers in the production of resin-bonded grinding wheels are pyrite, cryolite (fluoroaluminates), calcium carbonate, potassium fluoroaluminates (PAF), Wollastonite, and an inorganic pigment like "C-soot".

Fillers, such as Calcium carbonate and Wollastonite, increase the toughness (strengthen the grinding wheel) and contribute to higher efficiency and durability of grinding wheels at high temperatures and mechanical loads during the grinding process. When the heat is released during grinding, fillers react with the workpiece, and contribute to a more efficient grinding and thus protect the grains [8].

## 1.4 Impregnated Glass Cloth

In cutting discs and convex cutting discs with glass cloth only the mechanical structure of a grinding wheel is reinforced. Glass cloth is impregnated with phenol resins. The maximum rotational force the wheel can endure depends on the properties of the glass cloth fibres. Especially important properties are the endurance or tensile strength, and quality of the interweaving of fibres.

## 1.5 Microstructural Composition of Resin-Bonded Grinding Wheels

The basic composition of a grinding wheel is made of grains, binder, filler, pores and cracks, and glass-fibre

nets as additional reinforcement. Grains are used for grinding, binder holds grains together, and pores are responsible for the removal of chips. Grinding grains are capable of self-restoration (self-sharpening) and new grains appear on places, where worn grain falls out of the structure. This is a very important property of resin-bonded grinding wheels. If resin holds grains too tight, the restoration of the working surface of the grinding wheel is slow and pores get clogged, which reduces the efficiency of a grinding wheel. However, a grinding wheel is worn out too fast, if grains fall out, because resin failed to hold the grains together well.

## 2 EXPERIMENTAL PART

In the experimental part, analytical and statistical methods were applied in obtaining and evaluating the results. In order to determine the reliability of results, the Weibull statistical method and the calculated module, which is actually a quality criterion of resin-bonded grinding wheels have been used in the past [15].

The experimental part of the research was performed in the following way:

- an experimental part was prepared and executed with the purpose of determining the repeatability of results and comparability;
- a whole spectre of samples was prepared by implementing the procedure of determining the changes of functional properties of grinding wheels in a natural environment and under specific atmospheric conditions (humidity);
- a synthesis of findings was implemented and a model was created of time influence on mechanical features during ageing of grinding wheels in a natural environment under forced conditions;
- findings and conclusions have been made.

To obtain the results the following was applied:

- routine procedures in the industry, like internal technological rules and norms (preparation of samples and measurements of functional properties);
- procedures prescribed by standards (preparation of samples and measurements of mechanical properties and statistical data processing);
- procedures that have been designed by the authors (preparation of samples for the microstructural analysis).

For various types of grinding wheels of equal dimensions and quality, using the prescribed method of the grinding wheel manufacturer, we carried out

tests of maximum rotational speed (disintegration) and defined the cutting ability factors.

The microstructural analysis of samples was made on the basis of the imaging of samples on the scanning electron microscope in high vacuum. On the basis of the characterization of microstructures of grinding wheel samples, which were exposed to various thermo-mechanical impacts, we set a hypothesis (model) and determined the reasons for the downgrade in mechanical properties during ageing of grinding wheel.

For the purposes of the experimental study of the impact of ageing on mechanical and functional properties over a longer period, and due to easier traceability in the production, various types of samples have been prepared (six), separated by trademarks (label or TYPE 0X), which are presented in more detail in Table 1, where codes PL260, PL340 and PL380 suggest a different grammage of glass impregnated cloth, as a grinding wheel reinforcement.

**Table 1.** Basic types of grinding wheel samples

Sample no.:	Grinding wh. code:	Product composition (type and quality of reinforcement):
01	TYPE 01	No reinforcement, non-reinforced product
02	TYPE 02	2 pieces PL 340
03	TYPE 03	1 piece PL 340 and 1 piece PL 380
04	TYPE 04	2 pieces PL 380
05	TYPE 05	2 pieces PL 260
06	TYPE 06	2 pieces PL 380, grinding wheel heat processed again at 190 °C in the time of 6 hours

### 2.1 Disintegration

The concept of disintegration defines the rotational speed, where a grinding wheel is torn apart due to extreme centrifugal forces. Testing was performed on the machine, which continually increases rotational speed of the attached wheel to the value, at which the disc disintegrates.

The disintegration ability was tested on the machine PVM30, 50 Hz: rotational speed variation: Min/Max rpm: 4,500 min<sup>-1</sup> to 30,000 min<sup>-1</sup>, drive system: variable frequency unit, wheels diameter: 100 mm to 400 mm, spindle drive: motor-belt. each individual testing was undertaken on 1 piece of wheel. Tests were performed with 10 disintegration repetitions of grinding wheels.

Measurements or testing of maximum rotational speeds of grinding wheels were performed for basic types of grinding wheels (T01, T02, etc.).

In all cases, the same type of grinding wheel was used, F41 230 × 3(3.1) × 22 A30S. The average values of rotational speeds of grinding wheels where disintegration occurred are given in Table 2.

The results of measurements of rotational speeds of disintegration show that the lowest values of rotational speed and, consequently, of disintegration are around the 15<sup>th</sup> day of wheel ageing. Then, by the day 60, the values started growing again.

**Table 2.** Average values of rotational speeds [ $\text{min}^{-1}$ ] of wheel disintegration

Type of gr. wh.:	Day 1:	Day 15:	Day 60:
TYPE 01	9,860	9,610	9,693
TYPE 02	13,600	13,460	13,630
TYPE 03	13,690	13,650	14,020
TYPE 04	13,380	13,450	13,840
TYPE 05	13,340	12,930	13,230

With regard to the comparison of test results of various types of samples (different composition of glass cloth grammage), it has been determined that the downward trend of disintegration by day 45 is constant, after that the repeated growth was present in all types of grinding wheels.

## 2.2 Cutting Ability

The measurement of mechanical properties (cutting factor) of resin-bonded grinding wheels is a practical procedure (method), used for decades by all producers of resin-bonded grinding wheels [8]. The method was developed on the basis of practical experience of leading world producers of grinding wheels and is still used in a modified way by all the producers of grinding wheels (even though it is not standardised). The testing of cutting factor is carried out on automated machines of the biggest Italian producer, which enables making a comparison of products (grinding wheels) when the data is accessible.

The cutting ability of grinding wheel is actually its ability to cut off and remove material from the surface of a workpiece. It is defined by the cutting factor ( $f$ ) and the number of possible cuts of the grinding wheel on the test workpiece.

The cutting factor is the ratio between a chip ( $\Delta M_{ml}$ ) in grams of ground-off workpiece and the wear of grinding wheel ( $\Delta M_{gw}$ ) in grams of wheel wear, Eq. (1)

$$f = \frac{\Delta M_{ml}}{\Delta M_{gw}} \quad (1)$$

The cutting factor was determined for all types of grinding wheels on ten samples. In all cases the sample type of grinding wheel F41 230 × 3(3.1) × 22 A30S was used. The cutting factor was calculated on the basis of the data obtained with the test method of 30 cuts with a wheel.

The cutting factor was determined for all types of grinding wheels on ten samples. In all cases the sample type of grinding wheel F41 230 × 3(3.1) × 22 A30S was used. The cutting factor was calculated on the basis of the data obtained with the test method of 30 cuts with a wheel. So for each point on diagram (Figs. 2 to 6) was made test on 10 samples with 30 cuts (for each point on the graph has been made 300 tests - cuts and calculated mean value).

The cutting ability check procedures are defined in the internal standards of the manufacturer and are used for regular testing of grinding wheels in the production (monitoring and ensuring the stability of grinding wheels' quality).

To understand the concept better and to assess changes, more frequent measurements (from 1 day to 83 days) were initially performed on the sample TYPE 04 and a time diagram of cutting factor dependence was drawn, Fig. 2.

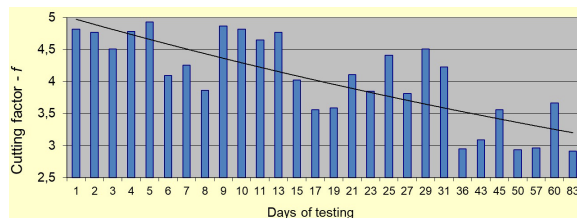


**Fig. 2.** Cutting factor by days for sample TYPE 04

As can be seen from Fig. 2, there is a great dispersion of value by individual days. For that reason and for easier interpretation of results and monitoring of time dependence, the diagrams of cutting factor dependence were made for the 1<sup>st</sup>, 2<sup>nd</sup>, 15<sup>th</sup>, 45<sup>th</sup> and 60<sup>th</sup> day for all samples, Figs. 3 to 6.

On the basis of the experimental preparation of samples, the results of measurements and calculations for a time period of 60 days, the following points were established:

- measurements confirm the actual impact of ageing during a time period and a direct impact on mechanical features of grinding wheels, i.e. cutting factor in grinding wheels;
- the implementation of more frequent measurements in fact somewhat distorts the entire image of monitoring the downgrade in the cutting ability of wheel, but it does not change

the trends shown by comparisons of results of the same grinding wheel in longer intervals during individual testing days;

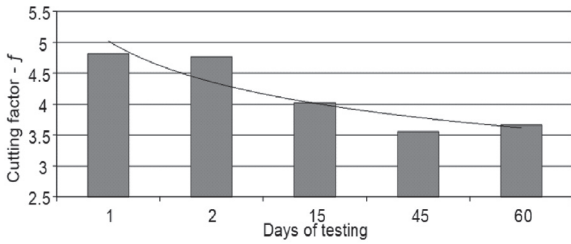


Fig. 3. Cutting factor by days for sample TYPE 04

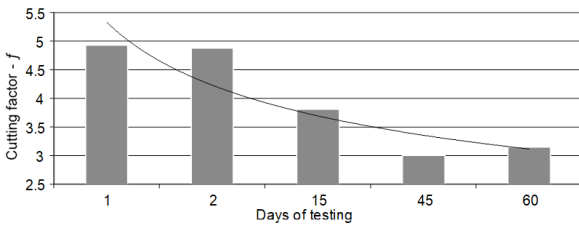


Fig. 4. Cutting factor by days for sample TYPE 03

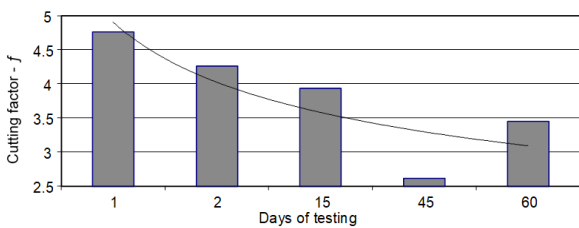


Fig. 5. Cutting factor by days for sample TYPE 02

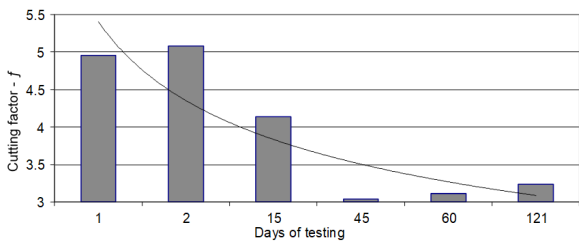


Fig. 6. Cutting factor by days for sample TYPE 05

- cutting factor in a time period of 45 days achieves the lowest value in all types of grinding wheels and is about 40 % lower;
- as the time period extends over 45 days, the ageing process stops and stabilizes, and the cutting ability slightly improves;
- repeated heat processing – i.e. drying of grinding wheels at an appropriate work temperature results in the mechanical properties (cutting ability) reversibly returning to original production values, Fig. 7;

- the results and findings in the paper are a result of monitoring of simultaneously measured samples of grinding wheels during a longer period of time, with the same technological processes of the same batch of prepared mixture (raw material). The measurements of mechanical properties (the measurements of the cutting factor and rotational speed) have shown that significant changes of mechanical properties of grinding wheels have occurred during the monitored period. From the findings it is evident that the mechanical changes do not occur as a result of in-built raw materials and changes in the geometry of the grain during the grinding wheel use, but as a consequence of what happens in the matrix of the composite due to the exposure of the composite matrix to the environmental influence where the grinding wheels have been stored;
- atmospheric conditions of storage (humidity and temperature) certainly have a decisive impact on the mechanical properties of grinding wheels.

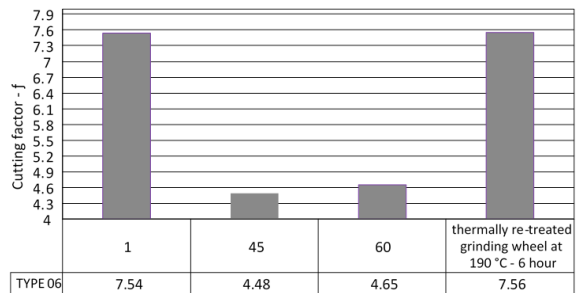


Fig. 7. Cutting factor by days for sample TYPE 06 (repeated heat processing)

### 2.3 Microstructure of Grinding Wheels

Microstructural analysis of samples was based on the imaging of samples on a scanning electron microscope (Quanta 200 3D) with wolfram cathode as the source of electrons in high vacuum. The microscope has an installed detector for bounced off electrons, which obtains the contrast between the areas of sample with a different chemical composition (Z-contrast).

On the basis of the characterisation of the microstructures of grinding wheel samples, which were exposed to various thermo-mechanical impacts, the authors designed the models of mechanisms of changes in the microstructure of grinding wheels during ageing.

In search of the answers for possible causes for the change of mechanical properties of grinding wheels during their use in a longer period, the

metallographic analyses of samples of microstructure of matrix composite of resin-bonded grinding wheels had been carried out. By using and analysing different magnifications of samples, we determined what is happening to the microstructure or the binding matrix of the samples, the changes of pores in the matrix, the occurrence of pores, their migration through the composite matrix, the performance of grains, their deviation from the binding matrix and the falling out of matrix connected with that. Consequently, the result are findings on the change of mechanical properties of the monitored samples, thermally treated with cutting in relation to the compared etalon of the same sample that was not exposed to usage, that is to cutting. In all cases, the same type of grinding wheel was used, F41 230 × 3(3.1) × 22 A30S.

In order to confirm the actual reasons for the downgrade in the functional properties of wheels throughout the measured period, we prepared samples of test pieces for the microstructural analysis, Table 3.

**Table 3.** Preparation of samples for the microstructural analysis [15] and [16]

Sample code / meas. date	Sample description	Sample processing
Sample A /07.02	Sample analysed 5 days old	Wheel not used – measurement standard
Sample B /07.02	Sample analysed 5 days old	5 cuts with grinding wheel
Sample C /03.03.	Sample analysed 30 days old	Additional force humidification 30 days and 5 cuts – 1 % humidity
Sample D /03.03	Sample analysed 140 days old (containing 1 % moisture)	Stored under normal conditions (40 % humidity and 15 °C) and 5 cuts

Figs. 8 to 10 show images of different magnifications of the microstructure of grinding wheel sample A that was 5 days old. Grinding wheel had not yet been used. Images of the microstructure of grinding wheel served as a comparable measurement standard in observing the changes in the microstructure of grinding wheel samples, which are intended for cutting.

Figs. 11 and 12 show the images of the microstructure of grinding wheel sample B, 5 days old. Grinding wheel is shown at different magnifications and had already been used.

Figs. 13 and 14 show images of the microstructure of grinding wheel sample C, 30 days old, at different magnifications. The grinding wheel was additionally aged (content of 1 % moisture) and already in use.

Figs. 15 and 16 show the images of the microstructure of grinding wheel sample D, 140 days old, at different magnifications. The grinding wheel was stored under normal conditions (~40 % humidity and ~15 °C, moisture content of 1 %). The grinding wheel had already been used.

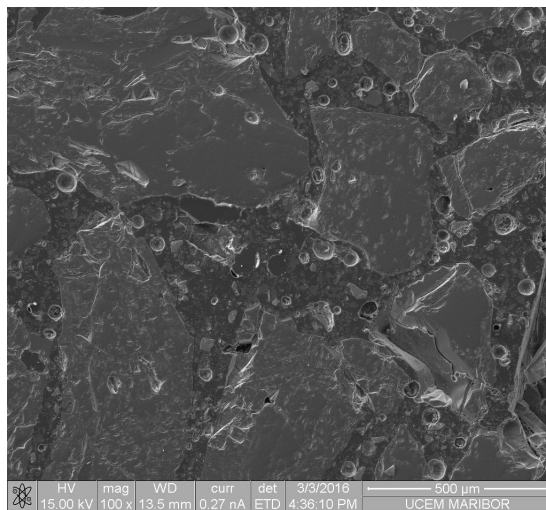


**Fig. 8.** Microstructure of grinding wheel sample A/07.02 [15]

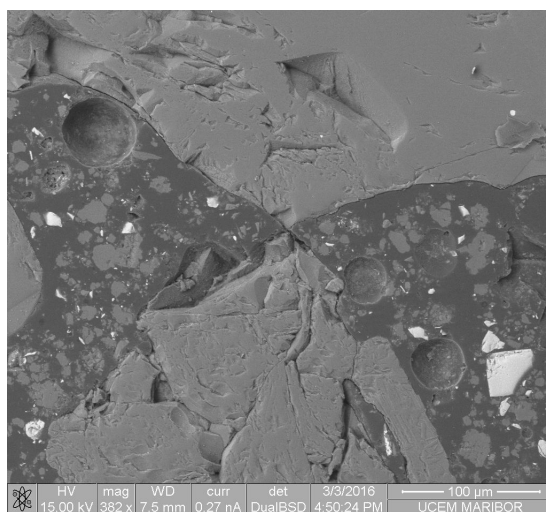


**Fig. 9.** Microstructure of grinding wheel sample A/07.02 [15]

On the basis of the method of cross-observation, comparison and analysis (Figures 8 to 16) of the microstructure of grinding wheels, which were exposed to various thermo-mechanical impacts, the following conclusions can be given:

- microstructure of the grinding wheel matrix that was not used for cutting is significantly different from the grinding wheel matrix that was used for cutting (Figs. 8 and 15);

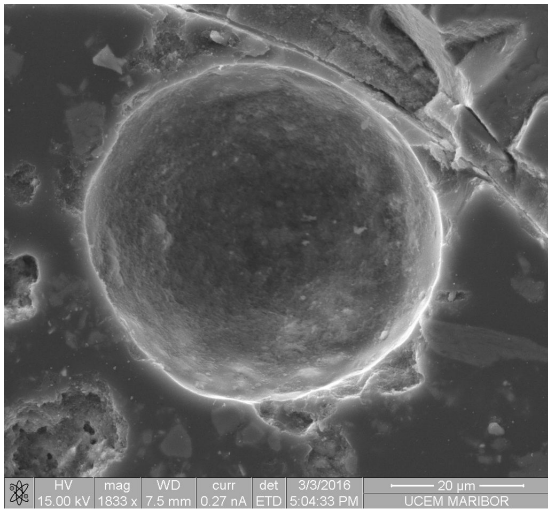


Fig. 10. Microstructure of grinding wheel sample A/07.02 [15]

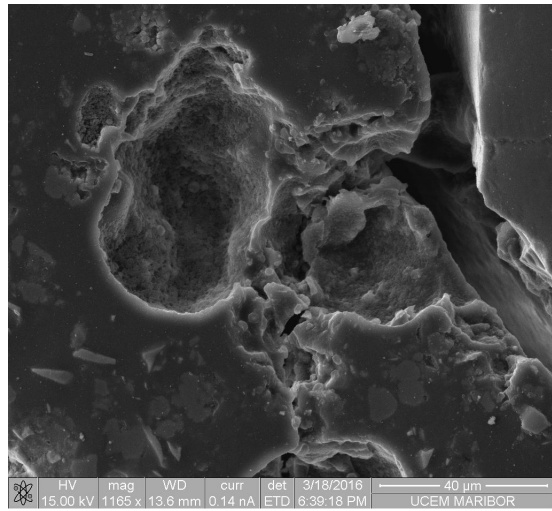


Fig. 13. Microstructure of grinding wheel sample C/03.03. [15]

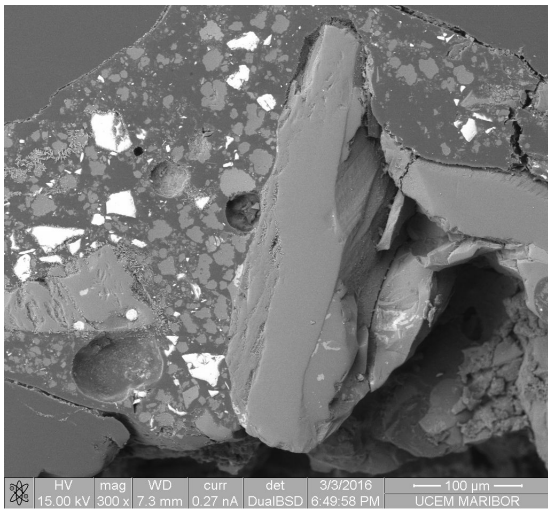


Fig. 11. Microstructure of grinding wheel sample B/07.02 [15]

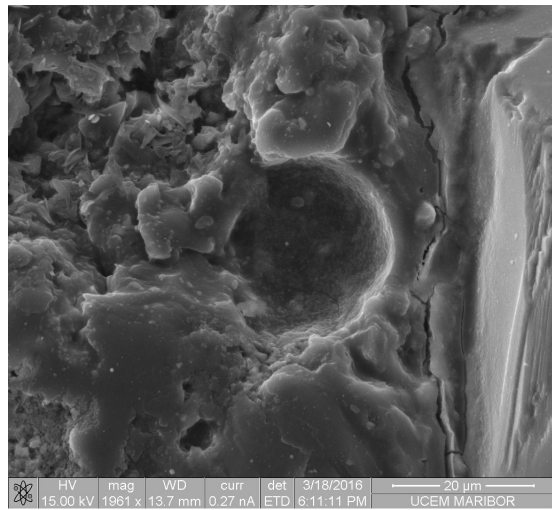


Fig. 14. Microstructure of grinding wheel sample C/03.03 [15]

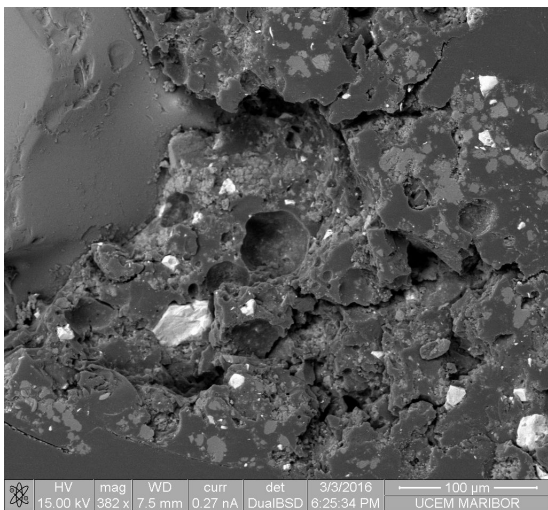


Fig. 12. Microstructure of grinding wheel sample B/07.02 [15]

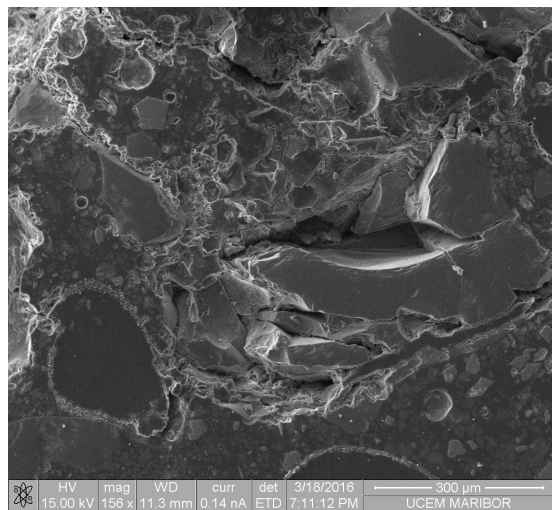
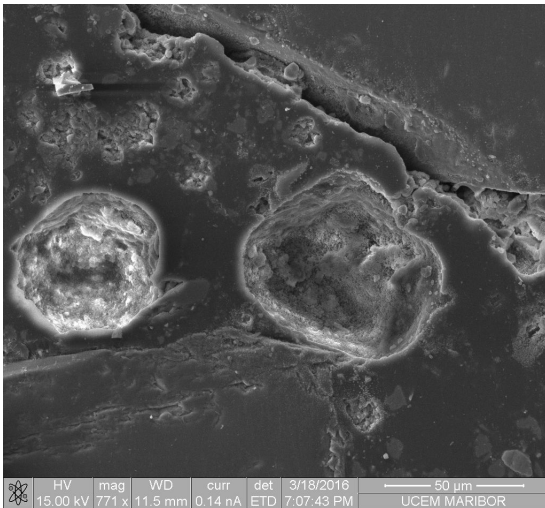


Fig.15. Microstructure of grinding wheel sample D/03.03 [15]



**Fig. 16.** Microstructure of grinding wheel sample D/03.03 [15] and [16]

- with the accelerated ageing method, the authors successfully inserted a quantity of water (1 % of moisture) into the grinding wheel pores, which is similar to that of the grinding wheel, which is stored under normal conditions for a much longer period, but such procedure has a negative effect on the internal structure of polymer matrix (microstructure) of grinding wheel (Figs. 13 and 16);
- the effect of ageing of grinding wheel is essentially related to the number and size of pores, which are caught in the polymer matrix of phenol-formaldehyde resin (Figs. 11 and 15);
- heat is generated during grinding and heats the water (atmospheric humidity), which is present in grinding wheel pores. It is transformed into a gas phase – water vapours, which causes a rise or increase of hydrostatic pressure of water vapours in pores (Figs. 10 and 16);
- in critical threshold values of the increased hydrostatic pressure in grinding wheel pores, it was first noticed that the internal deformation of pores occurs and in the next phase the destruction of the material across the circumference of pores caught in the polymer binder matrix (Fig. 16);
- water vapour, which penetrates the wall and travels through the matrix, causes cracks in polymer binders. Cracks travel over the matrix and stop on the edge of grain (Figs. 13 and 16);
- a dilatation crack is formed between the structurally homogenous grain and matrix, which first results in the downgrade of hardness of polymer matrix and after that also in faster fall-

off of abrasive grains of the phenol-formaldehyde matrix and thereby in a significant downgrade in the grinding wheel cutting ability in the first 45 days from the date of production (up to 40 %) (Figs. 2, 12 to 14);

- phenol-formaldehyde resin (duromer) in grinding wheel cross-binds individual abrasive grains. By nature, duromer is very hard and fragile, so the formation of cracks in the matrix contributes to a much faster reduction of grinding wheel hardness and, consequently, to the downgrade in functional and mechanical properties of grinding wheel (Figs. 11 to 13);
- increased presence of water vapours in pores of the polymer matrix of wheel increases internal tensions between the matrix, grain and glass impregnated cloth, which strengthens the microstructural matrix of wheel, which has a positive impact on the process of material destruction due to centrifugal forces, which occur when examining the maximum rotational speed of grinding wheel (disintegration testing) (Table 2).

Table 4 presents a comparison of characterisation based on the cross-observation, comparison, and analysis of the grinding wheel microstructural images.

### 3 DISCUSSION

The research of the cutting factor and maximum rotational speed of resin-bonded grinding wheels with corundum and SiC grains was performed within a period of 60 days with the purpose of determining the influence of ageing on their functional properties. The following conclusions can be drawn based on the results of experimental measurements:

- Results of measurements of rotational speeds of disintegration indicate that the lowest values of rotational speeds and thereby of disintegration are around the 15th day of grinding wheel ageing. After that, the values of rotational speeds start slowly growing again up to the 60th day.
- Trend in growth of rotational speeds of grinding wheels continues also in the later period and can actually exceed the original values.
- Results of measurements of the cutting factor confirm the actual influence of ageing during the monitored period and a direct influence on the mechanical properties of grinding wheels, i.e. the grinding wheel cutting factor.
- The implementation of more frequent measurements in fact somewhat distorts the entire image, but it does not change the trends shown

**Table 4.** Comparison of characterisation of grinding wheel microstructures

Sample code/Date of measurement:	Description of sample microstructure	Comment/notes:
Sample A/07.02./ grinding wheel analysed, 5 days old / grinding wheel not used – comparison measurement standard to other samples.	Microstructure of grinding wheel is quite homogeneous; pores are spherical, polymer well crosslinked and bonded to grains. The sample serves as a comparison measurement standard to other observed samples.	Pores have proper shapes, relatively well distributed throughout the polymer matrix there, are no present cracks and fractured grains, grains are fused along edges, and grain fractures run on proper planes. Pores themselves are highly spherical shape; on the surface of the pores is no indication of any plastic deformation or cracks. Polymer matrix around grains is unchanged, inclusions of fillers are well seen, and there is still no change of the microstructure.
Sample B/07.02./ grinding wheel analysed 5 days old / 5 cuts done with grinding wheel.	Microstructure of grinding wheel is still homogeneous, pores are slightly deformed over circumference, tears of binder parts are presents around grains and minor deformities are also present. Spherical pores are still clearly seen.	Pores already have partly improper shapes, cracks are present around grains and binder is separating from grain. The structure of polymer binding has also changed and is more homogenous (aggregates of fillers are not visible any more). The process of destruction of the polymer matrix already started, which results in a partial breakdown of the matrix strength, but due to the small quantity of air humidity content of the moisture, the process of destruction is not so pronounced and noticeable. Also, the size and length of the cracks in the matrix is not so clearly visible.
Sample C/03.03./ grinding wheel analysed 30 days old / additional forced humidification 30 days and 5 cuts (content of 1 % moisture).	Microstructure of grinding wheel has changed the most in this sample, pores have completely lost their original shape and many grains are torn. Very pronounced and branched cracks appear throughout the matrix, the grains are removed from the polymer matrix. Polymer structure is completely ruined. Cracks between grain and matrix are clearly seen. Due to the process of breakthrough of water vapor through the wall, the appearance of eruptive lanches, from which the cracks are spreading in the direction of breakthrough through the bonding matrix to the abrasive grains, where they stop. In the sequel, the water vapor, which spreads and travels through the cracks, deflects and drains abrasively grain from the binding matrix. Critical change of microstructure, many stripped-off grains and the most damaged microstructure.	Due to the forced addition of moisture into the polymer matrix, the most pronounced process of destruction of the polymer matrix is present here and its large deviation from the ideal structure, which results in a breakdown of the matrix strength (the size and length of the cracks in the matrix is clearly visible, the grains are moving away from the binding matrix itself) in accordance with this process the mechanical strength and durability of the resinoid grinding wheel during use is dropped extremely quickly. Destruction of homogeneity of binders due to changes in pores, the changes are a result of hydrostatic overpressure of water vapour in pores, penetration in the walls of pores can be seen in the weakest part. Deformation continues through the cracks in the matrix, which lead to edges of grains. Grains are eliminated from the matrix. Eruptive fields are present in places, where pores used to be. Penetration occurred in the weakest part of the pore wall, water vapour injects cracks in the matrix, cracks travel to the edges of the grains.
Sample D/03.03./ grinding wheel analysed 140 days old / Normal storage (40 % humidity and 15 °C) and 5 cuts (content of 1 % moisture).	Microstructure is worse than the sample B, but much better than sample C. Pores are partly deformed, grains are already separating from the binder matrix, but there are not so many eruptive fields present around the pores in the matrix as in the sample C. The process of destruction of the pores is also present here, as in sample B and C, but due to the lower amount of moisture in the matrix, the process is not as intense as in the sample C. The pores are less damaged, the eruptive zones are smaller, the cracks are less intense and branched, the deviation polymer matrix grain is not as pronounced as in the case of sample C.	Pores are deformed in the sample D more than in the sample B, destruction of binder matrix is clearly present. There are deformations around grains, but the matrix itself is not that extremely damaged as in the case of sample C. In pores, there is already an ongoing process of hydrostatic pressure of water vapour on walls. In pores, which are the closest to grains, there is already the same process of wall penetration; there are visible expansions of water vapour through the cracks in polymer matrix. Crack stops at the edge of grains, but in this case cracks around grains are smaller, and still bigger than in sample B. For that reason, less grains fall off the polymer matrix.

by comparisons of results of the same grinding wheel in longer intervals between individual testing days.

- Cutting factor achieves the lowest value in a period of 45 days in all tested types of grinding

wheels. The downgrade in cutting factor may amount up to 40 %.

- As the period is extended above 45 days, the ageing process stops and stabilises, and the cutting ability somewhat improves.

- Slight growth in the cutting factor of the grinding wheel continues also in the subsequent period, but it does not achieve the original properties.
- Repeated heat processing – thermal treated(drying) of grinding wheel under original conditions leads to the initial mechanical properties of grinding wheel (cutting factor values).
- Atmospheric storage conditions (humidity and temperature) certainly have a decisive impact on the mechanical features of resin-bonded grinding wheels.

On the basis of the findings it can be concluded that, during the observed period, atmospheric humidity has a positive influence on the disintegration of a grinding wheel and thereby on the increase of rotational properties and a much stronger negative influence on the cutting properties of grinding wheels during ageing.

#### 4 CONCLUSIONS

The research explores the impact of ageing in specific time sequences on the mechanical and functional properties of grinding wheels. On the basis of the results, it can be seen that the ageing process happens much faster than predicted. The highest downgrade in the mechanical properties of resin-bonded grinding wheels occurs in the first 45 days after the production.

Simultaneous comparisons of results of the measurements of the wheel cutting factor and the maximum rotational speed have shown that the ageing process has a negative impact on both functional properties in the first phase, but then the trend is reversed.

The measurements of mechanical tensile strengths of grinding wheels have confirmed the findings on a very dynamic and fast ageing of grinding wheel, that the method of determining tensile strength is very useful, reliable and repeatable, and that the statistical processing of measurement results by means of the Weibull model delivers the answer about the correct method of execution of measurements [15].

Cross characterisation of microstructure of grinding wheel samples, which were exposed to different thermomechanical influences has shown how and in what way the ageing process in grinding wheels takes place and what is the extent of impact of the moisture caught in pores of polymer matrix. The size and quantity of pores caught in the polymer matrix of grinding wheel have an indisputably high influence on the course and speed of ageing.

Reduction and control of the occurrence of pores is related to how and in what way the producers of grinding wheels master the entire production process. It is important that the raw materials used are well monitored, technologically verified and controlled so that the process of substance preparation and stabilisation is of good quality and repeatable. The occurrence and quantity of pores and, consequently, the change of properties of grinding wheel during ageing is highly influenced also by the proper selection of the length, inclination of thermal diagram and control during the total thermal procedure of heating and cooling of the grinding wheel.

Consequently, the conditions under which the grinding wheel was stored have a very high impact on the speed of ageing. Therefore, the producers of artificial resin-bonded grinding wheels are faced with a challenge of how to protect the wheel from unnecessary atmospheric impacts.

#### 5 ACKNOWLEDGEMENTS

The authors would like to thank the Faculty of Mechanical Engineering, University of Maribor for the support in research and experimental work, Mamut Tim Ltd. and Swatycomet Ltd. (ex - Comet d.d.) for manufacturing and testing the grinding wheel samples.

#### 6 REFERENCES

- [1] Dai, C., Ding, W., Xu, J., Fu, Y., Yu, T. (2017). Influence of grain wear on material removal behavior during grinding nickel-based superalloy with a single diamond grain. *International Journal of Machine Tools and Manufacture*, vol. 113, p. 49-58, DOI:10.1016/j.ijmactools.2016.12.001.
- [2] Miao, Q., Ding, W., Fu, D., Chen, Z., Fu, Y. (2017). Influence of graphite addition on bonding properties of abrasive layer of metal-bonded CBN wheel. *International Journal of Advanced Manufacturing Technology*, vol. 93, no. 5-8, p. 2675-2684, DOI:10.1007/s00170-017-0714-2.
- [3] Ding, W.F., Xu, J.H., Chen, Z.Z., Yang, C.Y., Song, C.J., Fu, Y.C. (2013). Fabrication and performance of porous metal-bonded CBN grinding wheels using alumina bubble particles as pore-forming agents. *International Journal of Advanced Manufacturing Technology*, vol. 67, no. 5-8, p. 1309-1315, DOI:10.1007/s00170-012-4567-4.
- [4] Zhu, Y., Ding, W., Yu, T., Xu, J., Fu, Y., Su, H. (2017). Investigation on stress distribution and wear behavior of brazed polycrystalline cubic boron nitride superabrasive grains: Numerical simulation and experimental study. *Wear*, vol. 376-377, p. 1234-1244, DOI:10.1016/j.wear.2016.12.048.
- [5] Linke, B. (2016). *Life Cycle And Sustainability Of Abrasive Tools*, Springer International Publishing Geneva, p. 64 -79, DOI:10.1007/978-3-319-28346-3.

- [6] Ding, W., Linke, B, Zhu, Y., Li, Z., Fu, Y., Su, H., Xu, J. (2016). Review on monolayer CBN superabrasive wheels for grinding metallic materials. *Chinese Journal of Aeronautics*, vol. 30, no. 1, p. 109-134, DOI:10.1016/j.cja.2016.07.003.
- [7] Klocke, F., Brinksmeier, E., Evans, C., Howes, T., Inasaki, I. Minke, E., Tönshoff, H.K., Webster, J.A., Stuff, D. (1997). High-speed grinding-fundamentals and state of the art in Europe, Japan, and the USA. *CIRP Annals*, vol. 46, no. 2, p. 715-724, DOI:10.1016/S0007-8506(07)91100-2.
- [8] Gardziella, A., Pilato, L.A., Knop, A., (2000). *Phenolic Resins: Chemistry, Applications, Standardization, Safety and Ecology*. Springer, Berlin, DOI:10.1007/978-3-662-04101-7.
- [9] Higuchi, M., Urakawa, T., Morita, M. (2001). Condensation reactions of phenolic resins. 1. Kinetics and mechanisms of the base-catalysed self-condensation of 2-hydroxymethylphenol. *Polymer*, vol. 42, no. 10, p. 4563-4567, DOI:10.1016/S0032-3861(00)00808-9.
- [10] Linke, B.S. (2015). A review on properties of abrasive grits and grit selection. *International Journal of Abrasive Technology*, vol. 7, no. 1, p. 46-58, DOI:10.1504/IJAT.2015.070582.
- [11] Asami M., Santorelli M., Pilato, L. (ed.) (2010). *Phenolic Resins: A Century of Progress*. Chapter 13, Abrasives, p. 316, Springer, Berlin Heidelberg, DOI:10.1007/978-3-642-04714-5\_13.
- [12] Kirsch, B., Aurich, J.C. (2014). Influence of the macrotopography of grinding wheels on the cooling efficiency and the surface integrity. *Procedia CIRP*, vol. 13, p. 8-12, DOI:10.1016/j.procir.2014.04.002.
- [13] Öpöz, T.T., Chen, X. (2012). Experimental investigation of material removal mechanism in single grit grinding. *International Journal of Machine Tools and Manufacture*, vol. 63, p. 32-40, DOI:10.1016/j.ijmactools.2012.07.010.
- [14] Pilato L., (2010). *Phenolic Resins*, Chapter 4, Resin Chemistry Springer - Verlag Berlin Heidelberg, p. 44 - 46, p. 53-57. DOI:10.1007/978-3-642-04714-5\_13.
- [15] Matavž, A. (2016). *The Impact of Ageing on Mechanical Characteristics of Resin Bonded Wheels with Corundum and SiC Grains*. PhD Thesis. University of Maribor, Faculty of Chemistry and Chemical Engineering, Maribor.
- [16] Matavž, A., Kroppe, J., Goričanec, D., Trop, P., Urbančl, D., Žagar, T., Anžel, I. (2016). The ageing of resin-bonded grinding wheels with corundum and SiC grains. *9<sup>th</sup> International Conference on Sustainable Energy and Environmental Protection: SEEP Conference Proceedings*, Kayseri, Turkey, p. 439-444.

# Control System Design for a Centrifuge Motion Simulator Based on a Dynamic Model

Jelena Vidaković<sup>1,\*</sup> – Vladimir Kvrđić<sup>2</sup> – Mihailo Lazarević<sup>3</sup>

<sup>1</sup> University of Belgrade, Lola Institute, Serbia

<sup>2</sup> University of Belgrade, Institute Mihajlo Pupin, Serbia

<sup>3</sup> University of Belgrade, Faculty of Mechanical Engineering, Serbia

*This paper presents a dynamic model-based design of a control system and an approach toward a drive selection of a centrifuge motion simulator (CMS). The objective of the presented method is to achieve the desired performance while taking into account the complexity of the control system and the overall device cost. An estimation of a dynamic interaction of the interconnected CMS links motions is performed using the suitable inverse dynamics simulation. An algorithm based on the approximate inverse dynamics model is used within the drive selection method. The model of the actuator's mechanical subsystem includes the effective inertia (inertia reflected on the rotor shaft) calculated from the inverse dynamics model. A centralized control strategy based on a computed torque method is considered and compared to traditional decentralized motion controllers. To obtain an accurate comparison of the suggested control methods through a realistic simulation, structural natural frequencies of the manipulator links are considered, and the actuator capabilities are taken into account. The control system design and simulation methods and the drive selection strategies, presented here for the CMS, are applicable within the general robot manipulator's domain.*

**Keywords:** robot dynamics, robot control, computed torque method, centrifuge

## Highlights

- A dynamic model-based control system design of a centrifuge motion simulator.
- A dynamic model-based approach toward an adequate drive selection of a centrifuge motion simulator.
- Realistic simulation of the control system takes into account natural frequencies of the mechanical structure, actuator torque limits and inertia reflected on the rotor shafts.

## 0 INTRODUCTION

Pilots of the newest generation of combat aircraft are exposed to dangerous effects of high  $G$  forces and sudden angular movements in all three aircraft axes, with accelerations of up to  $9g$  ( $g = 9.81 \text{ m/s}^2$  is Earth's gravitational acceleration), and acceleration rates of up to  $9 \text{ g/s}$ . Herein, the acceleration force  $G = a/g$  corresponds to the magnitude of acceleration acting on the pilot,  $a = (a_n^2 + a_t^2 + g^2)^{1/2}$ , where  $a_n$  and  $a_t$  are the normal and tangential accelerations, respectively [1]. Under such conditions, the pilot's ability to control the aircraft is reduced, and the pilot may suffer from a loss of consciousness induced by high  $G$  loads (G-LOC). Researchers are seeking answers to whether pilots can cope with the physiological and psychological requirements placed upon them with the newest generation of fighter aircraft [2]. High  $G$  training in a centrifuge motion simulator (CMS) is used to artificially increase the inertial force under controlled conditions. In this study, 'open loop flight simulations', with predefined trajectories, are considered.

The virtual structure of a CMS is made using CATIA, as shown in Fig. 1. The CMS is modelled

and controlled as a 3 degrees of freedom (DOF) robot manipulator with revolute joints. The pilot seat (or chest/head) acts as an end-effector. In Fig. 2, rotational axes and frames of the CMS are given. The CMS arm rotates about the vertical axis. It carries a ring that rotates about the roll axis, and a gondola rotating about the pitch axis. Denavit-Hartenberg notation is used for geometry model development [3]. Frame with index 3 is attached to the end-effector (the pilot's seat). An inverse dynamics (ID) algorithm, which computes the torques to be applied to the joints in order to obtain their commanded motions, for the CMS is given in [1] in the form of recursive Newton–Euler equations.

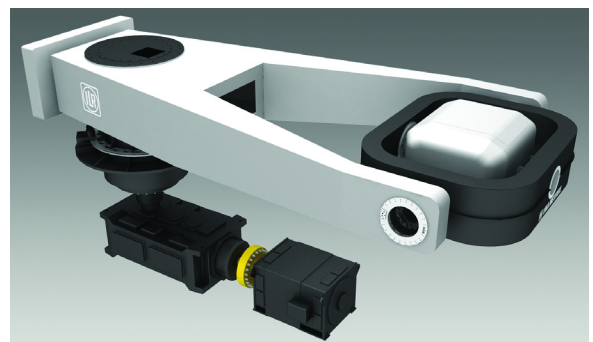


**Fig. 1.** CMS with 3 DOF

\*Corr. Author's Address: University of Belgrade, Lola Institute, Kneza Višeslava 70a, Belgrade, Serbia, jelena.vidakovic@li.rs

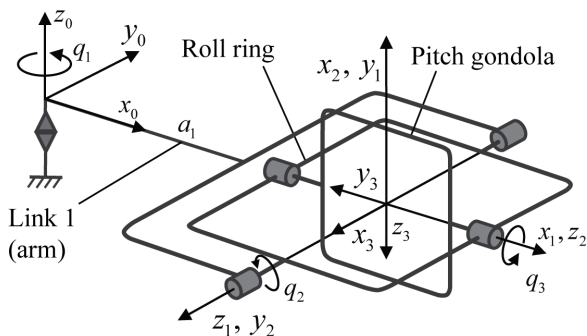


Fig. 2. CMS rotational axes and frames

Robot control is a challenging task due to high nonlinearity of robot dynamics and coupling effects between the joints. To deal with the nonlinearity and time variability of robot dynamics, many advanced control strategies have emerged, including adaptive control [4] and [5], sliding mode control [6], intelligent control [7] and [8], etc. Regarding the problem of uncertainty of kinematic and dynamic robot parameters, control schemes that make use of soft computing methods including neural networks [9] to [11] and fuzzy logic [12] have been developed. In order to improve trajectory tracking, various optimization techniques are used within motion controllers, [13] to [15]. Joint space control methods, which are adequate in situations in which the manipulator tasks can be accurately preplanned and little or no online trajectory adjustments are necessary [16], can be classified into decentralized (when a single manipulator joint is controlled independently of the others) and centralized (when dynamic interaction effects among the joints are considered) techniques [17]. The advantage of one particular control method over another depends on the robot application, performance requirements, characteristics of the mechanical design and actuators, implementation requirements, etc. A CMS falls into the category of high-assurance systems requiring a high level of robustness in terms of system performance and a guaranteed set of critical properties including reliability, availability, safety, and security [18]. The application of empirically validated control methods in systems in which their failure can result in a loss of life or property is questionable and must always be backed up by techniques that minimize the possibility of such undesirable effects.

This paper deals with a control system design and a drive system selection of the CMS that takes into account the desired performance, the control system complexity, and the overall system cost.

There are very few papers in the literature that deal with CMS motion control. In [19], a similar

centrifuge, driven with hydraulic actuator system, is presented. The centrifuge arm is controlled with conventional proportional-derivative (PD) speed feedback, while fuzzy sliding mode control is applied for the roll and pitch angles control. Simulation results for the trajectory tracking are given, divided into the increasing and decreasing  $G$  load profile segments without transitions in  $G$  load rates. In [20], another realization of the centrifuge is described, with the study of control methods based on the concepts of adaptive feedback linearization; some numerical simulation is provided for the less challenging trajectories.

Within a choice of the prospective control system for a robot manipulator in practice, complexity and implementation requirements may play significant roles. In regard to the potential use of advanced control schemes, given that such utilization can lead to complex control structures, benefits have to be clearly determined in comparison to the simpler control strategies. In this perspective, within the control system design for the CMS questions arise regarding whether a dynamic model should be taken into account, and if so, how. Methods used to answer this question for the CMS are presented herein.

In this study, the thorough analysis and suitable simulation of the CMS manipulator's dynamic model are used for an assessment of the nature of the mutual influences of the interconnected links' motions, from which conclusions on the correct control strategy regarding both the performance and the complexity are drawn. On the basis of the results of the presented ID model-based simulations, a single joint servo control is proposed for the CMS arm control. For the second (ring) and third (gondola) axes, the addition of a feedforward computed torque compensator [21] to the feedback controller is considered.

To obtain an accurate comparison of the suggested control methods through a realistic simulation, the following conditions are met: 1) the effective inertia (inertia reflected on the rotor shaft), which provides a realistic process model, is calculated from the ID for the desired joint trajectories and chosen actuator model, 2) the choice of feedback controller gains considers the structural natural frequencies (herein obtained using CATIA software), and 3) the torque limits for the chosen actuators are included in the simulation of the controlled process. Compared to the previously published work in [19] and [20], the performance of the considered control methods is here given for the significantly more challenging CMS trajectory profile, with the maximum acceleration magnitude of  $9g$ , the maximum acceleration rate of

$\pm 9g$  per second, and with provided transitions in  $G$  load rates.

A CMS falls into the category of heavy machinery (herein, the CMS arm length  $a_r$  is 8 m, its mass is approximately 42 tons, the whole assembly mass is 45 tons). Combined with the challenging joint trajectories, actuators with desired powers have huge weights. It is essential for motors to have sufficient power to rotate the links rapidly as well as to be lightweight. Bigger actuators induce an increase in manipulator inertia, energy consumption, and cost of the overall system.

In this study, a procedure based on the approximate inverse dynamics (aID) model [1], is used within the drive selection problem. The presented procedure enables the choice of actuators in terms of their power and weights in such a way that the smallest actuators with the potential to achieve the required joints' motions are determined. When the actuators are chosen, their model parameters are included within control system simulations.

The remainder of this paper is organized as follows. In section 1, the methodology for the design of the motion control system and the selection of CMS drives based on dynamic manipulator modelling are presented. Results and a discussion are provided in section 2. Concluding remarks are given in section 3.

## 1 DYNAMIC MODEL-BASED DESIGN OF CMS MOTION CONTROLLER

The required task for the CMS manipulator is to achieve commanded acceleration force  $G$  at the centre of the gondola, where the pilot's seat, chest, or head is accommodated. The desired tasks are defined using an application program written in L-IRL robot programming language, modified for flight simulators [22]. A trajectory planner for the CMS is implemented in L-IRL through the algorithm used to calculate the joint trajectories  $q_k, \dot{q}_k, \ddot{q}_k, k = 1, 2, 3$  which produce the desired change in  $G$ -force at the centre of the gondola with specified jerks of  $G$ , [1] and [23]. For the commanded end-effector acceleration ( $G$  load) given in Fig. 6, the positions, velocities, and accelerations of the CMS joints,  $q_k, \dot{q}_k, \ddot{q}_k, k = 1, 2, 3$  obtained as the outputs of the trajectory planner, are given in Fig. 3. Challenging kinematic profiles with the rapid changes in velocity and large jump-like changes in acceleration, particularly for axes 2 and 3, are required.

On the basis of the maximum values of the actuating torques obtained from the ID model for the most demanding commanded CMS trajectory, the initial selection of the corresponding actuators is

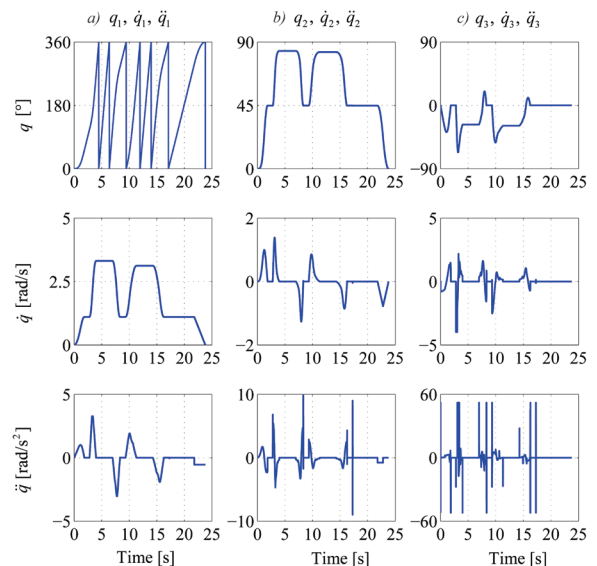


**Fig. 3.** Positions, velocities, and accelerations of CMS joints; a)  $k = 1$ , b)  $k = 2$ , and c)  $k = 3$

performed [1]. For the first axis (centrifuge arm), a DC motor with a rated torque of  $M_{1r} = 41200$  Nm was chosen. The motor overload capability is 2; the chosen gearbox has a gear ratio of 16.5 and an efficiency of  $\eta_1 = 0.94$ . This gives a short time maximum torque of  $M_{1max} = 1.28 \cdot 10^6$  Nm (for less than 5 s). For the axes 2 and 3, the actuating system consisting of two torque motors with a maximum torque of  $M_{imax} = 10900$  Nm [24] is considered for each axis.

Motion equation for a manipulator with  $n$  degrees of freedom can be described in the following matrix form:

$$\mathbf{D}(\mathbf{q})\ddot{\mathbf{q}} + \mathbf{H}(\mathbf{q}, \dot{\mathbf{q}})\dot{\mathbf{q}} + \mathbf{g}(\mathbf{q}) = \boldsymbol{\tau}, \quad (1)$$

where  $\mathbf{D}(\mathbf{q})$  is  $n \times n$  inertia/mass matrix,  $\mathbf{H}(\mathbf{q}, \dot{\mathbf{q}})$  is an  $n \times n$  matrix of centrifugal and Coriolis terms,  $\mathbf{g}(\mathbf{q})$  is  $n \times 1$  is a vector of gravitational terms and  $\boldsymbol{\tau}$  is  $n \times 1$  vector of the actuating torques. For an easier description regarding control methods used herein for the CMS, Eq. (1) is rewritten in Eq. (2),  $k = 1, 2, \dots, n$ , as a set of  $n$  coupled nonlinear differential equations.

$$\sum_{j=1}^n d_{kj}(\mathbf{q})\ddot{q}_j + \sum_{j=1}^n \sum_{i=1}^n h_{kji}(\mathbf{q})\dot{q}_j\dot{q}_i + g_k(\mathbf{q}) = \tau_k. \quad (2)$$

With the recursive Newton–Euler method, the actuating torque  $\tau_k$  in Eq. (2) is obtained as the  $z$  component of the vector  $\hat{\mathbf{m}}_k$ , which is a moment exerted on link  $k$  by link  $k-1$ , described in the frame attached to joint  $k-1$  [25], i.e.  $\tau_k = \hat{m}_{zk}$ . Hereafter, an over-line hat notation (^) along with subscript  $k$  is used to denote the matrices, vectors, and their

components described in the frame attached to link  $k$ . From Eqs. (1) and (2), it is clear that when large operational speeds and accelerations are required, the nonlinear coupling terms may have a strong influence on the system performance. In this case, it is advisable to design a control system that takes advantage of the detailed knowledge of manipulator dynamics [17].

**1.1 Determination of Dynamics Effects of the CMS Interconnected Links' Motions**

In this paper, the mutual dynamic effects of the interconnected links' motions of the CMS are analysed using ID-based simulations. For a specific  $k^{\text{th}}$  joint, influences of the other links motions,  $j=1, 2, \dots, n$ ,  $j \neq k$ , are estimated through their contribution within the value of the  $k^{\text{th}}$  joint actuating torque. Following ID simulations are used for this purpose.

For a specific commanded motion of the manipulator, outputs of the trajectory planner are obtained in the form of the time sequences of the joints' trajectories  $\tilde{q}_j, \dot{\tilde{q}}_j, \ddot{\tilde{q}}_j, j=1, 2, \dots, n$ , which are used as the input for the ID algorithm, Eq. (2), in order to obtain the time sequences of the corresponding actuating torques realizing the given manipulator motion,  $\tilde{\tau}_j, j=1, 2, \dots, n$ . Next, for a specific  $k^{\text{th}}$  joint,  $k=1, 2, \dots, n$ , ID algorithm, Eq. (2), is used to calculate the time sequence of actuating torque  $\tilde{\tau}_{kZ}$  for the same trajectory of that joint  $q_{kZ}, \dot{q}_{kZ}, \ddot{q}_{kZ} = \tilde{q}_k, \dot{\tilde{q}}_k, \ddot{\tilde{q}}_k$ , but with the trajectories of the other joints that are equal to zero,  $q_{jZ}, \dot{q}_{jZ}, \ddot{q}_{jZ} = 0, j=1, 2, \dots, n, j \neq k$  i.e. as if there are no rotations of the other links about their corresponding axes.

If the comparison of the obtained torques  $\tilde{\tau}_k$  and  $\tilde{\tau}_{kZ}$  gives insignificant differences for the most demanding CMS motions, it can be concluded that motions of the other joints do not significantly contribute the required actuating torque for the joint  $k$ . Consequently, the effects of the nonlinear coupling terms in Eq. (2) for that particular joint may be reasonably treated as disturbances that can be easily overcome using a single joint feedback controller.

**1.2 Usage of aID Algorithm within a Selection of the CMS Drives**

When high accelerations are required within a manipulator system, minimizing the system inertia is necessary to satisfy the dynamic performance [26]. For this reason, the actuators of the CMS are herein chosen to operate very close to the maximum motor torque. Here, it is necessary to check whether the desired trajectories can be achieved, i.e., if the

required joint torques are less than or equal to the maximum motor torques. If the desired actuating torques exceed the maximum level for a very small value, a trajectory modification using an algorithm based on aID described in [1] is applied.

In aID, a discretization method in which the desired joint velocities  $\dot{q}_k$  for a specific interpolation period are calculated as functions of the programmed accelerations for that interpolation period as  $\dot{q}_k = \dot{q}_{k\text{prev}} + \ddot{q}_k \Delta t, k=1, 2, \dots, n$ , is used within calculations of the actuating joint torques  $\tau_k = \hat{m}_{zk}$ , Eq. (2). Hereinafter, the suffix "prev" indicates a value in the previous interpolation period. Subsequently, the following will be valid for the products  $\dot{q}_j \dot{q}_i$  within  $h_{kji}(\mathbf{q}) \dot{q}_j \dot{q}_i$  terms in Eq. (2):

$$\dot{q}_j \dot{q}_i = c_{ji} + a_i \ddot{q}_j + a_j \ddot{q}_i + \dot{q}_j \ddot{q}_i \Delta t^2, \tag{3}$$

with  $c_{ji} = \dot{q}_{j\text{prev}} \dot{q}_{i\text{prev}}, a_i = \dot{q}_{i\text{prev}} \Delta t, a_j = \dot{q}_{j\text{prev}} \Delta t$ . Given that the interpolation period of  $\Delta t = 5$  ms is used within the control unit, if the terms with  $\Delta t^2$  are neglected in Eq. (3), the error of  $\dot{q}_j \dot{q}_i \Delta t^2 = 2 \cdot 10^{-5} \dot{q}_j \dot{q}_i$  is made. In the consecutive section, it will be described how the motions of the links 2 and 3 have an insignificant effect on the motion of the CMS arm (link 1). For this reason, the CMS arm is excluded from the following calculations. After neglecting  $\Delta t^2$ , joint torques  $\tau_2 = \hat{m}_{z2}$  and  $\tau_3 = \hat{m}_{z3}$  are obtained from Eq. (2) for a specific interpolation period in the following approximate form:

$$\tau_2 = c_2 + c_{22} \ddot{q}_2 + c_{23} \ddot{q}_3, \tag{4}$$

$$\tau_3 = c_3 + c_{32} \ddot{q}_2 + c_{33} \ddot{q}_3. \tag{5}$$

Simulations for various CMS trajectories have shown that for  $\Delta t = 5$  ms, joint torques  $\tau_2$  and  $\tau_3$  given in Eqs. (4) and (5) differ by less than 1 % from the results obtained by a classical ID (without neglecting the terms with  $\Delta t^2$  in Eq. (2)). Coefficients  $c_2, c_{22}, c_{23}, c_3, c_{32}, c_{33}$  in Eqs. (4) and (5) are calculated for every interpolation period as functions of variables  $\ddot{q}_1, \dot{q}_{2\text{prev}}, \dot{q}_{3\text{prev}}, q_1, q_2, q_3$  and constants  $\Delta t$ , the centrifuge arm length  $a_r$ , components of the inertia matrices  $\hat{\mathbf{I}}_{2-4}$  of links  $k=2, 3, 4$  about the centre of mass of link  $k$  (here, index 4 indicates an external load, i.e., the pilot and the pilot's seat and equipment), components of  $\hat{\mathbf{r}}_{2-4}$  representing position vectors of the centre of mass of links 2 and 3 and an external load with respect to the origin of the frame attached to link  $k$ , and the masses of links 2 and 3, and the mass of an external load.

Next, the check and, if necessary, the limitation of the joint torques to the maximum values  $\tau_{2\text{max}}$  and  $\tau_{3\text{max}}$  achievable by the motors is performed in the

following manner: If it is determined that, for the given interpolation period, joint torque/s  $\tau_2$  and  $\tau_3$  exceed the maximum value/s, the maximum possible values of accelerations of  $\ddot{q}_2$  and  $\ddot{q}_3$  that the motors can achieve in this interpolation period are calculated by solving the system described in Eqs. (4) and (5) for the maximum values of the moments  $\tau_2$  and  $\tau_3$ :

$$\ddot{q}_{2\max} = \frac{(\tau_{2\max} - c_2)c_{33} - (\tau_{3\max} - c_3)c_{23}}{c_{22}c_{33} - c_{23}c_{32}}, \quad (6)$$

$$\ddot{q}_{3\max} = \frac{(\tau_{3\max} - c_3)c_{22} - (\tau_{2\max} - c_2)c_{32}}{c_{22}c_{33} - c_{23}c_{32}}. \quad (7)$$

New angular velocities and joint positions are then obtained from Eqs. (6) and (7) using a numerical integration. When this procedure is implemented, check if the modification of the end-effector trajectory is within the allowable limits needs to be performed. If it is, the same procedure can be used for the next lower power motor, such that the smallest actuator that meets the specified requirements is found. After completion of this procedure, the aID algorithm is regularly used within the trajectory planner.

The major benefit of the aID implementation is that modification of the trajectories of a specific joint are not only due to that actuator saturation, but also to the saturation of the other joints' actuators, such that they facilitate the other links' motions when the other actuators are saturated. The appropriate selection of actuators will ensure that modifications of the joint trajectories produce negligible changes in the obtained  $G$  load.

### 1.3 Design of the CMS Motion Controllers

In this study, a traditional decentralized single joint feedback control is compared with the dynamic model-based strategy for the CMS. To obtain realistic simulations that can provide relevant insight, a credible process model based on the effective inertia calculated from the ID is used. With structural natural frequencies and actuator capabilities taken into account, a realistic simulation of the controlled process is achieved.

#### 1.3.1 Model of Actuator's Mechanical Subsystem

The equation of motion for rigid body rotation about an axis is given in Eq. (8), [27]:

$$I\ddot{q} = \tau_M - \tau_L - B\dot{q}, \quad (8)$$

where  $q$  is a rotational position,  $I$  is the inertia of the moving parts,  $B$  is equivalent system friction coefficient,  $\tau_M$  represents the driving torque, and  $\tau_L$  is the load torque. If Eq. (8) is applied to the mechanical subsystem of a robot joint actuator,  $I$  depend on the instantaneous manipulator configuration,  $B$  is the nonlinear function of the rotor speed. Load torque  $\tau_L = \tau_{LD} + \tau_{LS}$  is of a twofold nature: predictable part  $\tau_{LD}$  caused by the motion of the chain of interconnected links which can be calculated from the manipulator dynamic model, and torque due to stochastic disturbances  $\tau_{LS}$ . Herein, it is assumed that there are no other predictable disturbances contributing to motor load torque. Following the nonlinear time-variant model of joint  $k$  actuator's mechanical subsystem is obtained:

$$I_{\text{eff}k}\ddot{q}_{mk} + B_{\text{eff}k}\dot{q}_{mk} = \tau_{Mk} - \tau_{Lk}. \quad (9)$$

Here,  $\dot{q}_{mk} = r_k \dot{q}_k$  is the angular speed of the actuator's rotor;  $r_k$  is the motor gear ratio;  $B_{\text{eff}k}$  is the equivalent (reflected) friction coefficient;  $I_{\text{eff}k}$  is the inertia reflected onto the rotor shaft, denoted here as the effective inertia; and  $\tau_{Mk}$  is the driving torque generated by the actuator of the  $k^{\text{th}}$  joint. Herein, the load torque  $\tau_{LDk}$  is calculated from ID model, Eq. (2), in the following manner [28]:

$$\tau_{LDk} = \frac{\tau_k - d_{kk}\ddot{q}_k}{r_k} = \frac{\sum_{j=1, j \neq k}^n d_{kj}(\mathbf{q})\ddot{q}_j + \sum_{j=1}^n \sum_{i=1}^n h_{kji}(\mathbf{q})\dot{q}_j\dot{q}_i + g_k(\mathbf{q})}{r_k}, \quad (10)$$

that is, joint torque  $\tau_k = \hat{m}_{zk}$  from Eq. (2) is reduced for the inertial term  $d_{kk}\ddot{q}_k$ . Adding a coefficient of  $\ddot{q}_k$  in ID, Eq. (2), to motor and gearbox inertia  $I_{mk}$ , the effective inertia for the joint  $k$  actuator is obtained as [28]:

$$I_{\text{eff}k} = (I_{mk} + d_{kk} / r_k^2). \quad (11)$$

If an accurate model for the friction experimentally obtained is available, the friction compensation can be introduced into the control. An alternative approach is to regard the bounded nonlinear friction terms as disturbances in traditional servo systems [29]. For the torque motors, chosen for the actuation of axes 2 and 3, the friction problem is of much less significance compared to motors with a gear reduction and can be regarded as negligible. With this approach, Eq. (9) becomes:

$$I_{\text{eff}k}\ddot{q}_{mk} = \tau_{Mk} - \tau_{Lk}. \quad (12)$$

### 1.3.2 Computed Torque Method

The computed torque method implies a feedforward cancelation of the nonlinear coupling terms in Eq. (2). Here, the load torque from the motion of the chain of interconnected links,  $\tau_{LDk}$ , obtained from ID, Eq. (10), is cancelled with a feedforward signal. The addition of feedback is beneficial for improving the reference-tracking capability of the control system given that modelling in practice is almost never error-free, and for suppressing the effects of stochastic disturbances. In Fig. 4, a block diagram of a single-input-single-output (SISO) system of the computed torque method with an added feedback controller is shown. After implementing the feedforward disturbance cancellation, the process model given in Eq. (12) becomes:

$$I_{\text{eff}k} \ddot{q}_{mk} = u_k - \tau_{LSk}, \quad (13)$$

where  $u_k$  is the torque proportional to the feedback controller output.

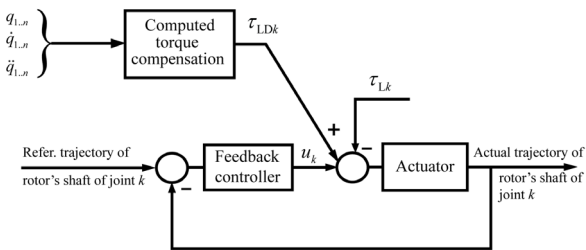


Fig. 4. Computed torque compensator with a feedback controller

### 1.3.3 Determination of Feedback Controller Gains for the Simulation Model

Given that the structural flexibilities in the system are not accounted for in the process modelling, to avoid exciting the unmodeled resonances, a rule of thumb is used when the lowest structural natural frequency  $\omega_{rk}$  of link  $k$  is at least two times bigger than the natural (undamped) frequency  $\omega_{nk}$  of the feedback controller for joint  $k$  [25]. To compare these frequencies, the PD position and proportional-integral (PI) velocity controllers are chosen, so that second-order closed-loop system with a characteristic polynomial  $s^2 + 2\zeta_k \omega_{nk} s + \omega_{nk}^2$  (where  $\zeta_k$  is the damping ratio) is obtained. Oscillations in the joint position or speed should be avoided.

Characteristic polynomials of the closed-loop system, where the rotor position  $q_{mk}$  and speed  $\dot{q}_{mk}$  are controlled using the PD and PI feedback, respectively, are given in the following forms:

$$s^2 + K_{DPk} s / I_{\text{eff}k} + K_{PPk} / I_{\text{eff}k}, \quad (14)$$

$$s^2 + K_{PSk} s / I_{\text{eff}k} + K_{ISk} / I_{\text{eff}k}, \quad (15)$$

where  $K_{PP}$ ,  $K_{DP}$ ,  $K_{PS}$ ,  $K_{IS}$  are the proportional and derivative, and proportional and integral, gains of the PD position and PI speed feedback, respectively.

A simple solution to overcome the problem of variable process control is to adopt a time-invariant model, tune the controller for the largest load, and accept the deteriorated performance under other operating conditions [30]. For the PD position control, Eq. (14), the effective inertia of a specific  $k^{\text{th}}$  joint actuator, Eq. (11), depends on the instantaneous manipulator configuration. For a fixed proportional gain  $K_{PPk}$ , the natural frequency of the closed-loop system in Eq. (14) varies, i.e.,  $\omega_{nk}(\mathbf{q}) = \sqrt{K_{PPk} / I_{\text{eff}k}(\mathbf{q})}$ . The maximum value of the natural frequency is obtained for the minimum value of the effective inertia. However, the damping ratio

$$\zeta_k = K_{DPk} / (2I_{\text{eff}k}(\mathbf{q})\omega_{nk}(\mathbf{q})) = K_{DPk} / (2\sqrt{I_{\text{eff}k}(\mathbf{q})K_{PPk}})$$

has the smallest value for the maximum value of the effective inertia  $I_{\text{eff}k\text{max}}$ , Eq. (11). Considering the request in which the motion of the link is never underdamped, if the value of  $\zeta_k$  for  $I_{\text{eff}k\text{max}}$  is 1 (critically damped response), in all configurations with smaller values of the effective inertia motions will be overdamped. In this way, fastest response without oscillations is obtained. For  $I_{\text{eff}k} = I_{\text{eff}k\text{max}}$ , the relation between the proportional gain  $K_{PPk}$ , Eq. (14), and natural frequency  $\omega_{nk}$  is as follows:

$$K_{PPk} = I_{\text{eff}k\text{max}} \omega_{nk}^2. \quad (16)$$

The maximum value of the allowed natural frequency  $\omega_{n\text{max}k} = \omega_{rk}/2$  is used for obtaining the maximum proportional gain in Eq. (16),  $K_{PPk\text{max}} = I_{\text{eff}k\text{max}} \omega_{rk}^2 / 4$ . When the proportional gain is chosen, and based on  $\zeta_k = 1$  for  $I_{\text{eff}k\text{max}}$ , the derivative gain follows from:

$$K_{DPk} = (2\sqrt{I_{\text{eff}k\text{max}}(\mathbf{q})K_{PPk}}), \quad (17)$$

and will have the maximum value for  $K_{PPk} = K_{PPk\text{max}}$ . The same analysis stands for the PI speed feedback controller in Eq. (15), where  $K_{IS}$  corresponds to  $K_{PP}$  in Eq. (16), and  $K_{PS}$  is obtained in the same way as  $K_{DP}$  in Eq. (17).

When the gains of the PD position/PI speed controller are chosen based on the structural resonance features, as described previously, to achieve a realistic simulation, the actuator capabilities, i.e., the maximum actuator torques, should be taken into account. Here, a model is adopted in which the maximum torque/

torque increment generated by an actuator based on the output of the feedback controller corresponds to the assumed maximum (allowed) controlled variable error. The corresponding gain should be applied to the output of the feedback controller within the simulation model.

Determination of the gain value that will provide a realistic simulation is based on the following model. The difference equation describing the actuator torque generated from the output of the PD position controller is [27]:

$$K_{pp}\Delta q(i) + K_{dp}(\Delta q(i) - \Delta q(i-1)) = \frac{\tau_M(i)}{K_{TORP}}, \quad (18)$$

where  $\Delta q(i)$  is the positional error at sampling instant  $i$  and  $\tau_M(i)$  is the torque generated by the actuator.

Likewise, in the case of a PI speed controller, the difference equation representing the torque increment  $\Delta\tau_M(i)$  generated by the actuator as a function of the speed error at sampling instant  $i$  is [27]:

$$K_{is}\Delta\dot{q}(i) + K_{ps}(\Delta\dot{q}(i) - \Delta\dot{q}(i-1)) = \frac{\Delta\tau_M(i)}{K_{TORS}}, \quad (19)$$

where  $\Delta\dot{q}(i)$  is the speed error at the  $i^{\text{th}}$  sampling instant.

Scaling factors  $K_{TORP}$  and  $K_{TORS}$ , calculated from Eq. (18) and Eq. (19) for the maximum torque/torque increment, assumed maximum allowed controlled variable error, and feedback gains defined by Eqs. (16) and (17), provide values of the amplifier gains applied to the output of the feedback controllers in the presented simulation model. The maximum allowed position and speed errors should be chosen such that they are within the range of expected errors, in order to obtain gains  $K_{TORP}$  and  $K_{TORS}$  that would provide a realistic simulation to be obtained.

## 2 RESULTS AND DISCUSSION

### 2.1 Simulation of Dynamics Effects of Interconnected CMS Links' Motions

A method for the assessment of the mutual dynamic effects of the interconnected links' motions, given in Section 1.1, is applied for the CMS. In Fig. 5, joint actuating torque for the first axis  $\tau_1$  obtained by the ID, Eq. (2), for the joint trajectories given in Fig. 3, is compared with the joint actuating torque  $\tau_{1Z}$  obtained by the ID, Eq. (2), for the same trajectory of axis 1, but with the trajectories of the other joints equalling zero ( $q_2=q_3=0$ ,  $\dot{q}_2=\dot{q}_3=0$ ,  $\ddot{q}_2=\ddot{q}_3=0$ ). The difference is practically negligible. This indicates the insignificant influence of the motions of links 2 and 3

to the CMS arm motion, which is even more reduced due to the use of a gear reduction between the actuator and the link 1, as shown in Eq. (10). In the same way, simulations showed a large influence of the motion of the first axis on the actuating torques of links 2 and 3 owing to the large centrifugal and tangential acceleration forces produced by the CMS arm. In addition, significant mutual influence of the motions of links 2 and 3 was determined through their mutual contribution within actuating torques  $\tau_2$  and  $\tau_3$ . Consequently, the following implementation of the control system is proposed: The first axis is controlled using feedback only, whereas a centralized control strategy is considered for the second and third axes. The latter is described later in this paper.

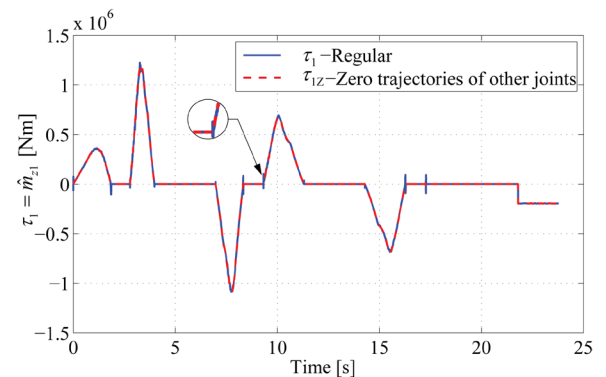


Fig. 5. The contribution of motions of second and third axes to the value of torque  $\tau_1$

### 2.2 Choice of actuators based on aID algorithm simulations

The approximate ID algorithm described in Section 1.2 was tested for the chosen actuators. Massive simulations showed that modifications of the joint trajectories do not significantly influence the end-effector trajectories for a given choice of actuators with  $\tau_{2,3\max}=2 \cdot M_{2,3\max}=21800$  Nm. In Fig. 6, the commanded acceleration at the centre of the gondola given by one of the most demanding application programs, and the same acceleration obtained as the output of the aID with the chosen actuators, are both given. Technical data and characteristics given in the manufacturer's configuration manual [24] indicate that the end-effector trajectory (absolute acceleration in the gondola centre) obtained after applying aID will significantly differ from the desired trajectory if a successively smaller motor is used. In this way, an actuator with the smallest weight and power with the potential to achieve the required joint motions is obtained.

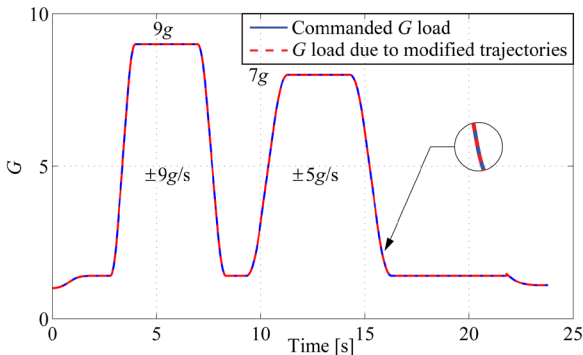


Fig. 6. Desired and modified absolute acceleration profiles

### 2.3 Comparison of Motion Controller Performances for Axes 2 and 3

A dynamic model-based control method that comprises feedback and feedforward computed torque compensation is considered for axes 2 and 3 in this study. Several Simulink models were designed to simulate and compare the controller performances for axes 2 and 3 achieved by position feedback, velocity feedback, and computed torque (CT) method with the same feedback controllers added. The reference position or speed in the Simulink models is given as a series of discrete values obtained from the trajectory planner given in Fig. 3 after an aID-based check of the trajectories is applied. The interpolation period  $\Delta t$  is 5 ms. The effective inertia is calculated for every interpolation period for links 2 and 3, as given in Eq. (11). Coefficients  $d_{22}$  and  $d_{33}$  are calculated using ID, Eq. (2), as the sum of the acceleration coefficients of  $\ddot{q}_2$  and  $\ddot{q}_3$ , respectively. The moment of inertia of the motors is  $I_{m2}=I_{m3}=1092 \cdot 10^{-2}$  kgm<sup>2</sup>. For the trajectories given in Fig. 3,  $I_{\text{eff}2\text{max}}=2221.3$  kgm<sup>2</sup> is obtained, relative to which the effective inertia varies up to 6.37 %, and  $I_{\text{eff}3\text{max}}=508.75$  kgm<sup>2</sup> is obtained with the same variations of up to 15.47 %.

From CATIA,  $\omega_{r2}=40.843$  Hz is obtained as the lowest structural natural frequency of the CMS ring, whereas  $\omega_{r3}=13.851$  Hz is the lowest natural frequency of the gondola.

Linear time-invariant (LTI) models of the process given in Eq. (12) with a maximal value of the effective inertia, Eq. (11), for the trajectories given in

Fig. 3 are adopted. Gains  $K_{PPk}/K_{ISk}$  and  $K_{DPk}/K_{PSk}$  are chosen as the maximum gains given by Eqs. (16) and (17), respectively. Gains  $K_{TORPk}$  and  $K_{TORSk}$  obtained from Eqs. (18) and (19) are applied at the outputs of the feedback controllers. In Table 1, the process and feedback controller parameters for joints  $k=2,3$  are given.

In models with feedback only, a disturbance is simulated as  $\tau_{Lk}=\tau_{LDk}$ ,  $k=2,3$ , obtained from ID, Eq. (10). In CT plus feedback control models, the load torques  $\tau_{LDk}$ ,  $k=2,3$ , calculated from, Eq. (10), are compensated for during every interpolation period, whereas the total load torque  $\tau_{Lk}$ ,  $k=2,3$  is simulated as  $\tau_{Lk}=\tau_{LDk}(1+A\sin\omega_D t)$   $k=2,3$ . The term  $\tau_{LDk}A\sin\omega_D t$  simulates the stochastic disturbances and uncertainties (errors in the estimates of the load torque,  $\tau_{LDk}$ ). Here,  $t$  indicates the time, whereas the values  $A$  and  $\omega_D$  are the amplitude and frequency of the disturbances. It should be noted that in the applied simulation models the torque limitation based on the model given in Eqs. (18) and (19) is included, the saturation of the torque generated from the output of the feedback controller is applied, as well as the saturation of the sum of the torques from the feedback and feedforward signals. Herein, the CT load torque compensation is effective only when the torque generated by the actuator due to feedback controller does not exceed the maximum actuator torque.

In Fig. 7, the position tracking of joints 2 and 3 is given as follows: a) joint 2, PD feedback controller, b) joint 3, PI feedback controller, c) joint 2, PD feedback controller together with the feedforward computed torque method, and d) joint 3, PI feedback controller together with feedforward computed torque method. Tracking errors are also given in Fig. 7 in e) for joint 2, and in f) for joint 3. In these simulations,  $A=0.05$  (which suggests that the load torque estimation error is about 5 %), and  $\omega_D=100$ .

The addition of feedforward cancelation of the nonlinear coupling terms in the dynamic model, Eq. (2), to the feedback controller achieves a considerable improvement in position tracking for joint 2. For joint 3, improvement in position tracking is noticeable, but insignificant, considering the size of the tracking error. To decrease the error in position for link 3, a bigger torque actuator should be used. With the achieved

Table 1. Process and controller parameters for joints  $k = 2, 3$  for the trajectories given in Fig. 3

Joint	$I_{\text{eff}k\text{max}}$ [kgm <sup>2</sup> ]	$K_{PPk}$	$K_{DPk}$	$K_{ISk}$	$K_{PSk}$	$K_{TORPk}$	$K_{TORSk}$	$\Delta q_{k\text{max}}$ [rad]	$\Delta \dot{q}_{k\text{max}}$ [rad/s]
$k=2$	2221.3	$3.65 \times 10^7$	$5.7 \times 10^5$	$3.65 \times 10^7$	$5.7 \times 10^5$	0.115	0.115	$5 \times 10^{-3}$	$5 \times 10^{-3}$
$k=3$	508.75	$9.63 \times 10^5$	$4.43 \times 10^4$	$9.63 \times 10^5$	$4.43 \times 10^4$	4.14	4.14	$5 \times 10^{-3}$	$5 \times 10^{-3}$

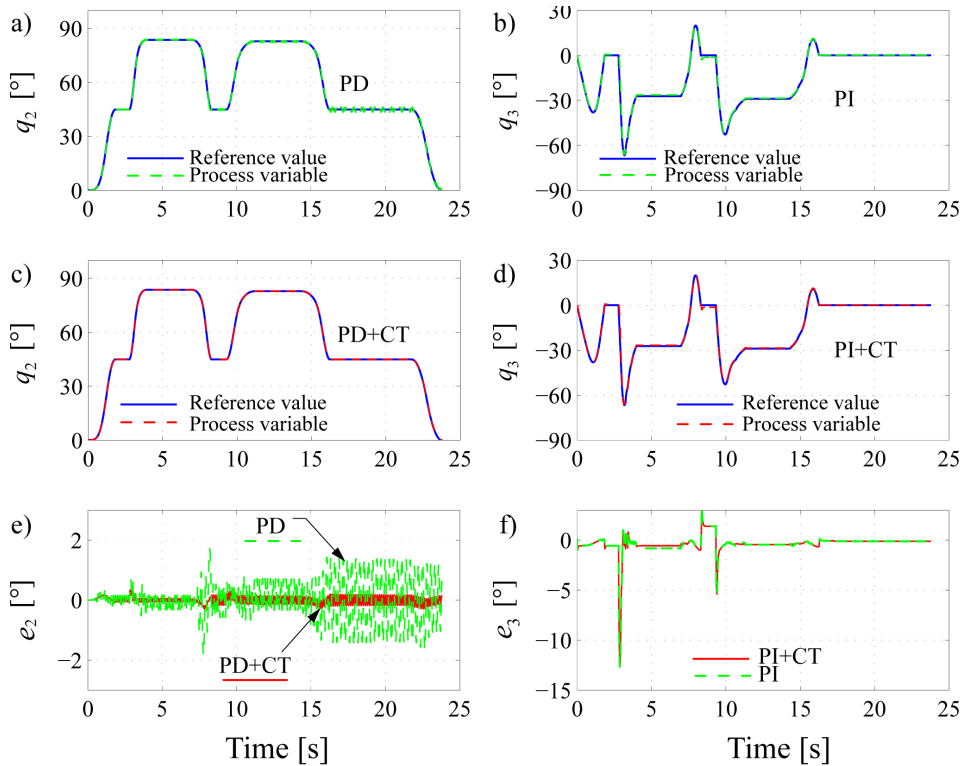


**Fig. 7.** Position tracking of a) joint 2, PD feedback controller (dashed/green); b) joint 3, PI feedback controller (dashed/green); c) joint 2, PD feedback plus CT (dashed/red); d) joint 3, PI feedback plus CT (dashed/red); e) joint 2, position error with PD feedback (dashed/green) and PD feedback controller plus CT (solid/red); f) joint 3, position error with PI feedback controller (dashed/green) and PI feedback controller plus CT (solid/red)

tracking, the maximum absolute error in the absolute acceleration at the centre of the gondola is 0.47 g.

### 3 CONCLUSIONS

The analysis described in this paper highlights the benefits of a dynamic model-based control system design for a CMS, which is a manipulator characterized by highly challenging motions. Based on appropriate inverse dynamics model simulations, a suitable choice of the control system and actuators, considering a satisfactory performance as well as the complexity and cost of the overall system, can be achieved. The use of an algorithm based on the approximate inverse dynamics model enables a compromise to be made between the power and weight of the chosen actuators. Realistic simulations of the controlled process for the ring and gondola axes, which account for structural natural frequencies, actuator torque limits, and inertia reflected on the rotor shafts, were conducted, enabling a comparison between the standard decentralized feedback control and a dynamic model-based control strategy consisting of a computed torque method with

the addition of feedback. Simulations demonstrated the significant benefits in position tracking with disturbance cancelation achieved using a computed torque method added to the feedback when an actuator that is able to achieve the required motion is applied. Future work will be focused on implementing the method presented in this paper to other systems. Furthermore, alternative centralized control methods will be considered.

### 4 ACKNOWLEDGEMENTS

This research has been supported by a research grant of the Serbian Ministry of Education, Science and Technological Development under numbers TR 35023 and TR 35006.

### 5 REFERENCES

[1] Kvrđić, V.M., Vidaković, J.Z., Lutovac, M.M., Ferenc, G.Z., Cvijanović, V.B. (2014). A control algorithm for a centrifuge motion simulator. *Robotics and Computer-Integrated*

- Manufacturing*, vol. 30, no. 4, p. 399-412, DOI:10.1016/j.rcim.2014.01.002.
- [2] Albery, W.B. (2004). Acceleration in other axes affects +Gz tolerance: dynamic centrifuge simulation of agile flight. *Aviation, Space, and Environmental Medicine*, vol. 75, no. 1, p. 1-6.
- [3] Hartenberg, R.S., Denavit, J. (1964). *Kinematic Synthesis of Linkages*. McGraw-Hill, New York.
- [4] Slotine, J.-J.E., Li, W. (1987). On the adaptive control of robot manipulators. *The International Journal of Robotics Research*, vol. 6, no. 3, p. 49-59, DOI:10.1177/027836498700600303.
- [5] Wang, H. (2017). Adaptive control of robot manipulators with uncertain kinematics and dynamics. *IEEE Transactions on Automatic Control*, vol. 62, no. 2, p. 948-954, DOI:10.1109/TAC.2016.2575827.
- [6] Ferrara, A., Incremona, G.P. (2015). Design of an integral suboptimal second-order sliding mode controller for the robust motion control of robot manipulators. *IEEE Transactions on Control Systems Technology*, vol. 23, no. 6, p. 2316-2325, DOI:10.1109/TCST.2015.2420624.
- [7] Chen, C.-S. (2008). Dynamic structure neural-fuzzy networks for robust adaptive control of robot manipulators. *IEEE Transactions on Industrial Electronics*, vol. 55, no. 9, p. 3402-3414, DOI:10.1109/TIE.2008.926778.
- [8] Jerbic, B., Nikolic, G., Chudy, D., Svaco, M., Sekoranja, B. (2015). Robotic application in neurosurgery using intelligent visual and haptic interaction. *International Journal of Simulation Modelling*, vol. 14, no. 1, p. 71-84, DOI:10.2507/IJSIMM14(1)7.290.
- [9] Li, X., Cheah, C.C. (2014). Adaptive neural network control of robot based on a unified objective bound. *IEEE Transactions on Control Systems Technology*, vol. 22, no. 3, p. 1032-1043, DOI:10.1109/TCST.2013.2293498.
- [10] Erkaya, S. (2018). Effects of joint clearance on motion accuracy of robotic manipulators. *Strojniški vestnik - Journal of Mechanical Engineering*, vol. 64, no. 2, p. 82-94, DOI:10.5545/sv-jme.2017.4534.
- [11] Klobučar, R., Čas, J., Šafarič, R., Brezočnik, M. (2008). Uncalibrated visual servo control with neural network. *Strojniški vestnik - Journal of Mechanical Engineering*, vol. 54, no. 9, p. 619-627.
- [12] Peng, J., Liu, Y., Wang, J. (2014). Fuzzy adaptive output feedback control for robotic systems based on fuzzy adaptive observer. *Nonlinear Dynamics*, vol. 78, no. 2, p. 789-801, DOI:10.1007/s11071-014-1477-z.
- [13] Das, M.T., Dulger, L.C., Das, G.S. (2013). Robotic applications with particle swarm optimization (PSO). *IEEE International Conference on Control, Decision and Information Technologies*, p. 160-165, DOI:10.1109/CoDIT.2013.6689537.
- [14] Hrelja, M., Klancnik, S., Irgolic, T., Paulic, M., Jurkovic, Z., Balic, J., Brezocnik, M. (2014). Particle swarm optimization approach for modelling a turning process. *Advances in Production Engineering & Management*, vol. 9, no. 1, p. 21-30, DOI:10.14743/apem2014.1.173.
- [15] Mei, J., Zang, J., Ding, Y., Xie, S., Zhang, X. (2017). Rapid and automatic zero-offset calibration of a 2-DOF parallel robot based on a new measuring mechanism. *Strojniški vestnik - Journal of Mechanical Engineering*, vol. 63, no. 12, p. 715-724, DOI:10.5545/sv-jme.2017.4529.
- [16] Chung, W.K., Fu, L.-C., Hsu, S.-H. (2008). Motion control. Siciliano, B., Khatib, O. (eds.). *Springer Handbook of Robotics*. Springer-Verlag, Berlin Heidelberg, p. 133-160, DOI:10.1007/978-3-540-30301-5\_7.
- [17] Sciavicco, L., Siciliano, B., Villani, L., Oriolo, G. (2012). Robotics-Modelling, Planning and Control. *Advanced Textbooks in Control and Signal Processing Series*. Springer-Verlag London, London, DOI:10.1007/978-1-84628-642-1.
- [18] Schumann, J., Gupta, P., Liu, Y. (2010). Application of neural networks in high assurance systems: A survey. Schumann, J., Liu, Y. (eds). *Applications of Neural Networks in High Assurance Systems. Studies in Computational Intelligence*, vol. 268, Springer-Verlag, Berlin Heidelberg, DOI:10.1007/978-3-642-10690-3\_1.
- [19] Tsai, M.-H., Shih, M.-C. (2009). G-load tracking control of a centrifuge driven by servo hydraulic systems. *Proceedings of the Institution of Mechanical Engineers, Part G: Journal of Aerospace Engineering*, vol. 223, no. 6, p. 669-682, DOI:10.1243/09544100JAER0519.
- [20] Chen, Y.C., Repperger, D.W. (1996). A study of the kinematics, dynamics and control algorithms for a centrifuge motion simulator. *Mechatronics*, vol. 6, no. 7, p. 829-852, DOI:10.1016/0957-4158(96)00018-9.
- [21] Markiewicz, B.R. (1973). *Analysis of the Computed Torque Drive Method and Comparison with Conventional Position Servo for a Computer-Controlled Manipulator* (NASA Technical Memorandum 33-601), California Institute of Technology, Pasadena.
- [22] Lutovac, M., Ferenc, G., Kvrđić, V., Vidaković, J., Dimić, Z. (2012). Robot programming system based on LIRL programming language. *Acta Technica Corviniensis-Bulletin of Engineering*, vol. 5, no. 2, p. 27.
- [23] Vidakovic, J., Lazarevic, M., Kvrđić, V., Dančuo Z., Lutovac, M. (2013). Comparison of numerical simulation models for open loop flight simulations in the human centrifuge. *PAMM*, vol. 13, no. 1, p. 485-486, DOI:10.1002/pamm.201310235.
- [24] *SINAMICS Configuration Manual: 1FW6 Built-In Torque Motors* (2009). Siemens Support, Erlangen.
- [25] Craig, J.J. (2005). *Introduction to Robotics: Mechanics and Control* (3<sup>rd</sup> ed.). Pearson Prentice Hall, Upper Saddle River.
- [26] Scheinman, V., McCarthy, J.M. (2008). Mechanisms and actuation. Siciliano, B., Khatib, O. (eds.). *Springer Handbook of Robotics*. Springer-Verlag, Berlin Heidelberg, p. 67-86, DOI:10.1007/978-3-540-30301-5\_4.
- [27] Vukosavic, S. (2007). *Digital Control of Electrical Drives*. Springer-Verlag US, New York, DOI:10.1007/978-0-387-48598-0.
- [28] Spong, M.W., Hutchinson, S., Vidyasagar, M. (2006). *Robot dynamics and control*. John Wiley & Sons, Hoboken.
- [29] Lee, H.S., Tomizuka, M. (1996). Robust motion controller design for high-accuracy positioning systems. *IEEE Transaction on Industrial Electronics*, vol. 43, no. 1, p. 48-55, DOI:10.1109/41.481407.
- [30] Åström, K., Hägglund, T. (1995). *PID Controllers: Theory, Design, and Tuning*, (2<sup>nd</sup> ed.) Isa, Research Triangle Park NC.

# A Weighted Gradient Projection Method for Inverse Kinematics of Redundant Manipulators Considering Multiple Performance Criteria

Jun Wan<sup>1,\*</sup> – Jiafeng Yao<sup>1</sup> – Liang'an Zhang<sup>2</sup> – Hongtao Wu<sup>1</sup>

<sup>1</sup> Nanjing University of Aeronautics & Astronautics, College of Mechanical and Electrical Engineering, China

<sup>2</sup> Anhui University of Technology, Department of Mechanical Engineering, China

*Among the many methods of solving inverse kinematics (IK) of redundant manipulators, the classic weighted least-norm (WLN) method is often introduced to avoid joint position limits effectively but cannot be extended to restrict other constraints. Another general technique uses the fashioned gradient projection method (GPM) that ensures successes of the main task and the constraints-based subtasks but suffers with regard to the proper selections for the coefficients of performance criteria. Inspired by the merits of WLN and GPM, a weighted gradient projection method (WGPM) is proposed in this paper to resolve IK problems of redundant manipulators with multiple performance criteria. In this approach, its structure is formulated as a hierarchical task-level regulation, where the highest priority is to accomplish the main task higher than the avoidance of joint position limits, and the priorities of other subtasks of the performance criteria are dependent on the clamping weighted matrix in descending order. Moreover, to avoid the defect of selecting scalar factors for different criteria by trial and error in GPM, a technique of determining proper scalar coefficients is presented by means of normalizing corresponding performance functions in WGPM. Using a 7 degree-of-freedom (DOF) redundant manipulator, simulations and experiments are conducted to demonstrate the validity of the proposed WGPM method by comparing it with the results of the traditional WLN and GPM methods, respectively.*

**Keywords:** inverse kinematics, multiple performance criteria, redundant manipulator, scalar coefficient, weighted gradient projection method

## Highlights

- Multiple performance criteria are taken into account in resolving IK problems of redundant manipulators.
- The hierarchical method can guarantee implementations of the main task and the subtasks.
- A scalar coefficient of performance criterion is adjusted on-line by the normalization method.
- The obtained results prove the effectiveness of the proposed WGPM method.

## 0 INTRODUCTION

Generally, a kinematically redundant manipulator has more DOFs than those required in performing a given task, which can exploit the redundancy to achieve second goals with little influence on the end-effector (EE). At present, the redundant manipulators have attracted considerable interest and been increasingly applied to modern productions and civilian fields.

To solve the inverse kinematics (IK) problem of a robotic manipulator is to obtain a set of actuated joint values to move the manipulator to a desired position and orientation in Cartesian space [1], and is a common basis of dynamic analysis and control system design [2]. Due to the residual redundancy, however, the underdetermined Jacobian matrix of a redundant manipulator admits infinite joint positions corresponding to a given posture of EE. Therefore, the problem of kinematic redundancy resolution becomes the basic and prerequisite issue [3] and [4]. To this end, multiple control strategies have been obtained to the IK resolution as the redundant manipulator has more

degrees-of-freedom (DOFs) over several decades, such as the pseudo-inverse (PI) method, the extended Jacobian matrix (EJM) method, and geometric methods for special structures, apart from the weighted least-norm (WLN) and the gradient projection method (GPM) [5] and [6]. Note that the WLN method and the GPM method are the most frequently used ones, but both methods are seriously flawed. In WLN, the major limitation is that it can only be used to constrain joint position limits effectively and dampen joint motion to exceed the limit without backing away from it. Meanwhile, the scalar factor in GPM for the performance criterion is often selected empirically, which may incur the poor performance of subtasks. Furthermore, a novel solution [7] and [8] to the kinematic analysis of a single-loop reconfigurable 7R (R: revolute joints) mechanism is given based on the algorithm of IK about a general serial 6R manipulator but neglects the advantages of redundancy in the 7R manipulator.

On account of the hierarchical control structure applied by GPM considering multiple constraints-

\*Corr. Author's Address: College of Mech. and Electrical Engineering, Nanjing University of Aeronautics & Astronautics, 210016, Nanjing, China, junwanrob@gmail.com

based performance criteria, excellent works have been conducted to avoid or alleviate the difficulty of inaccurate coefficients for performance criteria. A nested GPM [9] and [10] is used to provide fixed scalar weighted value for each performance criterion intuitively. Owing to the lack of adaptability to the changing situations using the fixed weighted values, a redundancy-based approach [11] is presented for GPM to eliminate the negative effect by iteratively solving a system of linear equations. Another way is an improved coefficient matrix [12] to calculate the coefficients of criteria by the magnitudes of the least-norm solution and the homogeneous solution of GPM. Moreover, a motion optimization measure [13] is designed to adjust self-motion coefficients in real time of multiple performance criteria for optimizing redundant robot trajectories using GPM. Additionally, to satisfy joint position limits as a performance criterion effectively, an extended vision of GPM [6] is proposed that refers to the principles of WLN and GPM.

However, the existing techniques still do not perfectly solve the problem of rational coefficients determinations for performance criteria in the original GPM method. They identify these coefficients by using extensive simulations inefficiently and/or increase the computation burden in algorithm unconsciously. Therefore, the self-adjusting coefficients of constraints-based performance criteria are the prerequisite for redundant robot manipulation using the GPM method with high efficiency.

Motivated by the availability of avoiding joint position limits of the WLN method and the extensibility of constraining multiple criteria of the GPM method, a novel GPM method, WGPM, is proposed in this paper to resolve IK problems of redundant manipulators considering multiple performance criteria. Novelties and specific contributions in this work are that in order to eliminate the limitation of the WLN method, a clamping weighted matrix and a repulsive potential field are introduced to force joints back away from joint position limits while not only blocking them at limits. In terms of selecting proper scalar factors for different performance criteria in the proposed weighted gradient projection method (WGPM), a technique of determining continuous scalar coefficients is presented based on respective normalizations of criteria but not on empiricism, which can maintain the performances of subtasks in the WGPM method. In order to regulate the subtasks and avoid conflicts between them, a hierarchy-based resolution on the proposed WGPM method is

presented in which priorities of performance criteria are organized in descending order.

This paper is outlined as follows: Section 1 briefly reviews IK formulations of redundant manipulators, and the WGPM method is proposed in Section 2. To verify and assess the proposed method, results and discussion of simulations and experiments are performed compared to the WLN method and the GPM method, respectively, in Section 3. Finally, the conclusive remarks are shown in Section 4.

## 1 PROBLEM FORMULATION

In kinematic control,  $\dot{\mathbf{x}} \in \mathbf{R}^m$  denotes the main task velocity of a manipulator, and  $\dot{\boldsymbol{\theta}} \in \mathbf{R}^n$  denotes the corresponding joint velocities. The relation between them is expressed as follows:

$$\dot{\mathbf{x}} = \mathbf{J}(\boldsymbol{\theta})\dot{\boldsymbol{\theta}}, \quad (1)$$

where  $\mathbf{J}(\boldsymbol{\theta}) \in \mathbf{R}^{m \times n}$  is the Jacobian matrix. For redundant manipulators, if  $\text{rank}(\mathbf{J})$  keeps constant as  $m$  and  $m < n$ ,  $\mathbf{J}$  becomes an underdetermined one, and the resolution of Eq. (1) is infinite corresponding to a given task velocity.

By using the PI method, the joint velocity  $\dot{\boldsymbol{\theta}}$  can have a least-norm solution

$$\dot{\boldsymbol{\theta}} = \mathbf{J}^+ \dot{\mathbf{x}}, \quad (2)$$

where  $\mathbf{J}^+$  denotes the Moore-Penrose inverse of  $\mathbf{J}$ ,  $\mathbf{J}^+ = \mathbf{J}^T (\mathbf{J}\mathbf{J}^T)^{-1}$ . Obviously, the PI method does not exhaust redundancy to perform optimization research for subtasks.

The IK solution, however, cannot always be derived in a straightforward manner as Eq. (2) due to an inherent singularity problem [14]. In order to handle singularities, the IK solution of a redundant manipulator in singular configurations is achieved by utilizing the damped least-squares (DLS) method [15], which has a compromised product between the accuracy of main task motion and the continuities of joint velocities. The DLS method is formally given as:

$$\mathbf{J}^T \dot{\mathbf{x}} = (\mathbf{J}^T \mathbf{J} + \rho^2 \mathbf{I}_n) \dot{\boldsymbol{\theta}}, \quad (3)$$

where  $\mathbf{I}_n \in \mathbf{R}^n$  is an identity matrix, and  $\rho \geq 0$  is the damping factor. A small value of  $\rho$  leads to accurate solutions but low robustness to occurrences of singular and near-singular configurations of the manipulator and vice versa.  $\rho$  is usually determined by the following equation:

$$\rho^2 = \max \left\{ 0, \rho_{\max}^2 \left( 1 - \left( \frac{\sigma_{\min}}{\varepsilon} \right)^2 \right) \right\} \geq 0, \quad (4)$$

where  $\rho_{\max}$  is at the user's disposal to suitably shape the solution in the neighbourhood of a singularity.  $\varepsilon$  is the size of the singular region.  $\sigma_{\min}$  is the minimum of singularity values from the singular value decomposition (SVD) technique on  $\mathbf{J}$ .

Performance criteria play an important role in control that determines the application potential of redundant manipulators [16] and improves kinematics and dynamics performance [17]. Following the consideration, therefore, the motion of the subtask should be appropriately selected based on the criterion with the primary task unaffected, which can be described by GPM:

$$\dot{\theta} = \mathbf{J}^+ \dot{x} + k\mathbf{P}\nabla\mathbf{H}(\theta). \quad (5)$$

The first item on the right of Eq. (5) is the least-norm solution for the primary task, and the second item is the homogeneous solution for self-motion that is orthogonal to the former in the null space  $\mathbf{P} = \mathbf{I}_n - \mathbf{J}^+ \mathbf{J}$ .  $\nabla\mathbf{H}(\theta)$  is the gradient vector of performance criterion  $\mathbf{H}(\theta)$  as a subtask, which is expressed as:

$$\nabla\mathbf{H}(\theta) = \left[ \frac{\partial H(\theta)}{\partial \theta_1}, \frac{\partial H(\theta)}{\partial \theta_2}, \dots, \frac{\partial H(\theta)}{\partial \theta_n} \right]^T. \quad (6)$$

$k$  is the scalar coefficient. It should be taken positive if  $\nabla\mathbf{H}(\theta)$  is to be maximized, and negative if  $\nabla\mathbf{H}(\theta)$  is to be minimized. As noted in the previous section, choosing a satisfactory coefficient is non-trivial. If  $k$  is too small, the capability for avoiding the constraint is weakened. If  $k$  is too large, violating the constraint and causing oscillation during execution is probable.

As an alternative, the WLN method is expressed as follows:

$$\mathbf{J}_w = \mathbf{J}\mathbf{W}^{-\frac{1}{2}}, \quad (7)$$

$$\dot{\theta}_w = \mathbf{W}^{\frac{1}{2}} \dot{\theta}, \quad (8)$$

$$\dot{\theta} = \mathbf{W}^{-\frac{1}{2}} \mathbf{J}_w^+ \dot{x} = \mathbf{W}^{-1} \mathbf{J}^T (\mathbf{J}\mathbf{W}^{-1} \mathbf{J}^T)^{-1} \dot{x}, \quad (9)$$

where  $\mathbf{J}_w$  and  $\dot{\theta}_w$  are defined as the weighted Jacobian matrix and the weighted joint velocity, respectively.  $\mathbf{W} \in \mathbf{R}^{n \times n}$  is the positive and diagonal weighted matrix, and its  $i$ th diagonal element is defined by:

$$w_i = \begin{cases} 1 + \left| \frac{\partial H(\theta)}{\partial \theta_i} \right| & \Delta \left| \frac{\partial H(\theta)}{\partial \theta_i} \right| \geq 0 \\ 1 & \text{else} \end{cases}, \quad (10)$$

where  $\Delta \left| \frac{\partial H(\theta)}{\partial \theta_i} \right|$  is the change rate of  $\left| \frac{\partial H(\theta)}{\partial \theta_i} \right|$  [18].

The WLN method is proposed to only keep joint motion inside a physical range based on a performance criterion:

$$H(\theta) = \sum_{i=1}^n \frac{(\theta_{i\max} - \theta_{i\min})^2}{4(\theta_{i\max} - \theta_i)(\theta_i - \theta_{i\min})}, \quad (11)$$

where  $\theta_{i\max}$  and  $\theta_{i\min}$  are the upper and lower limits of the joint position  $\theta_i$ .

In Fig. 1, when  $\theta_i$  is gradually close to the neighbouring positive or negative limit,  $\left| \frac{\partial H(\theta)}{\partial \theta_i} \right| \rightarrow \infty$ , this is,  $w_i \rightarrow \infty$ . Therefore from Eq. (9),  $\dot{\theta}_i$  is repressed to zero, and the  $i$ th joint motion is stopped at limit and has no competence to withdraw the joint from its limit.

Both GPM and WLN are possible to risk singularities when the manipulator configuration is ill-conditioned. Combining the DLS method defined in Eq. (3), GPM could be rewritten as:

$$\dot{\theta} = \mathbf{J}_a^+ \dot{x} + k(\mathbf{I}_n - \mathbf{J}_a^+ \mathbf{J}) \nabla\mathbf{H}(\theta), \quad (12)$$

$$\mathbf{J}_a^+ = \mathbf{J}^T (\mathbf{J}\mathbf{J}^T + \rho^2 \mathbf{I}_m)^{-1}. \quad (13)$$

WLN could be redefined by:

$$\dot{\theta} = \mathbf{W}^{-1} \mathbf{J}^T (\mathbf{J}\mathbf{W}^{-1} \mathbf{J}^T + \rho^2 \mathbf{I}_m)^{-1} \dot{x}, \quad (14)$$

where  $\mathbf{I}_m \in \mathbf{R}^m$  is an identity matrix.

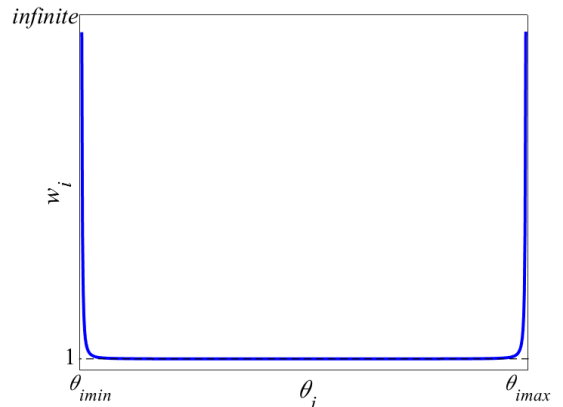


Fig. 1. Weighted value for the  $i$ th joint position in WLN

## 2 FORMULATION OF WGPM

### 2.1 Progressive Clamping Weighted Matrix

We add an activation buffer, i.e., a band of width  $\Omega$ , before a joint position limit, so that a whole joint motion interval is divided into three parts, as depicted in Fig. 2.

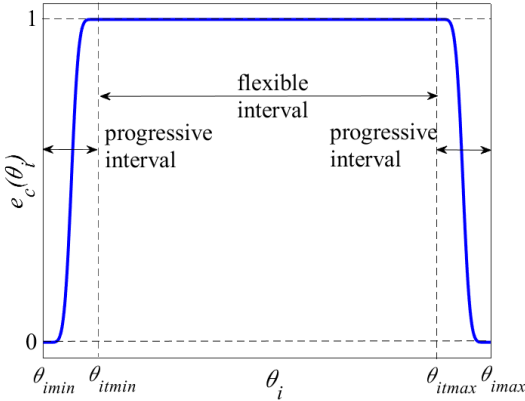


Fig. 2. Weighted value for the  $i$ th joint position in WGPM

Hence, a progressive clamping weighted matrix is defined by:

$$\mathbf{E}_c = \text{diag}(e_c(\theta_i)), \quad i = 1, 2, \dots, n, \quad (15)$$

where the element  $e_c(\theta_i)$  is governed by:

$$e_c(\theta_i) = \begin{cases} g_\Omega\left(\frac{\theta_{itmin} - \theta_i}{\theta_{itmin} - \theta_{imin}}\right) & \theta_{imin} \leq \theta_i \leq \theta_{itmin} \\ 1 & \theta_{itmin} < \theta_i < \theta_{itmax} \\ g_\Omega\left(\frac{\theta_i - \theta_{itmax}}{\theta_{itmax} - \theta_{imax}}\right) & \theta_{itmax} \leq \theta_i \leq \theta_{imax} \end{cases}, \quad (16)$$

where  $\theta_{itmax}$ ,  $\theta_{itmin}$  are the upper and lower damping thresholds before  $\theta_{imax}$  and  $\theta_{imin}$ , respectively, and  $\theta_{itmax} = (1-\Omega)\theta_{imax} + \Omega\theta_{imin}$ ,  $\theta_{itmin} = (1-\Omega)\theta_{imin} + \Omega\theta_{imax}$ .  $g_\Omega(\bullet)$  is a transitional function for the weighted factor varying from one to zero:

$$g_\Omega(d) = \frac{1}{2} - \frac{1}{2} \tanh\left(\frac{1}{1-d} - \frac{1}{d}\right), \quad d \in [0, 1]. \quad (17)$$

Based on the control technique in Eq. (16), an activation buffer is successfully taken into consideration that ensures the continuity and boundedness of the clamping weighted factor. In other words, when the joint motion runs in the flexible interval, the weighted value remains constant as one. While the joint goes towards the progressive interval from the flexible interval, the technique enables the weighted value to decrease uninterruptedly from one until zero, restricted at the joint position limit. Therefore, the continuous clamping weighted factor defined in Eq. (16) discards any unnecessary change of weighted value in the flexible region, in comparison to Eq. (10).

## 2.2 Repulsive Potential Field

Similar to the framework of WLN, the clamping control in this paper is designed

$$\dot{\theta} = \mathbf{E}_c \mathbf{J}_{E_c}^\oplus \dot{\mathbf{x}}, \quad (18)$$

where  $\mathbf{J}_{E_c} = \mathbf{J} \mathbf{E}_c$  is a weighted Jacobian matrix based on  $\mathbf{E}_c$  and  $\mathbf{J}_{E_c}^\oplus = \mathbf{E}_c \mathbf{J}^\top (\mathbf{J} \mathbf{E}_c \mathbf{E}_c \mathbf{J}^\top)^{-1}$ .

When  $\mathbf{E}_c = \mathbf{I}_n$ , Eq. (18) is equal to Eq. (2). While  $e_c(\theta_i) \rightarrow 0$ , we find it does not push  $\theta_i$  from the position limit but blocks any motion beyond the limit. However, referring to the potential field methods applied to avoid obstacles in IK resolutions of redundant manipulators [19], we define a repulsive task  $\mathbf{J}_{B_k} \mathbf{T}_r$  to force  $\theta_i$  back far from its limit that is depended on the joint positions and orthogonal to the primary task by means of being projected onto the weighted null space  $\mathbf{P}_{E_c}^\oplus$ . Therefore, a novel control scheme is represented as:

$$\theta = \mathbf{E}_c \mathbf{J}_{E_c}^\oplus \dot{\mathbf{x}} - \mathbf{P}_{E_c}^\oplus \mathbf{J}_{B_k} \mathbf{T}_r, \quad (19)$$

where  $\mathbf{P}_{E_c}^\oplus = \mathbf{I}_n - \mathbf{J}_{E_c}^\oplus \mathbf{J}_{E_c}$ ,  $\mathbf{J}_{B_k} = \mathbf{I}_n - \mathbf{E}_c$  indicates the weighted constraint Jacobian matrix for the repulsive task.  $\mathbf{T}_r = \text{diag}(t_r(\theta_i))$  is the repulsive force, whose element  $t_r(\theta_i)$  is designed by:

$$t_r(\theta_i) = \begin{cases} \frac{\theta_i - \theta_{itmin}}{\theta_{itmin} - \theta_{imin}} t_{rmax} & \theta_{imin} \leq \theta_i \leq \theta_{itmin} \\ 0 & \theta_{itmin} < \theta_i < \theta_{itmax} \\ \frac{\theta_i - \theta_{itmax}}{\theta_{itmax} - \theta_{imax}} t_{rmax} & \theta_{itmax} \leq \theta_i \leq \theta_{imax} \end{cases}, \quad (20)$$

$t_{rmax}$  denotes the maximum potential field force. The closer to the limit it is, the stronger the repulsive potential force is.

When joints are all located within the flexible interval,  $\mathbf{J}_{B_k} = \mathbf{0}$ , Eq. (19) acts as Eq. (2). While a joint remains in the progressive interval,  $\mathbf{J}_{B_k} \neq \mathbf{0}$ , the clamping and repulsive potential force are activated and withdraw the joint motion away from limit as far as possible. While the joint  $\theta_i$  reaches its limit,  $e_c(\theta_i) \rightarrow 0$ , the clamping term is disabled but  $t_r(\theta_i)$  becomes greatest and to push the joint motion away from its limit plays a dominant role in controlling. However, since  $\mathbf{P}_{E_c}^\oplus \mathbf{J}_{B_k} \mathbf{T}_r$  is a homogeneous solution, therefore, the main task of the manipulator is not affected.

Note that the manipulator could degenerate when it enters the singular region. According to the DLS method, Eq. (19) is arranged in the form:

$$\dot{\theta} = \mathbf{E}_c \mathbf{J}_{E_c}^\oplus \dot{\mathbf{x}} - \mathbf{P}_{E_c}^\oplus \mathbf{J}_{B_k} \mathbf{T}_r, \quad (21)$$

where  $\mathbf{J}_{E_c}^{\oplus, \rho_{E_c}}$ ,  $\mathbf{P}_{E_c}^{\oplus, \rho_{E_c}}$  are reproduced from  $\mathbf{J}_{E_c}^{\oplus}$  and  $\mathbf{P}_{E_c}^{\oplus}$  based on the DLS method. The damping factor  $\rho_{E_c}$  is derived from Eq. (4) by substituting  $\mathbf{J}_{E_c}$  for  $\mathbf{J}$ .

### 2.3 Continuous Scalar Coefficient

Eq. (21) is defined to improve the redundant manipulator performance of avoiding joint position limits. However, when the manipulator is executing tasks under the complicated conditions of multiple constraints, Eq. (21), thus, cannot generate feasible joint velocity. Therefore, pertinent performance criteria for the joint motion have to be considered.

To solve such a problem generally requires compiling multiple criteria as a sum over weighted subtasks' quadratic functions, and a trade-off of the main task and subtasks is performed by the manual tuning of the weights [20], which is often expressed as:

$$\phi = \sum_{j=1}^s k_j \nabla \mathbf{H}_j, \quad (22)$$

where  $k_j$  is the fixed scalar factor for the  $j^{\text{th}}$  performance criterion  $H_j$ , and is selected empirically.  $s$  indicates the total number of performance criteria.

However, the units and magnitudes of multiple criteria may differ from each other so that the assignment of  $k_j$  for each criterion through experience can allow critical limitations in terms of balancing the strengths of the criteria in control. Therefore, normalization is required to obtain the same magnitude of each criterion for assigning an appropriate scalar factor. Since the fixed scalar factors are not applicable to any configurations of the manipulator, in this paper, the continuous scalar factor  $k_j(H_{nj})$  is redefined based on its normalization:

$$k_j(H_{nj}) = \pm f(H_{nj}), \quad (23)$$

where  $\pm f(\bullet)$  denotes a continuous function, and its sign is selected positively if the performance criterion is to be maximized and vice versa.  $H_{nj}$  is the normalized value of the criterion  $H_j$ .

For avoiding unnecessary optimizations of criteria when the configuration of the manipulator is in its most balanced state, hence, analogous to Eq. (16), the maximum and minimum normalized thresholds,  $H_{nj}^{Mt}$  and  $H_{nj}^{mt}$ , are defined as:

$$H_{nj}^{Mt} = (1 - \lambda)H_{nj}^M + \lambda H_{nj}^m, \quad (24)$$

$$H_{nj}^{mt} = (1 - \lambda)H_{nj}^m + \lambda H_{nj}^M, \quad (25)$$

where  $H_{nj}^M$  and  $H_{nj}^m$  indicate the upper and lower boundaries of  $H_{nj}$ , respectively.  $\lambda$  controls the bandwidth between  $H_{nj}^{Mt}$  ( $H_{nj}^{mt}$ ) and  $H_{nj}^M$  ( $H_{nj}^m$ ).

To obtain a continuous scalar factor, the continuous function  $f(\bullet)$  is expressed as follows:

$$f(H_{nj}) = \begin{cases} 1 & H_{nj}^m \leq H_{nj} \leq H_{nj}^{Mt} \\ aH_{nj}^3 + bH_{nj}^2 + cH_{nj} + d & H_{nj}^{mt} < H_{nj} < H_{nj}^{Mt} \\ 0 & H_{nj}^{Mt} \leq H_{nj} \leq H_{nj}^M \end{cases}, \quad (26)$$

where

$$a = -\frac{2}{(H_{nj}^{Mt})^3 - 3(H_{nj}^{Mt})^2 H_{nj}^m + 3H_{nj}^{Mt} (H_{nj}^m)^2 - (H_{nj}^m)^3},$$

$$b = \frac{3H_{nj}^{Mt} + 3H_{nj}^m}{(H_{nj}^{Mt})^3 - 3(H_{nj}^{Mt})^2 H_{nj}^m + 3H_{nj}^{Mt} (H_{nj}^m)^2 - (H_{nj}^m)^3},$$

$$c = -\frac{6H_{nj}^{Mt} H_{nj}^m}{(H_{nj}^{Mt})^3 - 3(H_{nj}^{Mt})^2 H_{nj}^m + 3H_{nj}^{Mt} (H_{nj}^m)^2 - (H_{nj}^m)^3},$$

$$d = \frac{3H_{nj}^{Mt} (H_{nj}^m)^2 - (H_{nj}^m)^3}{(H_{nj}^{Mt})^3 - 3(H_{nj}^{Mt})^2 H_{nj}^m + 3H_{nj}^{Mt} (H_{nj}^m)^2 - (H_{nj}^m)^3}.$$

In Fig. 3, it is obvious that the curve is monotonously decreasing and continuous. When  $k_j \rightarrow 1$ , the influence of the  $j^{\text{th}}$  performance criterion becomes increasingly evident in the resolution of IK for the redundant manipulator. Conversely, when  $k_j \rightarrow 0$ , the criterion is increasingly deprived of the IK resolution.

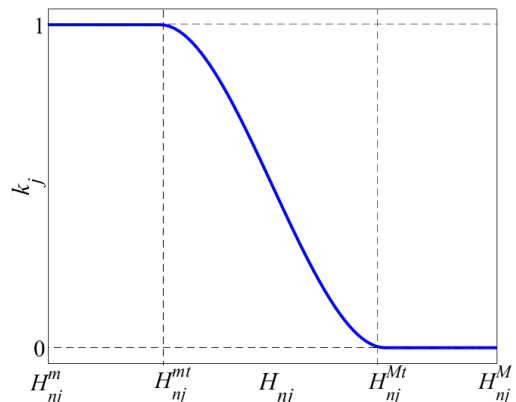


Fig. 3. A scalar coefficient for the corresponding performance criterion by calculation

### 2.4 Normalizing Criteria

Before normalization, the type and optimal value distribution of the performance criterion should be considered and analysed. For simplicity, assume a

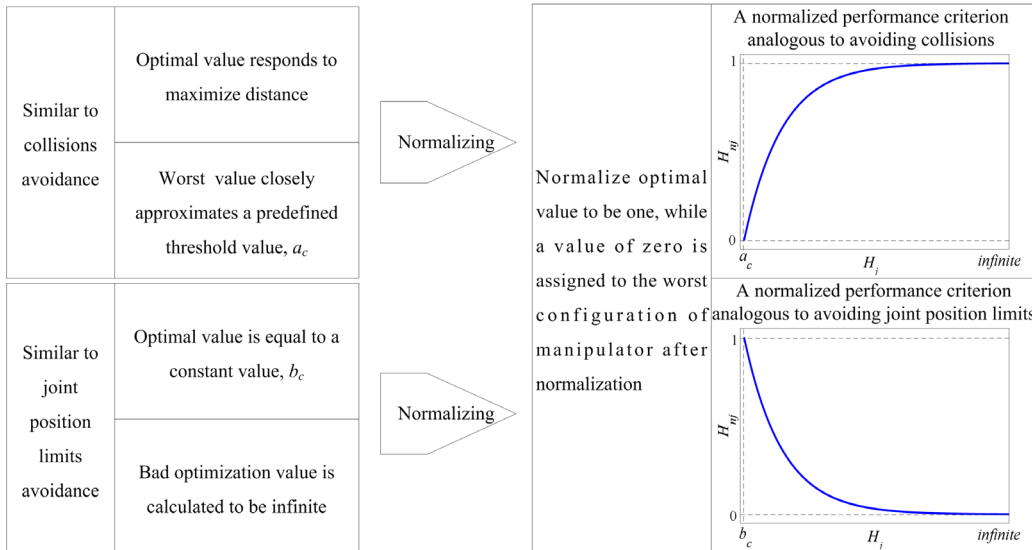


Fig. 4. A principle utilized to normalize different performance criteria

performance criterion is optimized by maximization or minimization in this paper.

For instance, in the case of avoiding collisions, the distance between EE and an obstacle is often defined as a performance criterion, which is supposed to maximize the distance but to oppose a small one, especially tending to the distance of zero.

Taking the avoidance of joint position limits defined as Eq. (11) as another example, the optimal value for each joint is equal to one as the joint position is in the middle of its limit, while the value becomes infinite when the joint goes towards the limit. Thus, the distribution of optimal value of avoiding joint position limits is the opposite of the case of avoiding collisions.

Consequently, distributions of optimal values vary from different performance criteria. For normalizing these individuals, we assume normalization for a criterion conforms to the following principle illustrated in Fig. 4.

To normalize the criteria similar to collisions avoidance, an exponential function is defined to normalize this kind of criteria

$$N_{\infty}(H_j) = 1 - \exp(a_c - H_j), \quad (27)$$

where  $N_{\infty}(\infty) = 1$  denotes the optimal normalized value far away from the predefined threshold  $a_c$ , and  $N_{\infty}(a_c) = 0$  indicates the manipulator is in the configurations that are restrained strictly.

On contrary, to normalize the criteria analogous to avoidance of the joint position limits where the

optimal value tends to a constant value  $b_c$  rather than infinite, we define another an exponential function for normalizations of these performance criteria

$$N_c(H_j) = \exp(b_c - H_j), \quad (28)$$

where  $N_c(b_c) = 1$  shows the optimal configuration of the manipulator without poor performances, e.g.,  $H_j = \infty$  far greater than  $b_c$ , correspondingly,  $N_c(\infty) = 0$ .

Based on the principles defined in Fig. 4, the same closed-range of normalized results can be obtained with the optimum to be one and the inferior to be zero, despite different properties of different performance criteria.

### 2.5 Resolution of WGPM

Therefore, we can obtain a novel GPM method, WGPM, considering multiple criteria, which is presented as:

$$\dot{\theta} = E_c J_{E_c}^{\oplus, \rho_{E_c}} \dot{x} - P_{E_c}^{\oplus, \rho_{E_c}} (J_{B_k} T_r + \sum_{j=1}^s k_j(H_{nj}) \nabla H_j). \quad (29)$$

In complicated circumstances, the criteria may be numerous, and their priority may be varied [20]. Specifically, if some performance criteria are activated simultaneously, criteria exhibit irregularities that affect the redundancy resolution of the manipulator. To regulate multiple criteria and improve the stability of the WGPM method, we set different priorities for criteria through weighted null space. Thus, Eq. (29) is rewritten as a hierarchy-based resolution:

$$\dot{\theta} = \mathbf{E}_c \mathbf{J}_{E_c}^{\oplus, \rho_{E_c}} \dot{\mathbf{x}} - \mathbf{P}_{E_c}^{\oplus, \rho_{E_c}} \times (\mathbf{J}_{B_k} \mathbf{T}_r + \sum_{j=1}^s k_j (H_{nj}) \exp(\frac{1-j}{s} E_c) \nabla H_j), \quad (30)$$

where the defined clamping weighted matrix  $\mathbf{E}_c$  dominates other criteria, and priorities decrease as the number of subtasks increases.

When  $\mathbf{E}_c = \mathbf{I}_n$ , the repulsive potential field is inactive, but other performance criteria are active. However, when  $\mathbf{E}_c \neq \mathbf{I}_n$ , the repulsive potential field is activated to repel joints from their position limits, and the impacts of other performance criteria are reduced but not eliminated. Therefore, besides the main task, the priority of avoiding joint position limits is higher than any other criteria in the proposed hierarchical task-level regulation. As the joint motion reaches the singular region  $\varepsilon$ , the manipulator has to encounter a singularity,  $\rho_{E_c} > 0$ . Then Eq. (30) is nothing but the solution of the following damped least-squares problem:

$$\min_{\theta} (\|\dot{\mathbf{x}} - \mathbf{J}\dot{\theta}\|^2 + \rho_{E_c}^2 \|\mathbf{E}_c^{-1}\dot{\theta}\|^2). \quad (31)$$

Obviously, Eq. (30) is a compromise product between the feasibility of joint velocities and deviations of main tasks. That is to say, when  $\mathbf{E}_c \rightarrow \mathbf{0}$ , the least-norm solution in Eq. (30),  $\mathbf{E}_c \mathbf{J}_{E_c}^{\oplus, \rho_{E_c}} \dot{\mathbf{x}} \rightarrow \mathbf{0}$ , and the homogeneous solution

$$-\mathbf{P}_{E_c}^{\oplus, \rho_{E_c}} (\mathbf{J}_{B_k} \mathbf{T}_r + \sum_{j=1}^s k_j (H_{nj}) \exp(\frac{1-j}{s} E_c) \nabla H_j) \rightarrow -\mathbf{P}_{E_c}^{\oplus, \rho_{E_c}} \mathbf{J}_{B_k} \mathbf{T}_r$$

can no longer take effect in the weighted null space  $\mathbf{P}_{E_c}^{\oplus, \rho_{E_c}}$  due to the existence of  $\rho_{E_c}$ , and change the task priority to make optimization of avoiding joint position limits have higher priority than the main task motion.

### 3 RESULTS AND DISCUSSION

Simulations and experiments are constructed to demonstrate the effectiveness and practicability of the proposed WGPM method for IK resolutions of redundant manipulators. In this work, a 7-DOF redundant manipulator is taken as an analysis object, shown in Fig. 5. The D-H parameters of the manipulator with the allowable limits for joint positions and joint velocities are listed in Table 1, where  $m_2 = -0.2975$ ,  $m_3 = -0.3555$ ,  $l_1 = 0.45$ ,  $m_4 = -0.293$ ,  $l_2 = 0.4$ ,  $m_5 = 0.255$ ,  $m_6 = 0.197$ ,  $m_7 = 0.104$ .

To improve motion precision, the closed-loop algorithm is introduced that is expressed as:

$$\dot{\mathbf{x}} = \dot{\mathbf{x}}_d + \kappa \mathbf{E}_e, \quad (32)$$

where  $\dot{\mathbf{x}}_d$  is the desired trajectory.  $\kappa$  is the positive feedback gain, and is set to 80.  $\mathbf{E}_e \in \mathbf{R}^{6 \times 1}$  indicates the tracking error between the desired and actual trajectory

$$\mathbf{E}_e = \begin{bmatrix} \mathbf{P}_d - \mathbf{P} \\ 0.5(\mathbf{n} \times \mathbf{n}_d + \mathbf{s} \times \mathbf{s}_d + \mathbf{a} \times \mathbf{a}_d) \end{bmatrix}, \quad (33)$$

$\mathbf{P}_d \in \mathbf{R}^{3 \times 1}$ ,  $\mathbf{P} \in \mathbf{R}^{3 \times 1}$  are the vectors of the desired and actual position of EE, and  $\mathbf{R}_d = (\mathbf{n}_d, \mathbf{s}_d, \mathbf{a}_d) \in \mathbf{R}^{3 \times 3}$ ,  $\mathbf{R} = (\mathbf{n}, \mathbf{s}, \mathbf{a}) \in \mathbf{R}^{3 \times 3}$ , express the rotation matrices for the desired and actual orientations of EE, respectively.

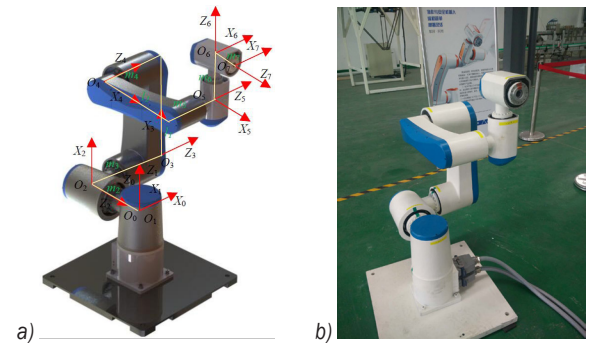


Fig. 5. A 7-DOF redundant manipulator; a) kinematic model, b) physical prototype

Table 1. D-H parameters and joint limits

$i$	$\alpha_{i-1}$ [°]	$a_{i-1}$ [m]	$d_i$ [m]	$\theta_i$ [°]	$\theta_{i\min} \sim \theta_{i\max}$ [°]	$v_{i\max}$ [°/s]
1	0	0	0	q1	-160 ~ 160	55
2	90	0	$m_2$	q2	-33 ~ 150	55
3	90	0	$m_3$	q3	-165 ~ 80	55
4	0	$l_1$	$m_4$	q4	-180 ~ 40	55
5	0	$l_2$	$m_5$	q5	-150 ~ 150	65
6	90	0	$m_6$	q6	-180 ~ 180	65
7	90	0	$m_7$	q7	-180 ~ 180	65

Furthermore, the simulations in the paper are implemented with the aid of the Matlab R2016a tool, and in the experiment, a computer with Intel Core i3 @ 1.8 GHz processor & 2 GB RAM as the control platform and the LabVIEW 2016 as the operation software are utilized to control servo joints connected in the manipulator with a sampling time of 0.005 s.

#### 3.1 Numerical Simulations of Clamping and Repulsive Force

As a validation of the proposed clamping and repulsive potential field, we only consider the avoidance of joint position limits as a subtask in redundancy resolution

of the manipulator. Therefore, scalar factors in Eq. (30) for other criteria are set to zero manually. For comparisons, the WLN method defined in Eq. (14) is provided as well.  
WLN:

$$\dot{\theta} = W^{-1} J^T (JWJ^T + \rho^2 I_6)^{-1} (\dot{x}_d + \kappa E_e), \quad (34)$$

WGPM:

$$\dot{\theta} = E_c J_{E_c}^{\oplus, \rho_{E_c}} (\dot{x}_d + \kappa E_e) - J_{E_c}^{\oplus, \rho_{E_c}} J_{B_k} T_r, \quad (35)$$

where  $\rho$  and  $\rho_{E_c}$  are damping factors of WLN and WGPM reduced from Eq. (4) where  $\varepsilon=0.02$ ,  $\rho_{\max}=0.02$ , and  $\sigma_{\min}$  are the minimum singular values of  $J_w$  and  $J_{E_c}$ , respectively.

In simulations, we control the manipulator to track a straight-line path whose position is interpolated with the modified trapezoidal function and orientation expressed as Euler angles is planned with the five-order polynomial function. The initial posture of EE is  $P_s=[0.3174, -0.2065, 0.6469]$  [m],  $O_s=[-90, 90, 90]$  [degree], and terminal posture is  $P_f=[0.37, 0.0068, 0.1707]$  [m],  $O_f=[-1.0036, 94.9841, -116.8194]$  [degree].

It is noted that the specified path is beyond the reachability of the redundant manipulator, and the fourth joint position in the terminal posture is close to its limit deliberately.

Simulation results of the WLN method are shown in Fig. 6. It is found that WLN comes to suffer from singularity at  $t=0.14$  s in Fig. 6c.

However, with the assistance of the DLS method, the continuity of joint velocity in Fig. 6b is still ensured at the expense of deviation of tracking trajectory, i.e., the WLN method obtains the maximum position error at  $t=0.28$  s in Fig. 6d. Fig. 6a depicts the normalized joint position expressed as  $(2\theta_i - \theta_{i\max} - \theta_{i\min}) / (\theta_{i\max} - \theta_{i\min})$ . Obviously, the fourth joint position is damped at limit due to the effect of the penalty function defined in Eq. (11), yielding an increasing weighted factor for the fourth joint shown in Fig. 6e.

Fig. 7 illustrates the simulation results of the proposed WGPM method. To force joints back away from their position limits effectively, the width of the progressive buffer,  $\Omega$ , is set to 0.25, and the maximum potential field force,  $t_{r\max}$ , is equal to  $\pi$ . From Fig. 7d, singularity resulted from WGPM occurs later than that from WLN, and as observed in Fig. 7a, the fourth joint position is restrained into the specified range but not violate the limit compared to that in WLN. The fundamental cause for this lies in the action of the repulsive potential field  $J_{B_k} T_r$  in the WGPM control where a large velocity is obtained based on the clamping weighted factors in Fig. 7f and projected onto the weighted null space  $P_{E_c}^{\oplus, \rho_{E_c}}$  with opposite direction, as shown in Fig. 7c, exploited to push the fourth joint away from the limit. Meanwhile, the seventh joint is effectively kept away from its position limit in comparison with that in the WLN method.

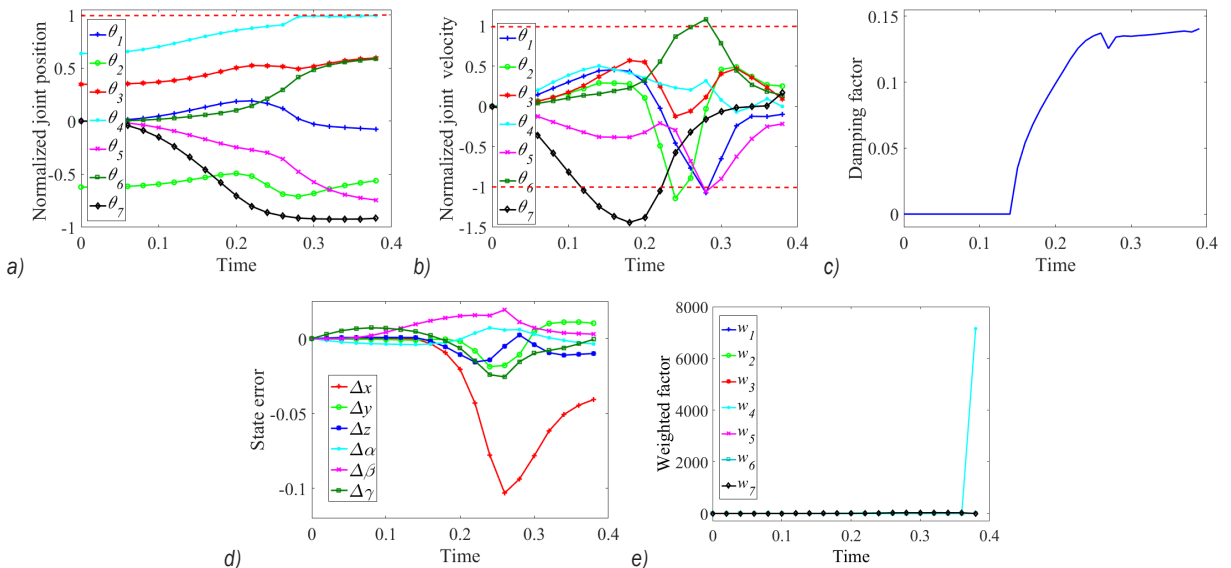
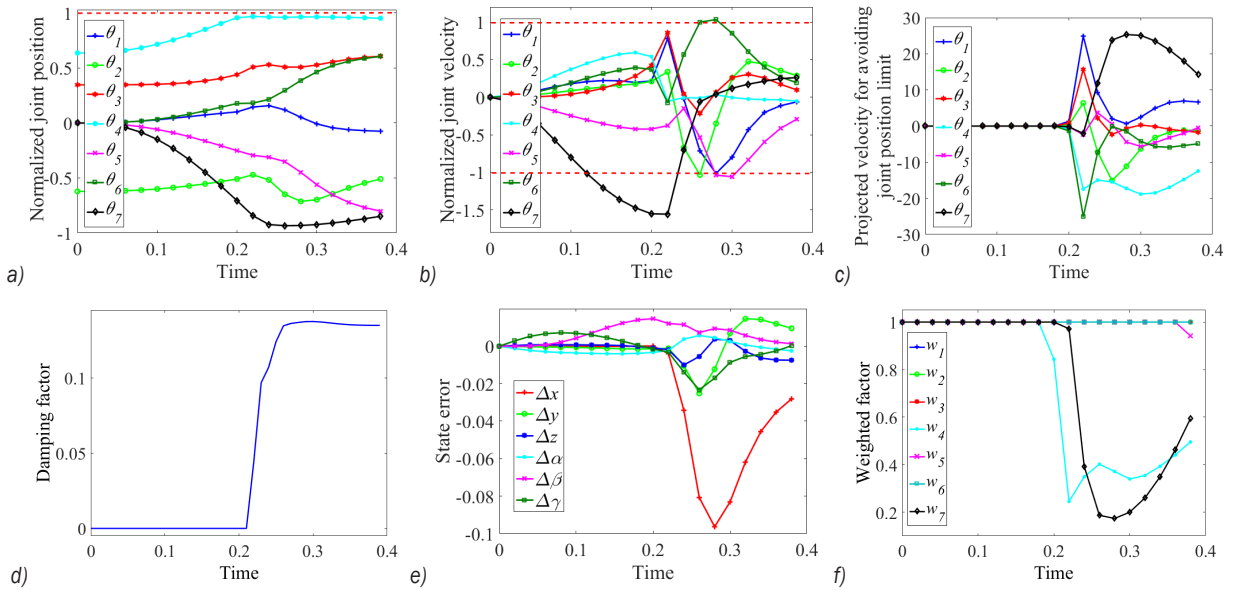


Fig. 6. Simulation results of the WLN method; a) normalized joint position, b) normalized joint velocity, c) damping factor, d) state error including position errors and orientation errors, and e) weighted factor



**Fig. 7.** Simulation results of the proposed WGPM method; a) normalized joint position, b) normalized joint velocity, c) projected velocity produced from the repulsive potential field, d) damping factor, e) state error including position errors and orientation errors, and f) weighted factor composing the clamping matrix

**Table 2.** The maximum simulation results of state errors

	WLN	WGPM	Percentage [%]
Max $\Delta x$ [m]	-0.1031	-0.0963	6.6
Max $\Delta y$ [m]	-0.0209	-0.0212	-1.44
Max $\Delta z$ [m]	-0.0162	-0.01	38.27
Max $\Delta\alpha$ [rad]	0.0072	0.0057	20.83
Max $\Delta\beta$ [rad]	0.0192	0.0147	23.44
Max $\Delta\gamma$ [rad]	-0.0256	-0.0233	8.98
Running time [s]	0.2337	0.1832	21.61

Table 2 briefly shows the maximum simulation results of state errors generated from WLN and WGPM. It is found that except along the direction of the  $Y$ -axis, the proposed WGPM method significantly increases the motion accuracy compared to the WLN method, which reduces position errors by 6.6 %, 38.27 % along the  $X$  and  $Z$  axes, and orientation errors by 20.83 %, 23.44 %, and 8.98 %. Meanwhile, since the WGPM method only performs optimizations when the joint position steps into the defined progressive interval while the WLN method optimizes the joint position throughout the whole interval, WGPM avoids the unneeded optimization procedure and improves the computational efficiency by 21.61 %.

Consequently, the simulation results indicate that the efficiency of the proposed WGPM method with clamping weighted matrix and repulsive potential field is superior to the traditional WLN method.

However, from Figs. 6b and 7b, except the third joint and the fourth joint, other joint velocities exceed their limits shown as normalizations, which is not admitted to appear in the physical control of manipulator. Thus, the problem will be resolved in the following experiment and the performance of the proposed WGPM method with multiple criteria will be verified.

### 3.2 Experimental Verification with Multiple Criteria

As the joint velocity violates its limit in the above simulations, joint velocity commands may lose effect when large instantaneous task velocity is requested, causing significant velocity saturations [21]. Analogous to the criterion of avoiding joint position limits expressed as Eq. (11), the performance criterion of avoiding joint velocity limits is defined as:

$$G(\dot{\theta}_i) = \sum_{i=1}^7 \frac{(\dot{\theta}_{i\max} - \dot{\theta}_{i\min})^2}{4(\dot{\theta}_{i\max} - \dot{\theta}_i)(\dot{\theta}_i - \dot{\theta}_{i\min})}, \quad (36)$$

where  $\dot{\theta}_{i\max}$  (expressed as  $v_{i\max}$  in Table 1),  $\dot{\theta}_{i\min} = -\dot{\theta}_{i\max}$  are the maximum and minimum of the  $i^{\text{th}}$  joint velocity, respectively. This also complies with the principle of normalizing a performance criterion defined in Fig. 4.

The experiment focuses on the realization of the main tasks under the joint limit constraints such as joint position limits and joint velocity limits. The comparison with the conventional GPM method is

devised to validate the superiority of the proposed WGPM method in this case. Therefore, combining Eqs. (11), (12) and (36), the conventional GPM method with fixed scalar factors for multiple criteria is written as:

$$\dot{\theta} = J_a^+(\dot{x}_d + \kappa E_e) + (I_7 - J_a^+ J)(k_H \nabla H(\theta) + k_G \nabla G(\dot{\theta})), \quad (37)$$

where  $k_H$ ,  $k_G$  are the fixed scalar coefficients to regulate the projected velocities of avoiding joint position limits and joint velocity limits and are set to  $-0.1$  and  $-0.05$  by trial and error, respectively. Since  $\text{abs}(k_H) > \text{abs}(k_G)$ , the priority of avoiding joint position limits is higher than that of avoiding joint velocity limits.

The proposed WGPM method with the performance criterion of avoiding joint velocity limits described as Eq. (36) is expressed as:

$$\dot{\theta} = E_c J_{E_c}^{\oplus, \rho E_c}(\dot{x}_d + \kappa E_e) - P_{E_c}^{\oplus, \rho E_c}(J_{B_k} T_r + k(G_n) \exp(0 E_c) \nabla G), \quad (38)$$

where the bandwidth for defining thresholds in normalization,  $\lambda$ , is set to 0.3.

The overview of the experimental setup is shown in Fig. 8, which mainly consists of the PC LabVIEW program, the motion control card and the redundant manipulator. These three parts communicate with each other to deliver the target and actual joint position by means of PCI and EtherCAT, and the traditional GPM method and the proposed WGPM method are embedded in the PC LabVIEW program to generate the target joint position. Moreover, the initial and terminal postures for manipulator in experiments are set as reference, and the terminal posture is also out of the manipulator's reachability, which is shown in Fig. 9. The trajectory is planned as a straight-line path of round-trip, i.e.,  $P_s \rightarrow P_f \rightarrow P_s$ . Besides, the values of other parameters remain unchanged, as defined in the previous simulations.

Initial posture:

$$P_s = [0.4063, -0.238, 0.5969] \text{ [m]},$$

$$O_s = [-80.8661, 92.267, 79.244] \text{ [degree]}.$$

Terminal posture:

$$P_f = [0.5917, -0.2083, 0.104] \text{ [m]}$$

$$O_f = [-92.1895, 125.3982, 43.4023] \text{ [degree]}.$$

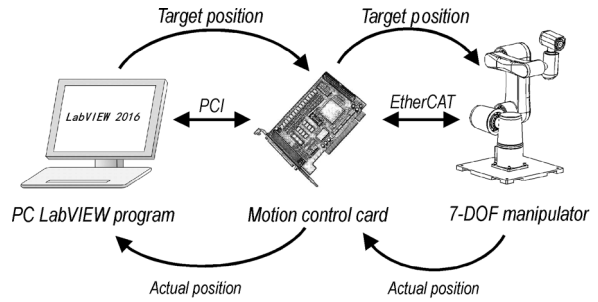


Fig. 8. Experimental setup

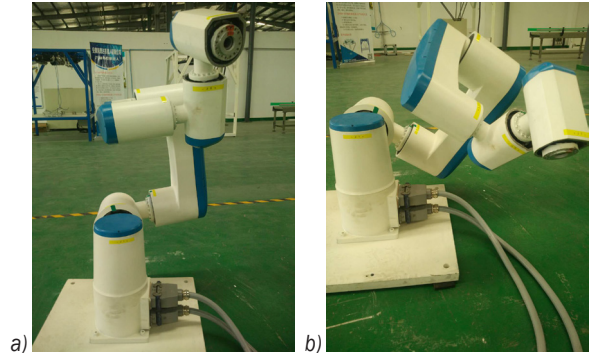
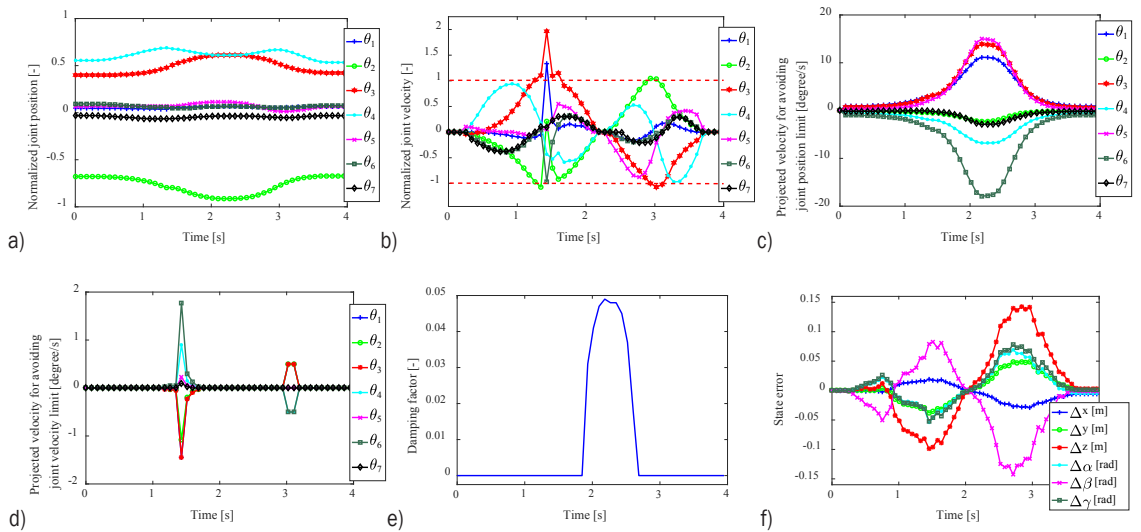


Fig. 9. Initial posture and terminal posture of the manipulator as reference; a) initial posture, and b) terminal posture

Fig. 10 illustrates the experimental results of the conventional GPM method. Seen from Fig. 10a, the second joint is approaching its position limit at  $t=1.932$  s that leads to a singularity and motion deviation inevitably depicted in Figs. 10e and f, respectively. Since the influence of performance criterion of avoiding joint position limits defined in Eq. (11) is projected onto the null space shown in Fig. 10c, the second joint position limit is not violated with the smallest projected velocity by virtue of the advantage of redundancy.

However, it is noted that when tracking the large joint command velocities, extreme vibration chatter occurs at  $t=1.428$  s shown in Fig. 10b. Eq. (37) defines a behaviour composed of main task and subtasks where the priority of avoidance of joint position limits is higher than that of avoidance of joint velocity limits but lower than the main task. Therefore, the projected velocities for avoiding joint velocity limits, depicted in Fig. 10d, are smaller than those for avoiding joint position limits even if the criterion of avoiding joint velocity limits is activated. Hence, the regulation between the main task and avoidances of joint position limits and joint velocity limits by the conventional GPM method failed.

The experimental results of the proposed WGPM method are summarized as shown in Fig.



**Fig. 10.** Experiment results of the conventional GPM method with avoiding joint position limits and joint velocity limits; a) normalized joint position, b) normalized joint velocity, c) projected velocity produced from the performance criterion of avoiding joint position limits, d) projected velocity produced from the performance criterion of avoiding joint velocity limits, e) damping factor, and f) state error including position errors and orientation errors

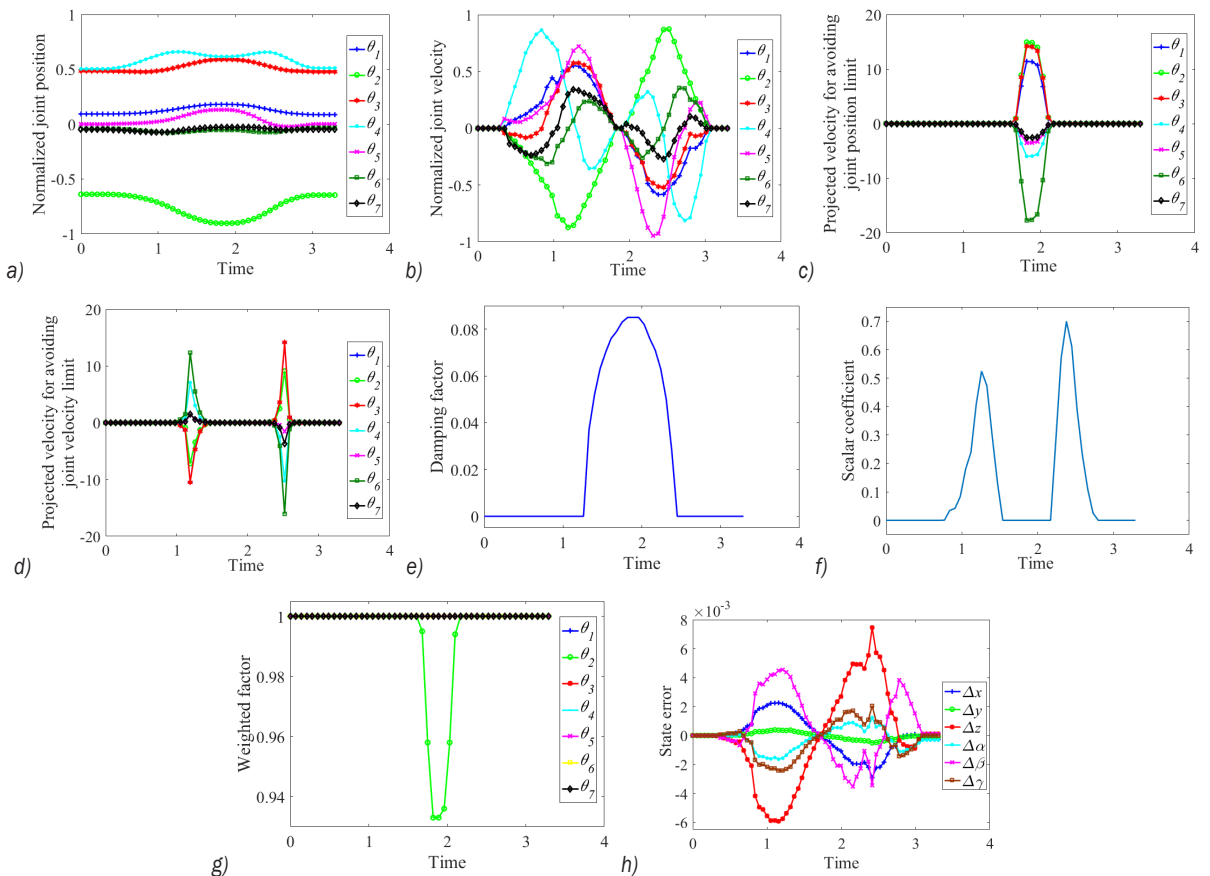


**Fig. 11.** Experiment results of the proposed WGPM method with avoiding joint position limits and joint velocity limits; a) normalized joint position, b) normalized joint velocity, c) projected velocity produced from the performance criterion of avoiding joint position limits, d) projected velocity produced from the performance criterion of avoiding joint velocity limits, e) damping factor, f) scalar coefficient of avoiding joint velocity limits, g) weighted factor from clamping matrix, and h) state error including position errors and orientation errors

11. Similarly, from Fig. 11a, the second joint is also close to its limit at  $t=1.89$  s, and the corresponding weighted factor decreases to 0.933 in Fig. 11g according to the clamping weighted matrix operator with the appearance of singular configurations of the manipulator during  $t=1.33$  s to 2.38 s. Remarkably, in the singular time shown in Fig. 11e, because the clamping matrix is not equal to an identity matrix, the repulsive potential field is activated to suppress the second joint velocity and repel it from its position limit effectively with a large opposite projected velocity, which passes through the weighted null space depicted in Fig. 11c. More significantly, however, from Figs. 10c and 11c, due to the different constructions of projected velocities for avoiding joint position limits between WGPM and GPM, the direction of the second joint projected velocity in WGPM is opposite to that in GPM.

From Fig. 11f, adopting the proposed continuous scalar coefficient theory, the coefficient for performance criterion of avoiding joint velocity limits is continuously documented dependent on the real-time joint velocities. Therefore, the projected velocities for avoiding joint velocity limits, shown in Fig. 11d, exist accompanied by the variation of the scalar coefficient and effectively restrain the joint velocity into a reasonable limit so as to protect and maintain the continuity of joint velocity. As such, the scheme to avoid joint velocity limits can play a positive effect on limiting joint velocities expressed as the normalizations depicted in Fig. 11b without any vibrations. Specifically, the scalar coefficient for avoiding joint velocity limits is automatically adjusted in WGPM while it is assigned a small constant value in GPM. Therefore, in Fig. 11d, two strong groups of projected velocities exist to avoid the second, the fourth and the fifth joint velocity violating their limits in the WGPM control while only an effective group, as shown in Fig. 10d, is produced from the conventional GPM control to constrain the first, the second, the third, and the sixth joint velocities.

The motion accuracies of the manipulator in experiments based on the traditional GPM method and the proposed WGPM method are demonstrated in Table 3. Obviously, the WGPM method has, compared to the GPM method, a potential advantage to enhance the kinematic performance of redundant manipulator that reduces errors by 6.27 %, 24.08 % and 45.33 % in position and by 44.81 %, 20.96 %, 12.04 % in orientation, respectively. Furthermore, as discussed previously, WGPM optimizes joint velocities in accordance with the clamping weighted matrix for avoiding joint position limits and the continuous scalar

coefficient for avoiding joint velocity limits while GPM does that all the time. Therefore, the proposed WGPM method could save time, i.e., decreasing 16.29 % of the time the GPM method consumed in the experiment.

**Table 3.** The maximum experimental results of state errors

	GPM	WGPM	Percentage [%]
Max $\Delta x$ [m]	-0.0287	-0.0269	6.27
Max $\Delta y$ [m]	0.049	0.0372	24.08
Max $\Delta z$ [m]	0.1425	0.0779	45.33
Max $\Delta \alpha$ [rad]	0.0694	0.0383	44.81
Max $\Delta \beta$ [rad]	-0.1422	-0.1124	20.96
Max $\Delta \gamma$ [rad]	0.0781	0.0687	12.04
Running time [s]	3.948	3.305	16.29

Consequently, the main task with continuous joint positions and joint velocities is completed by means of the proposed WGPM method in which joint motion is subject to different performance criteria sufficiently, while the traditional GPM method is invalid.

#### 4 CONCLUSIONS

The simulations and experiments in the paper are conducted to prove the validation and efficiency of the proposed WGPM method with multiple performance criteria. The results are concluded as follows:

1. Tracking the singular trajectory in simulations, the fourth joint and the seventh joint are successfully driven from joint position limits owing to exploitations of the proposed WGPM method, while they are arrested at limits using the WLN method that cannot repel them from limits. However, both methods violate joint velocity limits without taking into consideration the corresponding performance criterion.
2. The joint position limits and joint velocity limits are added to the experiments. In terms of guaranteeing the joint position limits, GPM performs as well as WGPM. In contrast, the regulation of avoiding joint velocity limits works barely satisfactory by using GPM that leads to a vibration chatter due to the unreasonable arrangement of fixed weights for multiple criteria. Contrarily, the hierarchical WGPM control effectively regulates the joint velocities far away limits based on the continuous scalar coefficient.
3. By analyses and comparisons of the simulation and experimental results, the hierarchical task-level regulation between the main task and subtasks in the proposed WGPM method is the

primary factor influence on improving kinematic motion prevision and saving time compared to the traditional WLN and GPM methods.

The paper provides a novel resolution to the IK problems of a redundant manipulator with multiple constraints. Future work will focus on the kinematical control of a redundant dual-arm manipulator.

## 5 ACKNOWLEDGEMENTS

The work supported by the National Natural Science Foundation (Grant no. 51375230, and Grant no. 51706098), China, and the Scientific and Technological Project in Anhui Province (Grant no. 1501021023), China.

## 6 REFERENCES

- [1] Giorelli, M., Renda, F., Calisti, M., Arienti, A., Ferri, G., Laschi, C. (2015). Neural network and Jacobian method for solving the inverse statics of a cable-driven soft arm with nonconstant curvature. *IEEE Transactions on Robotics*, vol. 31, no. 4, p. 823-834, DOI:10.1109/TRO.2015.2428511.
- [2] Cheng, G., Xu, P., Yang, D.H., Li, H., Liu, H.G. (2013). Analysing kinematics of a novel 3CPS parallel manipulator based on Rodrigues parameters. *Strojniški vestnik - Journal of Mechanical Engineering*, vol. 59, no. 5, p. 291-300, DOI:10.5545/sv-jme.2012.727.
- [3] Jin, L., Zhang, Y., Li, S., Zhang, Y. (2016). Modified ZNN for time-varying quadratic programming with inherent tolerance to noises and its application to kinematic redundancy resolution of robot manipulators. *IEEE Transactions on Industrial Electronics*, vol. 63, no. 11, p. 6978-6988, DOI:10.1109/TIE.2016.2590379.
- [4] Jin, L., Li, S. (2016). Distributed task allocation of multiple robots: A control perspective. *IEEE Transactions on Systems, Man, and Cybernetics: Systems*, vol. 48, no. 5, p. 693-701, DOI:10.1109/TSMC.2016.2627579.
- [5] Colomé, A., Torras, C. (2015). Closed-loop inverse kinematics for redundant robots: comparative assessment and two enhancements. *IEEE/ASME Transactions on Mechatronics*, vol. 20, no. 2, p. 944-955, DOI:10.1109/TMECH.2014.2326304.
- [6] Hu, T., Wang, T., Li, J., Qian, W. (2017). Gradient projection of weighted Jacobian matrix method for inverse kinematics of a space robot with a controlled-floating base. *ASME Journal of Dynamic Systems, Measurement, and Control*, vol. 139, no. 5, p. 051013-1-051013-10, DOI:10.1115/1.4035398.
- [7] He, X., Kong, X., Chablat, D., Caro, S., Hao, G. (2014). Kinematic analysis of a single-loop reconfigurable 7R mechanism with multiple operation modes. *Robotica*, vol. 32, no. 7, p. 1171-1188, DOI:10.1017/S0263574713001197.
- [8] He, X., Kong, X., Hao, G., Ritchie, J. (2016). Design and analysis of a new 7R single-loop mechanism with 4R, 6R and 7R operation modes. Ding, X., Kong, X., Dai, J. (eds.), *Mechanisms and Machine Science: Advances in Reconfigurable Mechanisms and Robots II*. Springer, Berlin, vol. 36, p. 27-37, DOI:10.1007/978-3-319-23327-7\_3.
- [9] Kapoor, C., Cetin, M., Tesar, D. (1998). Performance based redundancy resolution with multiple criteria. *ASME Design Engineering Technical Conference*, p. 1-6.
- [10] Lee, K.K., Buss, M. (2006). Redundancy resolution with multiple criteria. *IEEE/RSJ International Conference on Intelligent Robots and Systems*, p. 598-603, DOI:10.1109/IROS.2006.282538.
- [11] Chaumette, F., Marchand, E. (2001). A redundancy-based iterative approach for avoiding joint limits: application to visual servoing. *IEEE Transactions on Robotics and Automation*, vol. 17, no. 5, p. 719-730, DOI:10.1109/70.964671.
- [12] Lu, B., Guo, S., Han, L. (2016). A coefficient matrix GPM method to avoid joint limits for fault tolerant redundant manipulators. *35th Chinese Control Conference (CCC)*, p. 7076-7081, DOI:10.1109/ChiCC.2016.7554475.
- [13] Li, L., Gruver, W.A., Zhang, Q., Yang, Z. (2001). Kinematic control of redundant robots and the motion optimizability measure. *IEEE Transactions on Systems, Man, and Cybernetics - Part B: Cybernetics*, vol. 31, no. 1, p. 155-160, DOI:10.1109/3477.907575.
- [14] Miyata, S., Miyahara, S., Nenchev, D. (2017). Analytical formula for the pseudoinverse and its application for singular path tracking with a class of redundant robotic limbs. *Advanced Robotics*, vol. 31, no. 10, p. 509-518, DOI:10.1080/01691864.2017.1285721.
- [15] Nakamura, Y., Hanafusa, H. (1986). Inverse kinematic solutions with singularity robustness for robot manipulator control. *ASME Journal of Dynamic Systems, Measurement, and Control*, vol. 108, no. 3, p. 163-171, DOI:10.1115/1.3143764.
- [16] Jin, L., Li, S., La, H.M., Luo, X. (2017). Manipulability optimization of redundant manipulators using dynamic neural networks. *IEEE Transactions on Industrial Electronics*, vol. 64, no. 6, p. 4710-4720, DOI:10.1109/TIE.2017.2674624.
- [17] Lopez, J., Brenosa, J., Galiana, I., Ferre, M., Gimenez, A., Barrio, J. (2012). Mechanical design optimization for multi-finger haptic devices applied to virtual grasping manipulation. *Strojniški vestnik - Journal of Mechanical Engineering*, vol. 58, no. 7-8, p. 431-443, DOI:10.5545/sv-jme.2011.141.
- [18] Xiang, J., Zhong, C., Wei, W. (2010). General-weighted least-norm control for redundant manipulators. *IEEE Transactions on Robotics*, vol. 26, no. 4, p. 660-669, DOI:10.1109/TRO.2010.2050655.
- [19] Chen, Y.J., Ju, M.Y., Hwang, K.S. (2017). A virtual torque-based approach to kinematic control of redundant manipulators. *IEEE Transactions on Industrial Electronics*, vol. 64, no. 2, p. 1728-1736, DOI:10.1109/TIE.2016.2548439.
- [20] Huang, S., Xiang, J., Wei, W., Chen, M.Z.Q. (2018). On the virtual joints for kinematic control of redundant manipulators with multiple constraints. *IEEE Transactions on Control Systems Technology*, vol. 26, no. 1, p. 65-76, DOI:10.1109/TCST.2017.2650684.
- [21] Flacco, F., De Luca, A., Khatib, O. (2015). Control of redundant robots under hard joint constraints: saturation in the null space. *IEEE Transactions on Robotics*, vol. 31, no. 3, p. 637-654, DOI:10.1109/TRO.2015.2418582.

# Influence of Laser Power on Improving the Wear Properties of Laser-Deposited Ti-6Al-4V+B<sub>4</sub>C Composite

Mutiu F. Erinosh\* – Esther T. Akinlabi

University of Johannesburg, Department of Mechanical Engineering Science, South Africa

*Titanium and its alloys have possessed outstanding properties such as high specific strength, good oxidation and corrosion resistance; which have made them extensively suitable for use in the aeronautical, medical, automobile, marine and chemical industries. This paper presents the impact of laser power on the microstructure and the wear properties of titanium matrix Ti-6Al-4V+B<sub>4</sub>C composites. The laser power was varied from 0.8 kW to 2.2 kW while keeping other contributing parameters constant. The microstructural effects were characterized by increasing  $\alpha$ -Ti lamella and coarse Widmanstettan structures as the laser power was increased, with the inclusion of 20 wt % of B<sub>4</sub>C. The mechanical action during wear test has created a loop shape with inner and outer radii on the surface of the laser-deposited composites. The wear thickness, depth and COF were taken into account; with the sample C deposited at a laser power of 1.8 kW and scanning speed of 1 m/min having the lowest wear loss of 0.119 mm<sup>3</sup>. The substrate exhibited the shallowest wear depth, and the reason is attributed to the compressive nature of the material. The interlace of B<sub>4</sub>C in the titanium matrix has improved the properties of the laser-formed composites.*

**Keywords:** laser metal deposition, microstructure, wear measurement, Ti-6Al-4V+B<sub>4</sub>C composite

## Highlights

- The robustness of the  $\alpha/\beta$  phase increases as the laser power is increased.
- The mean wear thicknesses of the laser-deposited samples are varied from 0.309 mm and 0.504 mm.
- The entire laser-deposited samples experience a rise in the COF and later maintain steadiness between 0.35 and 0.5.
- The radii of the wear tracks and the mean wear depth have a significant effect on the wear loss.

## 0 INTRODUCTION

Laser metal deposition (LMD) is one of the most effective means of manufacturing complex geometrical components with high efficiency [1]. This process involves the manufacturing of a complex component directly from a three-dimensional (3D) computer-aided design (CAD) system [2], and it is characterized by an energy balance that is affected by the part being fabricated, the geometrical features of the substrate and the ambient temperature of the process [3]. This energy is however transformed into heat energy that creates the melt pool on the substrate [4]. Titanium and its alloys are metals that have been widely used in industries due to their desirable properties, including good corrosion resistance, high-strength-to-weight ratio, and retention of properties at high temperatures [2]. Despite all the fascinating properties of the alloy, they still possess poor wear resistance; however, the improvement in their properties has given room for other alloys to be integrated. TiB and TiC are widely preferred reinforcement agents for titanium due to their strength, interfacial bonding, excellent thermodynamic stability and related thermal expansion coefficient with the titanium matrix [5]. A small cylindrical bar of (Ti-6Al-4V + B) with a dimension of 9 mm by 6 mm was made to undergo a compressive test and compared

with the parent material, the Ti-6Al-4V alloy. After deformation, it was reported that a 50 % reduction in height was achieved and the microstructure of (Ti-6Al-4V + B) sample was characterized with strain-free  $\alpha$ -colonies and more homogenous dislocation density distribution as compared with the parent material [6]. Another research was conducted on cast (Ti-6Al-4V + xB) samples; where  $x$  is 0.05 wt %, 0.10 wt % and 0.40 wt % respectively. It was discovered that the microstructural refinement of the cast samples led to an increase in the yield and the ultimate tensile strength of the casted alloys. The strain to failure ratio was also reported to increase with a small addition of boron. However, revealed further that an increase in boron content would lead to an increase in fracture toughness [7], and a general improvement in the cracking resistance [8] to [10]. Premixed titanium and boron were blended in weight ratio 8:1 with sodium silicate solution and laser-deposited onto Ti-6Al-4V alloy substrate. Hard ceramic compounds of TiB and TiB<sub>2</sub> were revealed to be formed in the deposited alloy. Similarly, high microhardness values and excellent wear resistance of the laser deposited samples were also realized. However, the results were reported to have considerably enhanced the load-bearing capability of the substrate [11]. TiO<sub>2</sub> was sintered with B<sub>4</sub>C powder in steel dies at 80 MPa for 1 hour after preheating to 1500 °C for 2 hours in a vacuum

furnace. It was discovered that the resulting hardness values of the compacted composites ranged from 800 HV to 2500 HV [12].  $B_4C$  is an extremely hard boron-carbon ceramic used for ballistic armour, tank armour, bulletproof vests etc. The friction and wear behaviour of micro-textured cemented carbide was investigated against titanium alloy grade 5 using the dry sliding means. The texture filled with lubricant was reported to effectively improve the friction and wear of the cemented carbide disk against the titanium alloy balls [13]. The effect of carbon and boron was studied in Ti-48Al alloys. The crystal structure of  $B_4C$  formed was found to lessen the accumulations of boron atoms. In one study, Ti-48Al-0.2 $B_4C$  was reported to have excellent mechanical properties amongst other alloys. In addition, the microstructure with uniformly distributed borides and carbides was reported to be a good fracture toughness enhancer for the Ti-48Al-0.2 $B_4C$  alloys [14]. A broad approach to refurbish titanium turbine blades by direct laser deposition was investigated. The coatings involved the use of titanium carbide with boron carbide and tungsten carbide particles for an air foil shroud platform. 5 wt % of boron carbide and 5 wt % of tungsten carbide were added to TiC powder. Titanium boride obtained in the coating contains uniformly distributed large solid heat-resistant boron carbide and tungsten carbide particles. The hardness of 520 HV<sub>0.1</sub> was achieved in the coating matrix [15].

Series of works have been carried out with different ceramics especially boron carbide [15] to [18], but there some paucities in the laser cladding of Ti-6Al-4V with  $B_4C$  composite remain. Nevertheless, this paper presents the influence of laser power on improving the laser-deposited Ti-6Al-4V +  $B_4C$  composites through the microstructure and the wear properties for nuclear applications. The cladding requires a weight percentage ratio of 4:1 of Ti-6Al-4V alloy and  $B_4C$ . Here laser powers have been varied between 0.8 kW and 2.2 kW while the scanning speed of 1 m/min, powder flow rate of 3.2 rpm for Ti-6Al-4V alloy, 0.8 rpm for  $B_4C$  and gas flow rate of 2.0 are kept constant.

## 1 EXPERIMENTAL TECHNIQUE

The primary technique used in this experiment is grouped under laser cladding. The experiment was conducted at the National Laser Centre, Council for Scientific and Industrial Research (NLC-CSIR) on a 3.0 kW Ytterbium Laser System. Both the laser system and a Kuka robot are interconnected for the operation. The substrate used is a grit-blasted, 99.6 % Ti-6Al-4V

alloy plate with dimensions of (72 × 72 × 5) mm<sup>3</sup>. The experimental matrixes used are highlighted in Table 1, and the samples are labelled from A to E.

**Table 1.** Experimental matrix

Sample name	A	B	C	D	E
Laser power [kW]	0.8	1.6	1.8	2.0	2.2
Scanning speed [m/min] = 1, Gas flow rate [l/min] = 2					
Powder flow rate [rpm]: Ti-6Al-4V = 3.2; $B_4C$ = 0.8					

The particle size of the Ti-6Al-4V alloy powder used for the deposition ranges between 150 μm to 200 μm while the particle size of the  $B_4C$  powder is about 45 μm to 90 μm. Ten tracks with 50 % overlap were made on the substrate. During the deposition process, the clad is shielded with argon gas in order to prevent environmental oxidation. In this research work, 20 wt % of  $B_4C$  powder was deposited with Ti-6Al-4V alloy powder via the laser deposition process and deposited in a single- layer-multiple-track approach to characterize the wear properties.

### 1.1 Microstructure

According to E3-11 ASTM standard [19], all the samples are sectioned laterally, mounted, ground and polished. The Kroll's reagent was prepared for the etchant with H<sub>2</sub>O, HF, and HNO<sub>3</sub> in the ratio 48:1:3 following the guidelines in the Struers application note for metallurgical preparation of titanium [20]. Each sample was etched for 30 seconds before optical microscopic and SEM observations using BX51M Olympus microscope and TESCAN machine. The SEM uses a VEGA TC software and is equipped with an X-MAX instrument.

### 1.2 Wear

A CETR, UTM-2 tribometer, operating with linear reciprocating motion drive located at the Metallurgy and Chemical Laboratory of the Tshwane University of Technology in Pretoria West Campus, South Africa was used to test for wear. Rotary wear was conducted on the deposited surface of the entire sample for 1000 s using a constant force of 25 N and speed of 60 rpm. Prior to commencing the test, the samples were mounted tightly onto a metal plate which was placed in a reciprocating base and adjusted accordingly to ensure that the tungsten carbide ball is well located on the deposited surface. The tribometer measured the wear depth (WD) as well as the coefficient of friction (COF).

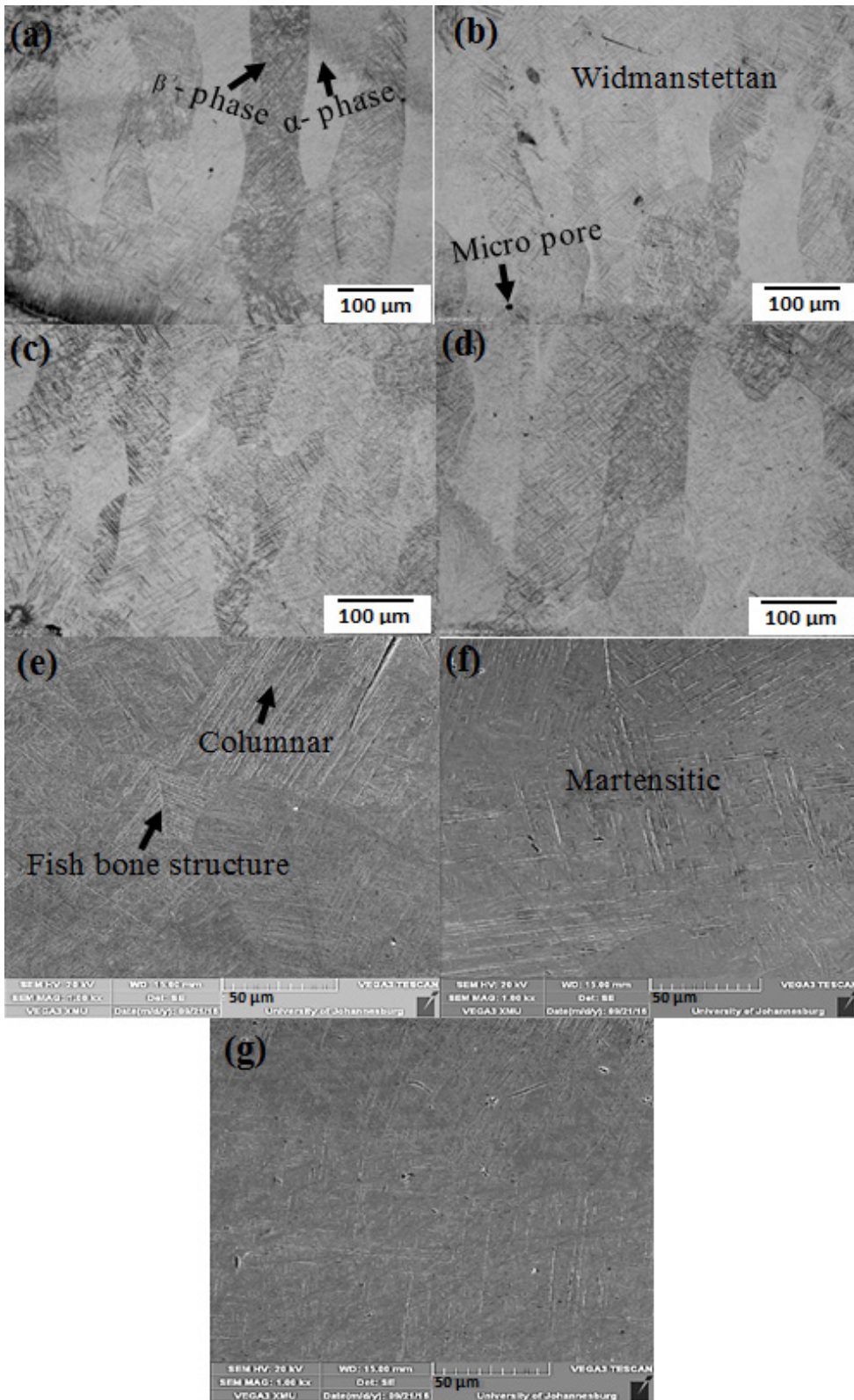


**Fig. 1.** Microstructures of laser deposited Ti-6Al-4V+B4C composite: a) sample A: 0.8 kW; b) sample B: 1.6 kW; c) sample C: 1.8 kW; d) sample D: 2 kW; e) SEM of sample B: 1.6 kW with columnar grains; f) SEM of sample D: 2 kW with martensitic phases; and g) SEM of sample E: 2.2 kW

Using Eqs. (1) to (4), derived by Klenam and Chown [21], the wear loss was calculated as follows:

$$R_2 = \sqrt{\frac{A_2}{\pi}}, \quad (1)$$

$$R_1 = R_2 - t, \quad (2)$$

$$V_s = \pi \times (R_2^2 - R_1^2) \times d_{\max}, \quad (3)$$

$$s = 2\pi \times R_{mean} = \pi \times (2R_2 - t), \quad (4)$$

where  $V_s$  is wear volume [mm<sup>3</sup>],  $R_2$  outer radius [mm],  $R_1$  inner radius [mm],  $t$  mean track thickness [mm].  $d_{\max}$  maximum wear depth [mm], and  $s$  sliding distance [mm].

## 2 RESULTS AND DISCUSSION

The microstructural behaviour and the rotary wear properties of the laser-deposited Ti-6Al-4V+B<sub>4</sub>C composites are presented in detail in this section.

### 2.1 Microstructural Examination

The deposits, the fusion zones, and the heat-affected zones (HAZ) of the laser-deposited samples are taken into consideration for the microstructures. Figs. 1a to d show the microstructures of samples A, B, C, and D deposited at the laser powers of 0.8 kW, 1.6 kW, 1.8 kW, and 2.0 kW, respectively.

The microstructures of the laser deposited composites show the formation of  $\alpha$ -Ti phase and  $\beta$ -Ti phase, and these were elongated towards the fusion zone and terminated at the zone. Globular microstructures were established just immediately after the fusion zone and grow epitaxially within this region and later disappear towards the HAZ(s). The robustness of the  $\alpha/\beta$  phases increases as the

laser power was increased. At high laser power, the coarseness of the microstructure is more obvious than the composite deposited with the previous laser powers due to the energy density of the laser beam. The intensity of the laser beam at high laser power creates more heat input as well as a wider melt pool to accommodate the volume of metal deposit. Widmanstettan structures are also observed in all the microstructures and look harsh and rigid with the agglomeration of 20 wt % of B<sub>4</sub>C added. The microstructures of the Ti-6Al-4V alloy after boriding show more lamellar, which typically enhance the formation of ( $\alpha + \beta$ )-Ti alloys [16]. The thickness of the  $\alpha$ -Ti lamella formed is a significant feature since it influences the mechanical properties of the Ti-6Al-4V alloy [17]. Under the SEM, a fish bone-like of  $\alpha$ -Ti martensitic phase was observed in sample B deposited with a laser power of 1.6 kW and scanning speed of 1 m/min; and this can be attributed to the stability accrued by B<sub>4</sub>C within the deposited region. Columnar grains growing perpendicularly to the heat sink direction were also observed in the deposit. There is an equiaxed transition of these grains, and these were as a result of the steep temperature gradient and the cooling rate effect during the solidification process.

### 2.2 Wear Properties

The wear scars of the substrate and the laser-deposited Ti-6Al-4V+B<sub>4</sub>C composite are shown in Fig. 2. A form of ring-type wear was inscribed on the surface of the samples.

The ring has an inner and outer radius which are measured from the centre and labelled as  $R_1$  and  $R_2$  respectively. The surface topographies of the wear scars of the laser-deposited Ti-6Al-4V+B<sub>4</sub>C

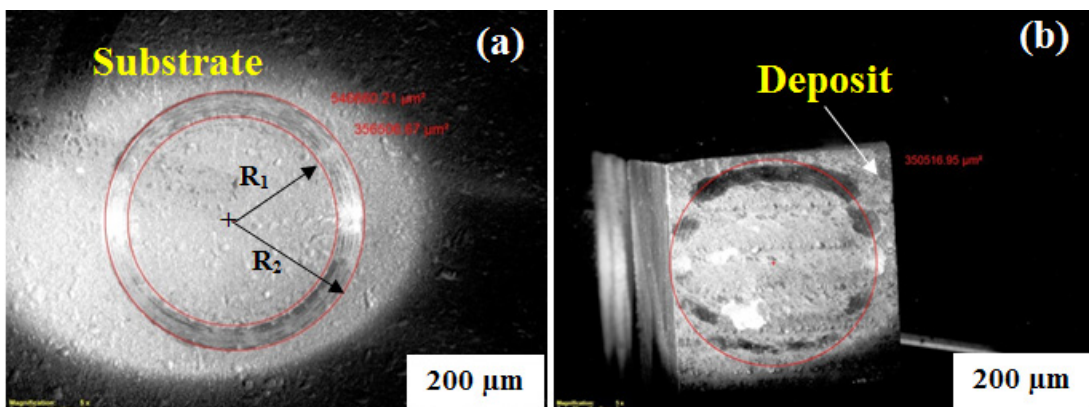
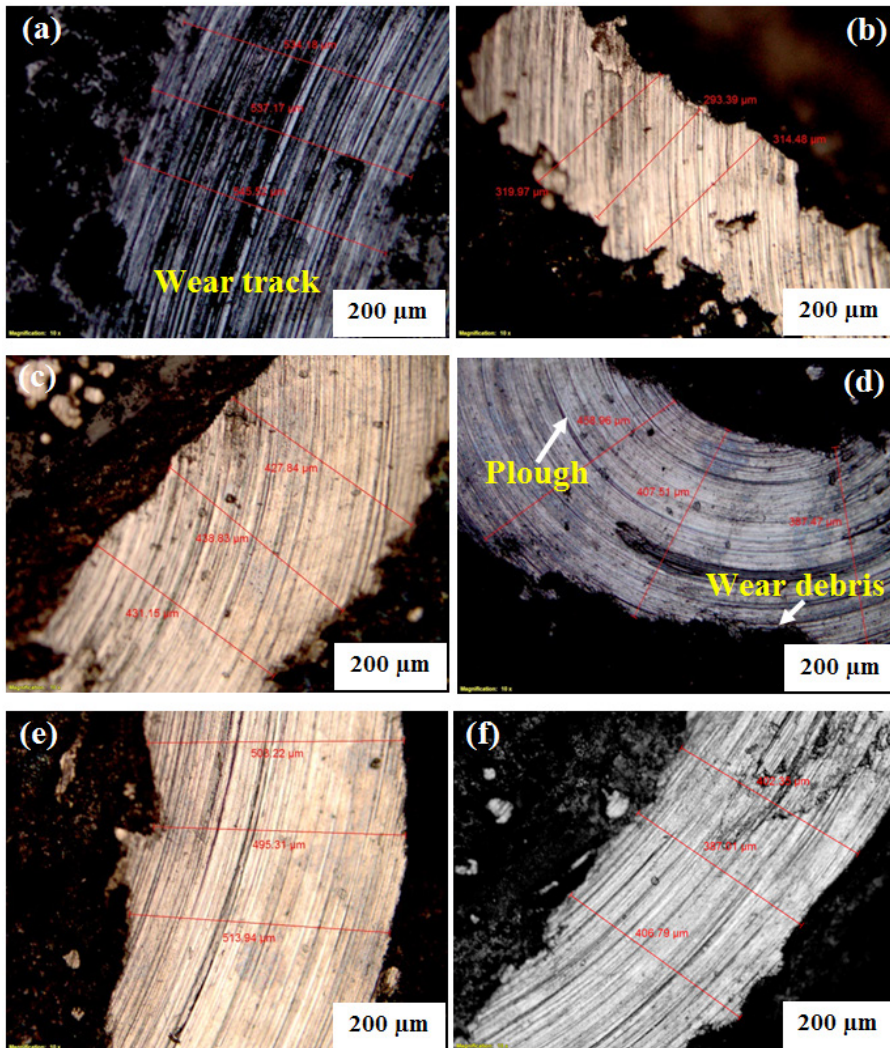


Fig. 2. Wear track of the substrate and the Ti-6Al-4V+B<sub>4</sub>C deposit at 2.0 kW



**Fig. 3.** Wear track of the laser deposited samples showing the thicknesses: a) substrate, b) sample A deposited at laser power of 0.8 kW; c) sample B deposited at laser power of 1.6 kW; d) sample C deposited at laser power of 1.8 kW; e) sample D deposited at laser power of 2 kW; f) sample E deposited at laser power of 2.2 kW

composites after the dry rotary wear tests are shown in Fig. 3.

The sliding friction that exists between the tip of the tungsten carbide ball and the surface of the laser-deposited composites was instigated by the action force. The wear morphology was inscribed as a result of the mechanical action which created a ring-shaped indentation on the surface of the composites. The thicknesses of the wear scars were measured and the average is taken into consideration. This is an essential parameter for the wear volume and wear rate in order to predict the life expectancy of the composite when subjected to wear. Rubbing exists between the tungsten carbide ball and the surface of the laser-deposited composites in a circular manner; and due

to the vertically applied force, wear was initiated on the surfaces as a result of the friction. Thin grooves were generated on the scar in the rubbing direction. The substrate shows a wider thickness as compared to other wear topographies.

Fig. 4 depicts the mean wear thicknesses of the substrate and the laser-deposited Ti-6Al-4V+B<sub>4</sub>C composites from samples A to E.

Fig. 5 shows the profiling of the wear depth of the substrate and the laser-deposited Ti-6Al-4V+B<sub>4</sub>C composites.

At different points, three thicknesses of the wear scar per sample were measured with the optical microscope, and the mean was established. The mean wear thicknesses of the laser-deposited samples varied

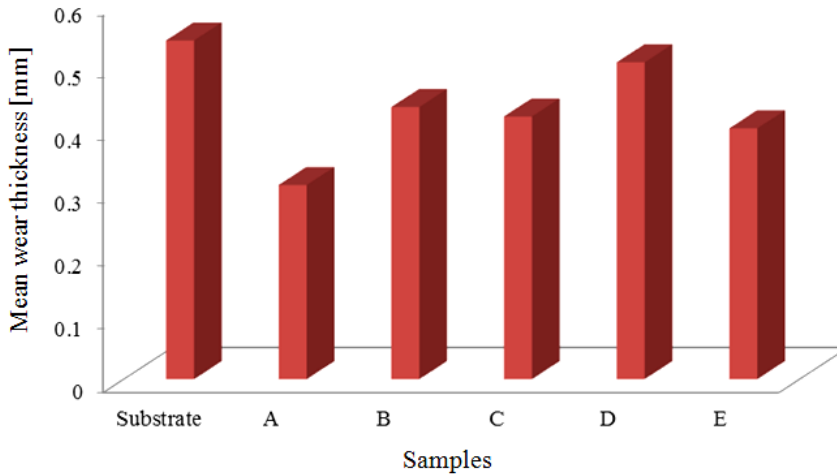


Fig. 4. Plot of mean wear thickness

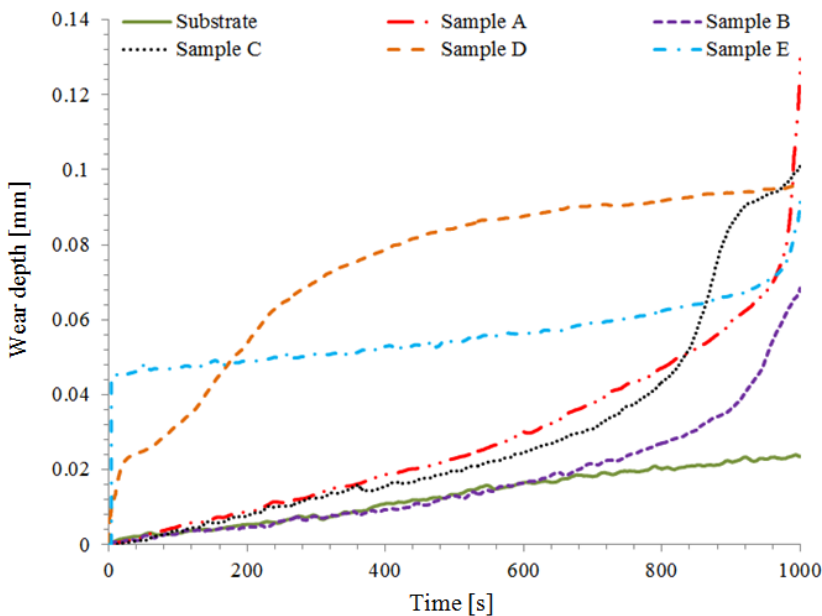


Fig. 5. Profiling of wear depth versus time

from 0.309 mm and 0.504 mm. Sample A deposited at a laser power of 0.8 kW and scanning speed of 1 m/min depicts the lowest wear thickness of 0.309 mm whilst the substrate exhibits the highest mean wear thickness of 0.539 mm. This sample depicts the lowest wear thickness among all other deposited samples; which could be as a result of partly and inhomogeneous melting of B<sub>4</sub>C in the alloy with the low laser power used. From the scattered plot of the wear depth against the time, it can be deduced that there is a linear rise in the trend from the start time to the end time at 1000 seconds. The substrate shows the lowest average wear depth of 0.013 mm, while among

other composites, sample D deposited at a laser power of 1.8 kW and scanning speed of 1 m/min exhibits the highest average wear depth of 0.074 mm. The rolled nature and the compactness of the substrate have a greater effect on its wear depth. Sample E deposited at a laser power of 2.2 kW exhibits a constant wear depth at zero (0) time till 0.045 mm and later maintains a slow steady rise till the end.

Table 2 illustrates the wear loss ( $V_s$ ) of the substrate as well as all the participating laser-deposited samples from samples A to E, respectively.

The wear loss was initiated as a result of the frictional force and the abrasive wear between the

**Table 2.** Wear loss ( $V_s$ ) of the substrate and the laser-deposited specimen

Sample name	Substrate	Sample A	Sample B	Sample C	Sample D	Sample E
Wear loss, $V_s$ [mm <sup>3</sup> ]	0.712	0.329	0.179	0.119	0.515	0.399

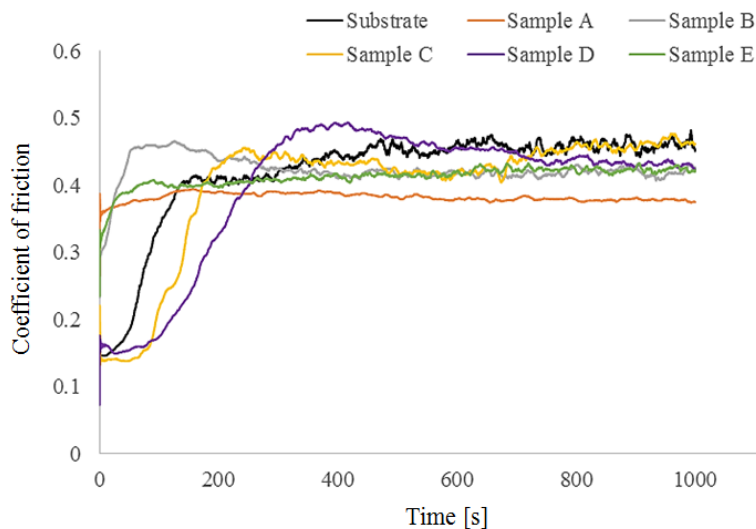
tungsten ball and the top surface of the laser-deposited composite. The round thicker ridge created at the engraved path-way shows the degree of the wear loss. The  $V_s$  measured between the laser-deposited samples A to E is from 0.119 mm<sup>3</sup> to 0.399 mm<sup>3</sup>. Among the deposited Ti-6Al-4V+B<sub>4</sub>C specimens, sample C deposited with a laser power of 1.8 kW exhibits the lowest  $V_s$  of 0.119 mm<sup>3</sup> while the as received substrate has the  $V_s$  of 0.712 mm<sup>3</sup> which is higher than all the deposited samples. The  $V_s$  has been improved with the addition of B<sub>4</sub>C based on the results obtained as shown in Table 2. The radii of the wear tracks and the mean wear depth have a significant effect on the wear loss. The variations between the melting points of the two participating powders as well as their densities have also contributed to the improvement in wear properties. From the values obtained, it can be deduced that, as the laser power was increased from 0.8 kW to 1.8 kW, the wear loss was found to decrease, and later showed a sudden increase from 0.119 mm<sup>3</sup> in sample C to 0.515 mm<sup>3</sup> in sample D at a laser power of 2 kW. For sample E, the  $V_s$  was dropped to 0.399 mm<sup>3</sup>. This behaviour can be attributed to the melting that took place at high laser power as well as the slow cooling rate.

The COF of the as-received substrate as well as the laser-deposited Ti-6Al-4V+B<sub>4</sub>C composites were also analysed and presented in Fig 6.

The COF of all the participating samples is varied between 0.382 and 0.424. Sample A deposited at a laser power of 0.8 kW and scanning speed of 1 m/min exhibits the lowest COF of 0.382 while sample B deposited at a laser power of 1.6 kW shows the highest COF of 0.424, although the value is close to that of the substrate with a COF of 0.419. However, these do not serve as the yardstick for enhancing their wear loss. The COF of all the samples reaches a maximum before they oscillate between limits and maintain steadiness in the range of 0.25 and 0.5. All the samples experience a rise in the COF from the starting point at zero seconds and maintain steadiness in the COF between 0.35 and approximately 0.5.

### 3 CONCLUSION

The coagulation of titanium alloy with boron carbide through the laser deposition process was successfully achieved, and the properties were considerably enhanced. The characteristics conducted on the microstructure of the titanium alloy matrix Ti-6Al-4V+B<sub>4</sub>C composite revealed some globular structures growing epitaxially towards the heat-affected zone. It

**Fig. 6.** COF of the substrate and the laser-deposited Ti-6Al-4V+B<sub>4</sub>C composites

was also evident that the robustness of the  $\alpha/\beta$  phases is as a result of the increase in the laser power. The rubbing that exists between the hard tungsten carbide ball and the surface of the laser-deposited composites facilitated a circular wear scar with different thicknesses and wear depths. Sample A deposited at a laser power of 0.8 kW and scanning speed of 1 m/min depicted the lowest wear thickness and COF of 0.309 mm and 0.382 but does not assure a reduced wear loss due to the wear depth and surface defect. The wear loss has been improved with the addition of 20 wt % of  $B_4C$ . The metal matrix Ti-6Al-4V+ $B_4C$  composites can be applied in the aerospace industries for the repair of parts due to the improved properties.

#### 4 REFERENCES

- [1] Erinosh, M.F., Akinlabi, E.T., Pityana, S. (2015). Influence of processing parameters on laser metal deposited copper and titanium alloy composites. *Transactions of Nonferrous Metals Society of China*, vol. 25, no. 8, p. 2608-2616, DOI:10.1016/S1003-6326(15)63882-1.
- [2] Mahamood, R.M., Akinlabi, E.T. (2015). Effect of laser power and powder flow rate on the wear resistance behaviour of laser metal deposited TiC / Ti6Al4V composites. *Materials Today: Proceedings*, vol. 2, no. 4-5, p. 2679-2686, DOI:10.1016/j.matpr.2015.07.233.
- [3] Tiang, L., Ruan, J., Sparks, T.E., Landers, R.G., Liou F. (2009). Layer-to-layer height control of Laser Metal Deposition processes. *American Control Conference*, p. 5582-5587, DOI:10.1109/ACC.2009.5160407.
- [4] Farayibi, P.K. (2014). *Laser Cladding of Ti-6Al-4V with Carbide and Boride Reinforcements using Wire and Powder Feedstock*, PhD thesis University of Nottingham, Nottingham.
- [5] Balaji, V.S., Kumaran, S. (2014). Densification and microstructural studies of titanium-boron carbide (B4C) powder mixture during spark plasma sintering. *Powder Technology*, vol. 264, p. 536-540, DOI:10.1016/j.powtec.2014.05.050.
- [6] Roy, S., Sarkar, A., Suwas, S. (2010). On characterization of deformation microstructure in Boron modified Ti - 6Al - 4V alloy. *Materials Science and Engineering: A*, vol. 528, no. 1, p. 449-458, DOI:10.1016/j.msea.2010.09.026.
- [7] Sen, I., Tamirisakandala, S., Miracle, D.B., Ramamurty, U. (2007). Microstructural effects on the mechanical behavior of B-modified Ti-6Al-4V alloys. *Acta Materialia*, vol. 55, no. 15, p. 4983-4993, DOI:10.1016/j.actamat.2007.05.009.
- [8] Skorokhod, V.I., Krstic, V.D. (2000). Processing, microstructure, and mechanical properties of B4C-TiB2 particulate sintered composites I. Pressureless sintering and microstructure evolution. *Powder Metallurgy and Metal Ceramics*, vol. 39, no. 7-8, p. 414-423, DOI:10.1023/A:1026625909365.
- [9] Gutmanas, E.Y., Gotman, I. (2000). Reactive synthesis of ceramic matrix composites under pressure. *Ceramics International*, vol. 26, no. 7, p. 699-703, DOI:10.1016/S0272-8842(00)00007-9.
- [10] Itoh, H., Tsunekawa, Y., Tago, S., Iwahara, H. (1993). Synthesis and sinterability of composite powder of the TiB2-B4C system. *Journal of Alloys and Compounds*, vol. 191, no. 2, p. 193-195, DOI:10.1016/0925-8388(93)90063-S.
- [11] Tian, Y.S., Zhang, Q.Y., Wang, D.Y. (2009). Study on the microstructures and properties of the boride layers laser fabricated on Ti-6Al-4V alloy. *Journal of Materials Processing Technology*, vol. 209, no. 6, p. 2887-2891, DOI:10.1016/j.jmatprotec.2008.06.043.
- [12] Levin, L., Frage, N., Dariel, M.P. (2000). A novel approach for the preparation of B4C-based cermets. *International Journal of Refractory Metals and Hard Materials*, vol. 18, no. 2-3, p. 131-135, DOI:10.1016/S0263-4368(00)00012-3.
- [13] Lian, Y., Mu, C., Wang, L., Yao, B., Deng, J., Lei, S. (2018). Numerical simulation and experimental investigation on friction and wear behaviour of micro-textured cemented carbide in dry sliding against TC4 titanium alloy balls, *International Journal of Refractory Metals & Hard Materials*, vol. 73, p. 121-131, DOI:10.1016/j.ijrmhm.2018.02.006.
- [14] Li, M., Xiao, S., Xiao, L., Xu, L., Tian, J., Chen, Y. (2017). Effects of carbon and boron addition on microstructure and mechanical properties of TiAl alloys. *Journal of Alloys and Compounds*, vol. 728, p. 206-221, DOI:10.1016/j.jallcom.2017.08.211.
- [15] Gorunov, A.I. (2018). Complex refurbishment of titanium turbine blades by applying heat-resistant coatings by direct metal deposition. *Engineering Failure Analysis*, vol. 86, p. 115-130, DOI:10.1016/j.engfailanal.2018.01.001.
- [16] Qin, L., Liu, C., Yang, K., Tang, B. (2013). Characteristics and wear performance of borided Ti6Al4V alloy prepared by double glow plasma surface alloying. *Surface and Coatings Technology*, vol. 225, p. 92-96, DOI:10.1016/j.surfcoat.2013.02.053.
- [17] Jackson, M., Jones, N.G., Dye, D., Dashwood, R.J. (2009). Effect of initial microstructure on plastic flow behaviour during isothermal forging of Ti-10V-2Fe-3Al. *Material Science and Engineering: A*, vol. 501, no. 1-2, p. 248-254, DOI:10.1016/j.msea.2008.09.071.
- [18] Makuch, N., Kulka, M., Dziarski, P., Przystacki, D. (2014). Laser surface alloying of commercially pure titanium with boron and carbon. *Optics and Lasers in Engineering*, vol. 57, no. 64-81, DOI:10.1016/j.optlaseng.2014.01.019.
- [19] ASTM E3-11 (2017). *Standard Guide for Preparation of Metallographic Specimens*, ASTM International, West Conshohocken, DOI:10.1520/E0003-11R17.
- [20] Struers Application Note on Titanium (2013). From [http://www.struers.com/resources/elements/12/104827/Application\\_Note\\_Titanium\\_English.pdf](http://www.struers.com/resources/elements/12/104827/Application_Note_Titanium_English.pdf), accessed on 25-08-2013.
- [21] Klenam, D.E.P., Chown, L.H., Papo, M.J., Cornish, L.A. (2015). Characterization of railway stock axle produced from medium-carbon steel. *DST-AMI Nuclear Materials Development Network Conference*, p. 125-137, DOI:10.13140/RG.2.1.1383.1128.



# Vsebina

## Strojniški vestnik - Journal of Mechanical Engineering

letnik 64, (2018), številka 7-8  
Ljubljana, julij-avgust 2018  
ISSN 0039-2480

Izhaja mesečno

### Razširjeni povzetki (extended abstracts)

Wouter Gregoor, Jenny Dankelman, Christoph Kment, Gabriëlle J.M. Tuijthof: Izbira hidravličnega aktuatorja za podajen kirurški sveder za kosti: teoretični pristop	SI 63
Igor Ivanovski, Darko Goričanec, Julijan Jan Salamunič, Tina Žagar: Primerjava dveh visokotemperaturnih toplotnih črpalk za proizvodnjo sanitarne vode	SI 64
Honghu Pan, Xingxi He, Sai Tang, Fanming Meng: Izboljšana metoda za diagnosticiranje napak ležajev z enodimenzionalnimi CNN in LSTM	SI 65
Albin Matavz, József Mursics, Ivan Anzel, Tina Zagar: Vpliv zunanjih pogojev na mehanske lastnosti smolno vezanih brusov s korundnimi in SiC zrnji	SI 66
Jelena Vidaković, Vladimir Kvirgić, Mihailo Lazarević: Zasnova sistema vodenja centrifugalnega simulatorja gibanja na osnovi dinamičnega modela	SI 67
Jun Wan, Jiafeng Yao, Liang'an Zhang, Hongtao Wu: Metoda utežene projekcije gradienta za inverzno kinematiko redundantnih manipulatorjev ob upoštevanju več kriterijev učinkovitosti	SI 68
Mutiu F. Erinosh, Esther T. Akinlabi: Vpliv moči laserja na izboljšanje obrabnih lastnosti lasersko navarjenega kompozita Ti-6Al-4V+B <sub>4</sub> C	SI 69



# Izbira hidravličnega aktuatorja za podajen kirurški sveder za kosti: teoretični pristop

Wouter Gregoor<sup>1</sup> – Jenny Dankelman<sup>1</sup> – Christoph Kment<sup>2</sup> – Gabriëlle J.M. Tuijthof<sup>3,4,\*</sup>

<sup>1</sup> Tehniška univerza v Delftu, Nizozemska

<sup>2</sup> Avstrijsko središče za medicinske inovacije in tehnologijo, Avstrija

<sup>3</sup> Univerza za aplikativne vede Zuyd, Nizozemska

<sup>4</sup> Akademsko medicinsko središče, Nizozemska

Pri minimalno invazivni kirurški mikrofrakturni tehniki se običajno razkrijejo tehnične slabosti ravnih instrumentov in vnaprej določenih smeri vstopa v sklepe: vsa mesta kirurških posegov niso dosegljiva, vrtnanje v sklep pod pravim kotom pa je izvedljivo le ponekod. V članku je raziskana uporabnost alternativnega tehničnega pristopa oz. zasnove podajnega svedra za kosti, ki ga poganja hidravlični aktuator. Cilj je izbira miniaturnega hidravličnega aktuatorja za predlagano aplikacijo. Sveder s hidravličnim pogonom ima več dodatnih prednosti, saj fiziološka raztopina med kirurškim posegom izpira sklep, voda pa tudi hladi sveder in tako preprečuje nekrozo.

Izbira je bila opravljena na osnovi teoretične analize. Konstruktivske zahteve so bile izpeljane iz minimalno invazivnega vrtnanja v kosti: vrtilna frekvenca 750 vrt./min, navor 0,015 Nm in največ 5 mm × 5 mm × 10 mm prostora za vrtnanje luknje premera Ø1,5 mm v človeško kost. Opravljen je bil pregled literature v bazi Scopus in v knjižnici Tehniške univerze v Delftu. Za vsak aktuator sta bila opisana pretok fluida in zahtevana tlačna razlika kot funkciji dimenzij in vrtilne frekvence aktuatorja. Izbira aktuatorja je bila opravljena na osnovi izbrane izhodne moči, navora, realističnih vhodnih dimenzij ter najmanjšega tlaka in števila delov.

V petih knjigah je opisanih šest hidravličnih aktuatorjev: zobniški hidromotor, hidromotor s profilnim rotorjem, aksialna turbina, radialna turbina, Peltonovo kolo in Ossbergerjeva turbina. Zadnji štiri stroji so hidrodinamične turbine, ki ne omogočajo zahtevanih vrtilnih frekvenc. Izbran je bil zobniški hidromotor, in sicer zaradi najmanjše zahtevane tlačne razlike ( $11,5 \times 10^5$  Pa) in preproste konstrukcije.

Prvič: ni bil upoštevan izkoristek aktuatorjev, ki je pomemben zaradi zahteve po majhnih dimenzijah. Podana teoretična primerjava pa je vseeno uporabna. Drugič: avtorji niso spreminjali zasnove šestih hidravličnih aktuatorjev, da bi dosegli rezultate, ki bi se bolje ujemali z zahtevami. Hitra analiza občutljivosti nekaterih parametrov aktuatorjev je pokazala, da ostaja velikostni red izračunanih vrednosti enak. Nejasno je, ali bi bilo te vrednosti mogoče doseči tudi v praksi. Tretjič: izbrana je bila vrtilna hitrost 750 vrt./min, deloma zaradi pomanjkanja podatkov o navoru, ki pa bi jo bilo mogoče zmanjšati zaradi nevarnosti nekroze.

Predstavljen študija je tako prvi pomemben korak v razvoju podajnega svedra za kosti s hidravličnim pogonom. V naslednjem koraku bi bilo mogoče zgraditi in preskusiti miniaturni zobniški hidromotor. Prototip v merilu je potrdil probleme, povezane z izgubami, kritičnimi geometrijami in tolerancami površin. Izgube, ki zmanjšujejo izkoristek, bi bile sicer sprejemljive za medicinsko aplikacijo, toda pričakovana večja tlačna razlika bi lahko ogrozila varnost.

Izpeljane so bile kvantitativne konstruktivske zahteve za podajen minimalno invaziven kirurški sveder za kosti.

- Obravnavanih je bilo šest hidravličnih aktuatorjev: zobniški hidromotor, hidromotor s profilnim rotorjem, aksialna turbina, radialna turbina, Peltonovo kolo in Ossbergerjeva turbina.
- Teoretični izračuni na osnovi kvantitativnih zahtev so pokazali, da je zobniški hidromotor najprimernejša izbira za aktuator.
- Teoretične enačbe so splošne narave in jih bo mogoče uporabiti tudi za izbrane hidravlične aktuatorje v drugih aplikacijah.

**Ključne besede:** ortopedski posegi, kirurška orodja, aktuator, sveder za kosti, hidravlika

# Primerjava dveh visokotemperaturnih toplotnih črpalk za proizvodnjo sanitarne vode

Igor Ivanovski<sup>1</sup> – Darko Goričanec<sup>2</sup> – Julijan Jan Salamunič<sup>3</sup> – Tina Žagar<sup>4,\*</sup>

<sup>1</sup> IVD Maribor, Slovenija

<sup>2</sup> Univerza v Mariboru, Fakulteta za kemijo in kemijsko tehnologijo, Slovenija

<sup>3</sup> Inter oil d.o.o., Slovenija

<sup>4</sup> Ministrstvo za gospodarski razvoj in tehnologijo, Slovenija

Evropska unija se je zavezala k zmanjšanju emisij toplogrednih plinov za vsaj 80 % do leta 2050. Toplotne črpalke bi lahko imele pomembno vlogo za doseganje tega cilja. Na tržišču obstajajo že dalj časa znane toplotne črpalke za nizkotemperaturno ogrevanje (talno ogrevanje, nizkotemperaturni radiatorji, konvektorji...), v zadnjem času pa so se pojavile visokotemperaturne toplotne črpalke za daljinsko ogrevanje in pripravo večjih količin sanitarne vode (npr. v mesni in mlečni industriji), ki izkoriščajo nizkotemperaturne vire kot so: geotermalna voda, odpadna toplota hladilnih sistemov, industrijska odpadna toplota, odpadna toplota dimnih plinov, itd.

Članek primerja energetske učinkovitosti visokotemperaturne toplotne črpalke s hladilom amonijak in transkritično toplotno črpalko s hladilom ogljikov dioksid v smislu grelnega števila COP pri segrevanju sanitarne vode na 65 °C do 85 °C.

Ogljikov dioksid ima v primerjavi s klasičnimi hladili, ki se trenutno uporabljajo v nizkotemperaturnih toplotnih črpalkah, relativno majhen vpliv na globalno segrevanje in ničelni vpliv na razgradnjo ozona, amonijak pa nima vpliva na globalno segrevanje in razgradnjo ozona. Slabost uporabe amonijaka je v njegovi toksičnosti in eksplozivnosti. Po drugi strani ima amonijak izredno visoko latentno toploto, kar omogoča, da se z manjšim pretokom hladila v visokotemperaturni toplotni črpalki doseže visok energetski izkoristek. Slabost uporabe ogljikovega dioksida je v višjih obratovalnih tlakih v uparjalniku in kondenzatorju, kar pomeni da je izvedba dražja. Po drugi strani pa ima ogljikov dioksid dobre fizikalne lastnosti, kar omogoča visoko učinkovitost komprimiranja, in s tem visoko grelni število COP. Prav tako ni toksičen ali vnetljiv in je toplotno obstojen.

Visokotemperaturne toplotne črpalke so že bile predmet različnih raziskav, vendar pa v literaturi nismo zasledili primerjave obeh tehnologij za proizvodnjo sanitarne vode. Poleg tega ni bilo možno zaslediti modela v programu AspenPlus za simulacijo transkritične toplotne črpalke.

Raziskovalno delo je bilo teoretične narave, oblikovali smo modele obeh visokotemperaturnih toplotnih črpalk s prenosniki toplote dimenzioniranimi posebej za ogrevanje sanitarne vode. Prav tako smo zasnovali model za dvostopenjsko visokotemperaturno toplotno črpalko s hladilom amonijak.

Simulacije obratovanja obeh visokotemperaturnih toplotnih črpalk so bile izvedene v programskem paketu AspenPlus na podlagi termodinamične metode REFPROP. Glavna razlika obeh analiziranih procesov je v tem, da pri transkritični toplotni črpalki za kompresorjem ni klasičnega kondenzatorja, ogljikov dioksid se samo ohlaja pri nadkritičnem tlaku, pri visokotemperaturni toplotni črpalki pa amonijak kondenzira in se na ta način proizvede večina toplote v kondenzatorju. V primerih z veliko razliko med temperaturo kondenzacije in uparjanja je tlačno razmerje kompresorja pri uporabi amonijaka previsoko, zato je bila zasnovana dvostopenjska visokotemperaturna toplotna črpalka z vmesnim hladilnikom, ki se je uporabil za predgrevanje sanitarne vode.

Na osnovi rezultatov računalniških simulacij je razvidno, da visokotemperaturna toplotna črpalka, ki uporablja hladilo amonijak, dosega višje grelni število COP, kot transkritična toplotna črpalka, ki uporablja hladilo ogljikov dioksid. V primeru segrevanja sanitarne vode na temperaturo 75 °C in pri uparjanju hladila pri 20 °C je grelni število COP za visokotemperaturno toplotno črpalko znašalo 5,18, medtem ko je za iste pogoje grelni število za transkritično toplotno črpalko znašalo 4,40. Razlike med grelnimi števili so bile najvišje v primeru višje temperature uparjanja hladila in nižje temperature segrevanja sanitarne vode.

**Ključne besede: toplotna-črpalka, sanitarna voda, COP, REFPROP, amonijak, ogljikov dioksid**

# Izboljšana metoda za diagnosticiranje napak ležajev z enodimenzionalnimi CNN in LSTM

Honghu Pan – Xingxi He\* – Sai Tang – Fanming Meng

Univerza v Chongqingu, Državni laboratorij za mehanske prenose, Chongqing, Kitajska

Ležaji predstavljajo najpomembnejši sestavni del rotacijskih strojev. Njihova glavna funkcija je nošenje vrtečih se teles in zmanjševanje količnika trenja med gibanjem. Stalno abrazivno delovanje zaradi medsebojnega gibanja stičnih površin povzroča poškodbe komponent in v več študijah je bilo dokazano, da so napake v ležajih glavni vir odpovedi rotacijskih strojev. Z učinkovitimi metodami za diagnosticiranje napak je mogoče potrditi brezhibno stanje ležajev in preiskovati vzorce napak.

Glavne napake pri ležajih so napake na kroglicah, notranjih ležajih in zunanjih ležajih. Teoretična osnova metod za diagnosticiranje napak je notranja struktura signalov, zbranih pri različnih stanjih ležajev. Tradicionalne metode za diagnosticiranje napak ležajev s signali vibracij imajo običajno tri korake: vnaprejšnja obdelava podatkov, izločitev značilnosti in razvrščanje vzorcev. Izbiranje ustreznih značilnosti je težavna naloga, saj so odvisne od različnih pogojev. V članku je za reševanje tega problema predlagana metoda na osnovi globokega učenja.

Predlagana metoda uporablja dva običajna algoritma (CNN in LSTM), njena izvirnost pa je v združitvi obeh algoritmov. Metoda CNN je zelo uporabna na področju razvrščanja slik, saj zmanjšuje frekvenčno variabilnost, metoda LSTM pa se zelo dobro izkaže pri obdelavi časovnih vrst. V članku je podan predlog izboljšane metode za diagnosticiranje napak z združitvijo enodimenzionalnih CNN in LSTM v eno samo strukturo. S takšnim pristopom se je mogoče izogniti omejitvam tradicionalnega izločanja značilnosti, saj so na vhodu uporabljeni surovi podatki signala in izločanje značilnosti tako sploh ni potrebno.

Predlagani model ima več prednosti v primerjavi z drugimi modeli na osnovi globokega učenja: dosega največjo točnost napovedi s testnim naborom podatkov; iterira hitreje kot model LSTM; in učinkoviteje preprečuje preveliko prilagojenost podatkom kot model DNN. Predlagana metoda ima naslednji prednosti v primerjavi s tradicionalnimi metodami za diagnosticiranje napak: tradicionalno izločanje značilnosti ni potrebno, zato odpadejo motnje zaradi neprimernih značilnosti; točnost napovedi pri predlagani metodi je bistveno večja kot pri tradicionalnih metodah.

Predlagani model ima svoje omejitve, največja slabost pa je računska zahtevnost. S trendom povečevanja računalniških zmogljivosti postaja predlagana metoda vse primernejša tudi za zahtevne mehanske sisteme.

V članku je podan predlog izboljšane metode za diagnosticiranje napak ležajev, ki združuje enodimenzionalne CNN in LSTM. Ob upoštevanju prednosti CNN pri zmanjševanju frekvenčne variabilnosti ter prednosti LSTM pri časovnem modelu je bil izhod CNN uporabljen kot vhod za LSTM. Surovi podatki, zbrani za zaznavanje, so bili razdeljeni v nabor podatkov za učenje in v nabor podatkov za testiranje. Z naborom podatkov za testiranje so bili določeni notranji parametri modela. Nabor podatkov za testiranje je bil nato uporabljen za preverjanje učinkovitosti naučenega modela. Rezultati so pokazali, da povprečna točnost na testnem naboru podatkov presega 99 %, model v najboljši konfiguraciji pa omogoča popolnoma točne napovedi.

**Ključne besede:** diagnosticiranje napak ležajev, globoko učenje, CNN, LSTM, izločanje značilnosti, razvrščanje vzorcev

# Vpliv zunanjih pogojev na mehanske lastnosti smolno vezanih brusov s korundnimi in SiC zrni

Albin Matavz<sup>1</sup> – József Mursics<sup>2</sup> – Ivan Anzel<sup>3,\*</sup> – Tina Zagar<sup>4</sup>

<sup>1</sup>MAMUT TIM, Ltd., Slovenija

<sup>2</sup>FALCO Zrt. Madžarska

<sup>3</sup>Univerza v Mariboru, Fakulteta za strojništvo, Slovenija

<sup>4</sup>Ministrstvo za gospodarski razvoj in tehnologijo, Slovenija

Članek predstavlja rezultate obsežne raziskave učinka zunanjih (atmosferskih) pogojev na osnovi preizkusov, izvedenih na smolno vezanih brusih s korundnimi zrni in zrni silicijevega karbida (SiC). Raziskovali smo, kako v določenih časovnih intervalih staranje vpliva na njihove mehanske in funkcionalne lastnosti. Na osnovi meritev smo oblikovali časovni model poteka sprememb. Prav tako smo preverili in ugotavljali vpliv vlažnosti zraka kot najverjetnejšega povzročitelja hitrejšega padca mehanskih lastnosti brusov. V tem kontekstu smo uporabili sistem vsiljenega, t.j. hitrejšega staranja brusov (dodatno vlaženje) pri atmosferskih pogojih. V nadaljevanju smo na osnovi karakterizacije mikrostruktur brusov, ki so bili izpostavljeni različnim termo mehanskim vplivom izdelali različne modele mehanizmov spreminjanja mikrostruktur med staranjem, ki so potrdili že empirično ugotovljen najverjetnejši razlog vpliva na staranje in s tem povezanih sprememb mehanskih lastnosti brusov. Ugotovitve smo z reverzibilnim procesom termične obdelave brusov tudi potrdili. Meritve mehanskih lastnosti brusov so bile podlaga za oblikovanje časovnega modela sprememb mehanskih lastnosti smolno vezanih brusov.

V cilju tega so bile izvedene spodnje znanstvene raziskave in izpeljane naslednje ugotovitve:

- narejena je bila natančna raziskava vseh možnih strokovnih in literaturnih virov s to problematiko,
- pripravljen je bil natančen koncept priprave in izdelani testni vzorci smolno vezanih brusov v realnih industrijskih pogojih (vzorci narejeni v serijski proizvodnji pri slovenskem proizvajalcu),
- raziskano je bilo, kaj povzroča padec reznih sposobnosti brusa (hidroskopična vlaga iz zraka, pore in potujoče razpoke po polimerni matrici do posameznih zrn v brusu),
- raziskan je bil sam proces hitrejšega padca mehanskih lastnosti brusov, pri čemer je bilo ugotovljeno, kako poteka staranje zaradi mikroporoznosti, evkladiranih komponent in potovanja mehansko ustvarjenih mikro razpok po polimerni matrici brusa,
- ugotovljeno je bilo, kako vlažnost zraka oz. količina vode v zraku posledično vpliva na velikost padca kakovosti in s tem povezan proces hitrosti staranja brusov,
- na osnovi preizkusov so bili ugotovljeni in eliminirani vplivni faktorji, ki povzročajo staranje smolno zanih brusov in zmanjšujejo njihove rezne lastnosti,
- ugotovljene so bile dejanske vrednosti faktorjev reznosti brusov med časovno definiranim modelom procesa staranja, ugotovljen je bil vpliv staranja na vrtilne hitrosti pri razletu brusov med samim procesom staranja,
- z mikrostrukturno analizo vzorcev so bile potrjene empirične ugotovitve padca mehanskih lastnosti brusov in oblikovan model poteka mehanskih sprememb (potovanje razpok) v polimerni matrici.

Na osnovi rezultatov raziskave je ugotovljeno, da poteka proces staranja bistveno hitreje, kot smo predvidevali. Največji padec mehanskih lastnosti smolno vezanih brusov nastopi v prvih 45 dneh od dneva proizvodnje, kar potrjujejo meritve mehanskih lastnosti kot tudi meritve funkcionalnih lastnosti brusov. Sočasne primerjave rezultatov meritev reznega faktorja brusov in maksimalne vrtilne hitrosti so pokazale, da ima proces staranja negativen vpliv na obe funkcionalni lastnosti v prvi fazi (45 dni), nato pa se trend obrne. Navzkrižna karakterizacija mikrostruktur vzorcev brusov, ki so bili izpostavljeni termo mehanskim vplivom (preizkusi rezanja) je pokazala, na kakšen način poteka proces staranja v brusih in kako velik vpliv ima vlaga ujeta v porah polimerne matrice, kar pa pomeni, da imajo na potek in hitrost staranja ključen vpliv velikost, razporejenost ter količina por ujetih v polimerni matrici brusa, s tem pa tudi na hitrost in širino potovanja mikrorazpok po matrici brusa do abrazivnih zrn v matrici.

Zmanjšanje in obvladovanje nastanka por ter posledično manjši padec mehanskih lastnosti brusov skozi časovno obdobje je povezano s tem, kako in na kakšen način proizvajalci brusov obvladujejo celoten proizvodni proces in kako kvalitetno obvladujejo atmosferske pogoje pri skladiščenju brusov.

**Ključne besede: smolno vezani brusi, mehanske lastnosti, staranje, mikroskopska analiza**

# Zasnova sistema vodenja centrifugalnega simulatorja gibanja na osnovi dinamičnega modela

Jelena Vidaković<sup>1,\*</sup> – Vladimir Kvirgić<sup>2</sup> – Mihailo Lazarević<sup>3</sup>

<sup>1</sup> Univerza v Beogradu, Inštitut Lola, Srbija

<sup>2</sup> Univerza v Beogradu, Inštitut Mihajlo Pupin, Srbija

<sup>3</sup> Univerza v Beogradu, Fakulteta za strojništvo, Srbija

Piloti sodobnih bojnih letal so izpostavljeni nevarnim učinkom velikih pospeškov in silovitih odklonov gibanja v vseh treh oseh letala. Centrifugalni simulator gibanja (CMS) je naprava, ki omogoča simulacijo delovanja vztrajnostnih sil na pilota v nadzorovanih pogojih. V članku je predstavljena zasnova regulacijskega sistema CMS na osnovi dinamičnega modela in pristop k izbiri pogonov za CMS. Cilj predstavljene metodologije je doseganje želene učinkovitosti ob upoštevanju kompleksnosti regulacijskega sistema in stroškov celotne naprave.

CMS je modeliran in reguliran kot robotski manipulator s tremi prostostnimi stopnjami, model inverzne dinamike (ID) pa je postavljen v obliki rekurzivnih Newton-Eulerjevih enačb. Pri izbiri regulacijskega sistema robotskega manipulatorja imata v praksi pomembno vlogo kompleksnost in zahteve v zvezi z implementacijo. Zato se postavlja vprašanje, ali in kako naj bo v vodenju upoštevan dinamični model.

Predstavljena je metoda simulacije na osnovi ID za ocenjevanje dinamične interakcije povezanega gibanja členov robota, ki omogoča tehtanje upravičenosti uporabe decentraliziranega povratnozančnega krmilnika ali centraliziranih metod vodenja.

CMS spadajo v kategorijo težke mehanizacije: trajektorije zgibov predstavljajo izziv, aktuatorji želene moči pa so zelo težki. Za zmanjšanje vztrajnosti manipulatorja, rabe energije in stroškov celotnega sistema je zelo pomembno, da imajo motorji dovolj moči za hitro vrtenje zgibov, obenem pa morajo biti lahki. Pri izbiri pogona je uporabljen postopek na osnovi modela približne inverzne dinamike (aID), ki omogoča določanje najmanjših aktuatorjev za zahtevano gibanje zgibov.

Za točno primerjavo predlaganih metod vodenja z realistično simulacijo so izpolnjeni naslednji pogoji: 1) vztrajnost gredi rotorjev je izračunana iz ID za želene trajektorije zgibov in izbrane modele aktuatorjev, omogoča pa realističen model procesa; 2) izbira ojačenja povratnozančnega krmilnika upošteva lastne frekvence konstrukcije; in 3) upoštevane so omejitve navora za izbrane aktuatorje.

Na podlagi rezultatov predlagane metode simulacije ID je bilo izbrano decentralizirano vodenje roke CMS. Za osi obroča in gondole je bila uporabljena predlagana metoda simulacije sistema vodenja za primerjavo učinkovitosti standardnega povratnozančnega vodenja in centralizirane strategije vodenja, kjer je v povratno zanko dodana metoda izračunanega navora (CT). Simulacije povratne zanke z dodatkom CT so pokazale pomembne koristi pri sledenju položaja z odpravo motenj, ko je izbran ustrezen pogon za želeno gibanje. Predlagani postopek na osnovi aID je bil uporabljen pri izbiri pogonskega sistema. Za razliko od predhodno objavljenih del je podana učinkovitost obravnavanih metod vodenja za bistveno zahtevnejši profil trajektorije CMS z največjim pospeškom 9 g, največjo stopnjo pospeška 9 g/s in prehodnimi obremenitvami.

Predstavljene metode snovanja in simulacije sistemov vodenja in strategije za izbiro pogonov za CMS so uporabne tudi na širšem področju robotskih manipulatorjev. Prihodnje raziskave bodo usmerjene v uvajanje predstavljene metodologije pri realnih sistemih in pri obravnavi drugih centraliziranih metod vodenja.

**Ključne besede:** robotska dinamika, vodenje robotov, metoda izračunanega navora, centrifuga

# Metoda utežene projekcije gradienta za inverzno kinematiko redundantnih manipulatorjev ob upoštevanju več kriterijev učinkovitosti

Jun Wan<sup>1,\*</sup> – Jiafeng Yao<sup>1</sup> – Liang'an Zhang<sup>2</sup> – Hongtao Wu<sup>1</sup>

<sup>1</sup> Kolidž za strojništvo in elektrotehniko, Univerza za aeronavtiko in astronautiko v Nanjingu, Kitajska

<sup>2</sup> Oddelek za strojništvo, Tehniška univerza Anhui, Kitajska

Pri inverzni kinematiki (IK) kinematično redundantnih manipulatorjev je značilno, da je za določen položaj vrha robota na voljo neskončno število različnih položajev sklepov. Zato obstaja potreba po učinkoviti in praktični metodi za reševanje problema IK pri redundantnih manipulatorjih.

Danes se za reševanje IK redundantnih manipulatorjev najpogosteje uporabljata klasična metoda utežene najmanjše norme (WLN) in metoda projekcije gradienta (GPM). Metoda WLN se pogosto uporablja za uspešno izogibanje mejnim položajem sklepov, ni pa je mogoče razširiti tudi na ostale omejitve. Metoda GPM učinkovito razreši probleme IK redundantnih manipulatorjev z več omejitvami, težave pa nastopijo pri izbiri ustreznih koeficientov kriterijev učinkovitosti.

V članku je podan predlog utežene metode projekcije gradienta (WGPM) na osnovi prednosti WLN in GPM, ki omogoča reševanje problemov IK redundantnih manipulatorjev z več kriteriji učinkovitosti. Metoda je strukturirana kot regulacija na nivoju hierarhičnih nalog, ki lahko zagotavlja uspešnost glavne naloge in več podrejenih nalog. Da bi se izognili pomanjkljivosti metode GPM, kjer se skalarni faktorji za različne kriterije izbirajo na način poskusov in napak, je v WGPM uvedena tehnika za določanje ustreznih skalarnih koeficientov z normalizacijo ustreznih funkcij učinkovitosti. Teoretični del članka spada na področje kinematike robotov.

1. Predlagana metoda WGPM v simulacijah uspešno premakne vse sklepe iz mejnih položajev, medtem ko metoda WLN duši gibanje sklepov v mejnih položajih. Obe metodi pa kršita omejitve hitrosti sklepov ob neupoštevanju ustreznega kriterija učinkovitosti.
2. Metoda GPM se v eksperimentih pri izogibanju mejnim položajem sklepov pričakovano izkaže enako dobro kot metoda WGPM. Metoda GPM pa ni uspešna pri izogibanju omejitvam hitrosti sklepov zaradi neprimernih fiksnih uteži pri več kriterijih. Metoda WGPM lahko po drugi strani učinkovito regulira oddaljene meje hitrosti sklepov na osnovi zveznega skalarnega koeficienta.
3. Regulacija na nivoju hierarhičnih nalog in podrejenih nalog pri predlagani metodi WGPM je po analizah in primerjavah z metodama WLN in GPM glavni vplivni dejavnik za izboljšanje kinematike in prihranek časa.

Trenutno je s predlagano metodo WGPM implementirano samo vodenje kinematike ene roke manipulatorja s sedmimi prostostnimi stopnjami. Za validacijo uspešnosti metode WGPM bo delo v prihodnje osredotočeno na vodenje kinematike redundantnega manipulatorja z dvema rokama.

1. Za odpravo omejitev metode WLN sta bila uvedena utežena matrika in odbojno potencialno polje, ki silita sklepe proč od mejnih položajev, ne da bi jih tam blokirala.
2. Za izbiro ustreznih skalarnih faktorjev za različne kriterije učinkovitosti je v članku predstavljena tehnika določanja zveznih skalarnih koeficientov na osnovi normalizacije kriterijev in ne na osnovi empirike.
3. Za regulacijo podrejenih nalog in preprečevanje sporov med njimi je predstavljena hierarhična rešitev, kjer so prioritete kriterijev učinkovitosti organizirane v padajočem vrstnem redu.

Predlagana metoda WGPM je tako učinkovitejša in bolj praktična od metod WLN in GPM.

**Ključne besede:** inverzna kinematika, več kriterijev učinkovitosti, redundantni manipulator, skalarni koeficient, normalizacija, metoda utežene projekcije gradienta

# Vpliv moči laserja na izboljšanje obrabnih lastnosti lasersko navarjenega kompozita Ti-6Al-4V+B<sub>4</sub>C

Mutiu F. Erinosh\* – Esther T. Akinlabi

Univerza v Johannesburgu, Oddelek za strojništvo, Južna Afrika

Titanove zlitine imajo odlične lastnosti, kot sta denimo visoka trdnost in protikorozijska obstojnost, zato so se uveljavile v letalski in vesoljski industriji, medicini, pomorstvu in v kemični industriji.

Namen raziskovalnega projekta je bil preučiti mikrostrukturo in obrabne lastnosti kompozitov s titanovo osnovo Ti-6Al-4V+B<sub>4</sub>C. Kompoziti so bili izdelani po postopku laserskega navarjanja z iterbijevim laserjem moči 3000 W na robotskem sistemu Kuka. Cilj predstavljenega dela je identifikacija lastnosti kompozita kovinske osnove iz titanove zlitine in borovega karbida, izdelanega po tehniki laserskega navarjanja, ter preučitev mikrostrukture in obrabnih lastnosti. Prahova zlitine Ti-6Al-4V in B<sub>4</sub>C sta bila lasersko navarjena v utežnem razmerju 4:1. Moč laserja se je spreminjala med 0,8 in 2,2 kW pri konstantni hitrosti žarka 1 m/min, pretoku prahu 3,2 vrt./min za zlitino Ti-6Al-4V oz. 0,8 vrt./min za B<sub>4</sub>C, in pretoku plina 2,0 l/min. Substrat je bil pred navarjanjem speskan in očiščen z acetonom. Vsi vzorci so bili lateralno izrezani, zbrušeni in spolirani. Za jedkanje je bil uporabljen Krollov reagent, ki vsebuje H<sub>2</sub>O, HF in HNO<sub>3</sub>.

Navarjena površina vzorcev je bila izpostavljena rotacijski obrabi za 1000 sekund s konstantno silo 25 N in hitrostjo 60 vrt./min. S tribometrom sta bila izmerjena globina obrabe in količnik trenja. V mikrostrukturi lasersko navarjenih kompozitov sta bili ugotovljeni fazi  $\alpha$ -Ti in  $\beta$ -Ti, ki sta podaljšani proti talilni coni in se končata pri njej. Debelina lističev  $\alpha$ -Ti je zelo pomembna, saj vpliva na mehanske lastnosti zlitine. Srednja debelina obrabe lasersko navarjenih vzorcev je znašala od 0,309 mm do 0,504 mm. Vzorec A, navarjen pri moči laserja 0,8 kW in hitrosti žarka 1 m/min, je imel najmanjšo debelino obrabe 0,309 mm, največja srednja debelina obrabe 0,539 mm pa je bila ugotovljena pri substratu. Izguba materiala je bila določena na drsni poti. Izmerjene obrabne izgube materiala pri lasersko navarjenih vzorcih A do E so znašale od 0,119 mm<sup>3</sup> do 0,399 mm<sup>3</sup>. Količnik trenja pri vseh obravnavanih vzorcih je znašal od 0,382 do 0,424. Najmanjši količnik trenja 0,382 je bil ugotovljen pri vzorcu A (moč laserja 0,8 kW, hitrost žarka 1 m/min), največji količnik trenja 0,424 pa pri vzorcu B (moč laserja 1,6 kW).

Prispevek in novost tega raziskovalnega dela je v širokem razponu moči laserja, ki so bile uporabljene pri eksperimentih, prav tako pa pred tem še niso bili opravljeni rotacijski preskusi obrabe na površini kompozita. Nastali kolobar ima notranji in zunanji polmer, ki sta bila merjena od središča. Z optičnim mikroskopom so bile izmerjene tri debeline obrabne sledi na vzorec in nato je bila določena srednja vrednost.

Rezultati raziskave potrjujejo izboljšanje lastnosti in bodo tako uporabni pri popravilu letalskih komponent.

**Ključne besede:** lasersko navarjanje, mikrostruktura, meritev obrabe, kompozit Ti-6Al-4V+B<sub>4</sub>C, obrabne izgube

# Information for Authors

All manuscripts must be in English. Pages should be numbered sequentially. The manuscript should be composed in accordance with the Article Template given above. The maximum length of contributions is 10 pages. Longer contributions will only be accepted if authors provide justification in a cover letter. For full instructions see the Information for Authors section on the journal's website: <http://en.sv-jme.eu>.

## SUBMISSION:

Submission to SV-JME is made with the implicit understanding that neither the manuscript nor the essence of its content has been published previously either in whole or in part and that it is not being considered for publication elsewhere. All the listed authors should have agreed on the content and the corresponding (submitting) author is responsible for having ensured that this agreement has been reached. The acceptance of an article is based entirely on its scientific merit, as judged by peer review. Scientific articles comprising simulations only will not be accepted for publication; simulations must be accompanied by experimental results carried out to confirm or deny the accuracy of the simulation. Every manuscript submitted to the SV-JME undergoes a peer-review process.

The authors are kindly invited to submit the paper through our web site: <http://ojs.sv-jme.eu>. The Author is able to track the submission through the editorial process - as well as participate in the copyediting and proofreading of submissions accepted for publication - by logging in, and using the username and password provided.

## SUBMISSION CONTENT:

The typical submission material consists of:

- A **manuscript** (A PDF file, with title, all authors with affiliations, abstract, keywords, highlights, inserted figures and tables and references),
  - Supplementary files:
    - a **manuscript** in a WORD file format
    - a **cover letter** (please see instructions for composing the cover letter)
    - a ZIP file containing **figures** in high resolution in one of the graphical formats (please see instructions for preparing the figure files)
    - possible **appendices** (optional), cover materials, video materials, etc.
- Incomplete or improperly prepared submissions will be rejected with explanatory comments provided. In this case we will kindly ask the authors to carefully read the Information for Authors and to resubmit their manuscripts taking into consideration our comments.

## COVER LETTER INSTRUCTIONS:

Please add a **cover letter** stating the following information about the submitted paper:

1. **Paper title**, list of **authors** and their **affiliations**.
2. **Type of paper**: original scientific paper (1.01), review scientific paper (1.02) or short scientific paper (1.03).
3. A **declaration** that neither the manuscript nor the essence of its content has been published in whole or in part previously and that it is not being considered for publication elsewhere.
4. State the **value of the paper** or its practical, theoretical and scientific implications. What is new in the paper with respect to the state-of-the-art in the published papers? Do not repeat the content of your abstract for this purpose.
5. We kindly ask you to suggest at least two **reviewers** for your paper and give us their names, their full affiliation and contact information, and their scientific research interest. The suggested reviewers should have at least two relevant references (with an impact factor) to the scientific field concerned; they should not be from the same country as the authors and should have no close connection with the authors.

## FORMAT OF THE MANUSCRIPT:

The manuscript should be composed in accordance with the Article Template. The manuscript should be written in the following format:

- A **Title** that adequately describes the content of the manuscript.
- A list of **Authors** and their **affiliations**.
- An **Abstract** that should not exceed 250 words. The Abstract should state the principal objectives and the scope of the investigation, as well as the methodology employed. It should summarize the results and state the principal conclusions.
- 4 to 6 significant **key words** should follow the abstract to aid indexing.
- 4 to 6 **highlights**; a short collection of bullet points that convey the core findings and provide readers with a quick textual overview of the article. These four to six bullet points should describe the essence of the research (e.g. results or conclusions) and highlight what is distinctive about it.
- An **Introduction** that should provide a review of recent literature and sufficient background information to allow the results of the article to be understood and evaluated.
- A **Methods** section detailing the theoretical or experimental methods used.
- An **Experimental section** that should provide details of the experimental set-up and the methods used to obtain the results.
- A **Results** section that should clearly and concisely present the data, using figures and tables where appropriate.
- A **Discussion** section that should describe the relationships and generalizations shown by the results and discuss the significance of the results, making comparisons with previously published work. (It may be appropriate to combine the Results and Discussion sections into a single section to improve clarity.)
- A **Conclusions** section that should present one or more conclusions drawn from the results and subsequent discussion and should not duplicate the Abstract.
- **Acknowledgement** (optional) of collaboration or preparation assistance may be included. Please note the source of funding for the research.
- **Nomenclature** (optional). Papers with many symbols should have a nomenclature that defines all symbols with units, inserted above the references. If one is used, it must contain all the symbols used in the manuscript and the definitions should not be repeated in the text. In all cases, identify the symbols used if they are not widely recognized in the profession. Define acronyms in the text, not in the nomenclature.
- **References** must be cited consecutively in the text using square brackets [1] and collected together in a reference list at the end of the manuscript.
- **Appendix(-ices)** if any.

## SPECIAL NOTES

**Units:** The SI system of units for nomenclature, symbols and abbreviations should be followed closely. Symbols for physical quantities in the text should be written in italics (e.g.  $v$ ,  $T$ ,  $n$ , etc.). Symbols for units that consist of letters should be in plain text (e.g.  $\text{ms}^{-1}$ , K, min, mm, etc.). Please also see: <http://physics.nist.gov/cuu/pdf/sp811.pdf>.

**Abbreviations** should be spelt out in full on first appearance followed by the abbreviation in parentheses, e.g. variable time geometry (VTG). The meaning of symbols and units belonging to symbols should be explained in each case or cited in a **nomenclature** section at the end of the manuscript before the References.

**Figures** (figures, graphs, illustrations digital images, photographs) must be cited in consecutive numerical order in the text and referred to in both the text and the captions as Fig. 1, Fig. 2, etc. Figures should be prepared without borders and on white grounding and should be sent separately in their original formats. If a figure is composed of several parts, please mark each part with a), b), c), etc. and provide an explanation for each part in Figure caption. The caption should be self-explanatory. Letters and numbers should be readable (Arial or Times New Roman, min 6 pt with equal sizes and fonts in all figures). Graphics (submitted as supplementary files) may be exported in resolution good enough for printing (min. 300 dpi) in any common format, e.g. TIFF, BMP or JPG, PDF and should be named Fig1.jpg, Fig2.tif, etc. However, graphs and line drawings should be prepared as vector images, e.g. CDR, AI. Multi-curve graphs should have individual curves marked with a symbol or otherwise provide distinguishing differences using, for example, different thicknesses or dashing.

**Tables** should carry separate titles and must be numbered in consecutive numerical order in the text and referred to in both the text and the captions as Table 1, Table 2, etc. In addition to the physical quantities, such as  $t$  (in italics), the units [s] (normal text) should be added in square brackets. Tables should not duplicate data found elsewhere in the manuscript. Tables should be prepared using a table editor and not inserted as a graphic.

## REFERENCES:

A reference list must be included using the following information as a guide. Only cited text references are to be included. Each reference is to be referred to in the text by a number enclosed in a square bracket (i.e. [3] or [2] to [4] for more references; do not combine more than 3 references, explain each). No reference to the author is necessary.

References must be numbered and ordered according to where they are first mentioned in the paper, not alphabetically. All references must be complete and accurate. Please add DOI code when available. Examples follow.

## Journal Papers:

Surname 1, Initials, Surname 2, Initials (year). Title. Journal, volume, number, pages, DOI code.

- [1] Hackenschmidt, R., Alber-Laukant, B., Rieg, F. (2010). Simulating nonlinear materials under centrifugal forces by using intelligent cross-linked simulations. *Strojniški vestnik - Journal of Mechanical Engineering*, vol. 57, no. 7-8, p. 531-538, DOI:10.5545/sv-jme.2011.013.

Journal titles should not be abbreviated. Note that journal title is set in italics.

## Books:

Surname 1, Initials, Surname 2, Initials (year). Title. Publisher, place of publication.

- [2] Groover, M.P. (2007). *Fundamentals of Modern Manufacturing*. John Wiley & Sons, Hoboken.

Note that the title of the book is italicized.

## Chapters in Books:

Surname 1, Initials, Surname 2, Initials (year). Chapter title. Editor(s) of book, book title. Publisher, place of publication, pages.

- [3] Carbone, G., Ceccarelli, M. (2005). Legged robotic systems. Kordić, V., Lazinica, A., Merdan, M. (Eds.), *Cutting Edge Robotics*. Pro literatur Verlag, Mammendorf, p. 553-576.

## Proceedings Papers:

Surname 1, Initials, Surname 2, Initials (year). Paper title. Proceedings title, pages.

- [4] Štefanič, N., Martinčević-Mikić, S., Tošanović, N. (2009). Applied lean system in process industry. *MOTSP Conference Proceedings*, p. 422-427.

## Standards:

Standard-Code (year). Title. Organisation. Place.

- [5] ISO/DIS 16000-6.2:2002. *Indoor Air - Part 6: Determination of Volatile Organic Compounds in Indoor and Chamber Air by Active Sampling on TENAX TA Sorbent, Thermal Desorption and Gas Chromatography using MSD/FID*. International Organization for Standardization. Geneva.

## WWW pages:

Surname, Initials or Company name. Title, from <http://address>, date of access.

- [6] Rockwell Automation. Arena, from <http://www.arenasimulation.com>, accessed on 2009-09-07.

## EXTENDED ABSTRACT:

When the paper is accepted for publishing, the authors will be requested to send an **extended abstract** (approx. one A4 page or 3500 to 4000 characters). The instruction for composing the extended abstract are published on-line: <http://www.sv-jme.eu/information-for-authors/>.

## COPYRIGHT:

Authors submitting a manuscript do so on the understanding that the work has not been published before, is not being considered for publication elsewhere and has been read and approved by all authors. The submission of the manuscript by the authors means that the authors automatically agree to transfer copyright to SV-JME when the manuscript is accepted for publication. All accepted manuscripts must be accompanied by a Copyright Transfer Agreement, which should be sent to the editor. The work should be original work by the authors and not be published elsewhere in any language without the written consent of the publisher. The proof will be sent to the author showing the final layout of the article. Proof correction must be minimal and executed quickly. Thus it is essential that manuscripts are accurate when submitted. Authors can track the status of their accepted articles on <http://en.sv-jme.eu/>.

## PUBLICATION FEE:

Authors will be asked to pay a publication fee for each article prior to the article appearing in the journal. However, this fee only needs to be paid after the article has been accepted for publishing. The fee is 320 EUR (for articles with maximum of 6 pages), 400 EUR (for articles with maximum of 10 pages), plus 40 EUR for each additional page. The additional cost for a color page is 90.00 EUR. These fees do not include tax.

Strojniški vestnik - Journal of Mechanical Engineering  
Askerčeva 6, 1000 Ljubljana, Slovenia,  
e-mail: [info@sv-jme.eu](mailto:info@sv-jme.eu)



<http://www.sv-jme.eu>

# Contents

## Papers

- 425 Wouter Gregoor, Jenny Dankelman, Christoph Kment, Gabriëlle J.M. Tuijthof:  
**Hydraulic Actuator Selection for a Compliant Surgical Bone Drill:  
A Theoretical Approach**
- 437 Igor Ivanovski, Darko Goričanec, Julijan Jan Salamunić, Tina Žagar:  
**The Comparison between Two High-Temperature Heat-Pumps  
for the Production of Sanitary Water**
- 443 Honghu Pan, Xingxi He, Sai Tang, Fanming Meng:  
**An Improved Bearing Fault Diagnosis Method  
using One-Dimensional CNN and LSTM**
- 453 Albin Matavz, József Mursics, Ivan Anzel, Tina Zagar:  
**The Influence of External Conditions on the Mechanical Properties  
of Resin-bonded Grinding Wheels**
- 465 Jelena Vidaković, Vladimir Kvirgić, Mihailo Lazarević:  
**Control System Design for a Centrifuge Motion Simulator  
Based on a Dynamic Model**
- 475 Jun Wan, Jiafeng Yao, Liang'an Zhang, Hongtao Wu:  
**A Weighted Gradient Projection Method for Inverse Kinematics  
of Redundant Manipulators Considering Multiple Performance Criteria**
- 488 Mutiu F. Erinosho, Esther T. Akinlabi:  
**Influence of Laser Power on Improving the Wear Properties  
of Laser-Deposited Ti-6Al-4V+B4C Composite**